On Uncertainty Quantification of Models Defined by Initial and Boundary Value Problems for Differential Equations

Thesis to obtain the degree of **Doctor of Science**

with Speciality in Applied Mathematics

by

Hugo Alberto Flores Arguedas

date

Guanajuato, Guanajuato, México.

Advisor: Marcos Aurelio Capistrán Ocampo.

Dedication

¿No podría ser que digas: "Con mi propio esfuerzo me conseguí esta buena situación"? Más bien acuérdate de Yavé, tu Dios, que te dio fuerzas para conseguir este bienestar... Dt 8, 17-18

El Señor ha puesto a lo largo de mi camino a muchas familias. Todas y cada una de ellas es parte de este producto final. Especialmente lo son la primera: Sonia, Marcela y Víctor Hugo; así como la última: Lili y los Guadalupe Salvador. Estas dos familias son parte de mi cotidianidad y han sido apoyo directo para la elaboración de este trabajo y para muchas otras cosas...

Acknowledgements

I would like to thank

- Conacyt (Consejo Nacional de Ciencia y Tecnología) for sponsoring my studies and stay in Mexico during this Ph.D. degree.

- CIMAT (Centro de Investigación en Matemáticas, A.C.) for helping me during this Ph.D. degree: administrative staff, researchers, teachers, and colleagues; particularly María Luisa Daza and Alessandro Bravetti for their support and the opportunity to collaborate with them.

- My advisor Marcos Capistrán for his guidance, work, patience, and financial support. Andrés Christen for his help, work, and financial support (RDCOMM grant). Antonio Capella for valuable discussions and for providing us his OGTT data.

- CONTEX for the financial support to travel to Oden Institute in UT Austin and multiple events; Tan Bui from Oden Institute for his time and valuable discussions. Also, I would like to thank especially to Brad Marvin, Ph.D. student from the Oden Institute for his work, patience, support, and his implementation of the GMRES for hIPPYlib.

Abstract

Inverse problems arise in an enormous variety of science and engineering applications where model parameters must be estimated from noisy and indirect observational data. These problems are characterized by observational errors, model errors, and issues of ill-posedness which yield uncertainties in model parameters. Bayesian statistical approaches to inverse problems allow us to make simulations and predictions with quantified uncertainties. These tasks become essential in model-based decision-making. Using a dynamical system based on physical principles to predict the observations is known as the forward problem. Traditional Bayesian methods as inference of the parameters, sampling from a distribution, quadrature approximations, experimental design, and model selection are affected by the introduction of a numerical solution of an ODE/PDE system. Therefore, ensuring the regularity of the direct problem, the consistency in the discretization, and the consequent stability of the posterior is of great importance to building reliable predictions. In this work, our specific interest relies on the challenges for the statistical approach for inverse problems defined by initial and boundary value problems for differential equations. We present several examples of inverse problems with applications in mesh refinement, elastography, epidemics, and biology. To face these problems,

we consider model selection criteria, experimental design strategies, posterior sampling schemes, among others in which we apply dimension reduction, optimization, and numerical analysis tools. The main goal illustrated by these examples is the systematic treatment of model, data, and computational errors to produce predictions with quantified uncertainty.

Keywords : Uncertainty Quantification, Bayesian Inverse Problems, ODEs/PDEs

Contents

Chapter 1

Introduction

Theoretically, mathematical models may be used to describe physical processes. The validation of these models from observations is fundamental in a predictive science process. Specify quantities of interest to predict will allow us to determine the important aspects of the physical process in which we must focus. In practice, we use computational models to implement this description and perform the computations. A verification process is designed to control possible errors in the discretization step of the theoretical mathematical model described. Inside these models, we found parameters of different classes which in the process may be taken from literature, may be proposed or may be inferred. The calibration step involves the tuning of parameters, which are commonly not known with great precision. After calibration, we obtain predictions of the model for our quantities of interest that may lead us to make decisions. But, how good are these predictions? The validation process is designed to built confidence in the predictions obtained from the model. Together these steps describe a systematic treatment of model, data, and computational errors to produce predictions with quantified uncertainty.

The inference of parameters based on observations is a very old problem with applications nowadays in medical imaging [1, 2, 3], geophysics [4, 5], epidemics [6], and others [7, 8, 9, 10]. Using a dynamical system based on physical principles to predict the observations is known as the forward problem. The

inverse problem corresponds to infer possible values for the parameter based on observations of this physical phenomenon. The solution of inverse problems can be viewed as the interpretation of data through a forward modeling that capture relationships between measured quantities and quantities of interest. Let us consider the problem of recovery θ from observations y given by

$$y = \mathcal{G}(\theta) \tag{1.1}$$

Assume that $\mathcal{G}(\theta)$ is given by the solution of a PDE/ODE system. From a traditional point of view, this problem is usually ill-posed. That means, a solution does not exist or multiple solutions may exist or solutions may not depend continuously on the data. To circumvent the ill-posedness, traditional methods formulate an optimization problem including a regularization term. A probabilistic approach considers θ as a random variable and the noise in the data. Under this approach, solving the inverse problem means to find a probability distribution for the parameter θ. Under the Bayesian paradigm, a probability distribution for the parameters is imputed as prior knowledge. By correcting this prior information with the data we obtain the posterior distribution. This approach introduces a regularization effect through the prior. By introducing probabilistic elements, equation (1.1) is replaced by

$$y = \mathcal{G}(\theta) + \eta \tag{1.2}$$

where an additive Gaussian noise η is assumed on the observations. Other structure for the noise may be considered.

A statistical approach for inverse problems introduces new components to propose solutions with quantified uncertainty and produce predictions. Implementation of computational models on the treatment of data uncertainties has become more usual and provides several challenges. Since $\mathcal{G}(\theta)$ corresponds to the solution of an ODE/PDE system, a numerical solver is required in practice. This requirement leads to a numerical version $\mathcal{G}_h(\theta)$ of $\mathcal{G}(\theta)$. In practice, all the simulations and analyses are performed with the numerical posterior $\pi_h(\theta|y)$ determined by $\mathcal{G}_h(\theta)$. Traditional Bayesian methods

as inference of the parameters, sampling from a distribution, quadrature approximations, and model selection are affected by the computational cost introduced by the numerical solution of an ODE/PDE system. Also, regularity conditions are needed to ensure that the numerical posterior $\pi_h(\theta|y)$ is a good approximation of the theoretical posterior $\pi(\theta|y)$. The study of linear problems allows to improve and implement new notions as MCMC sampling methods, experimental design, and goal-oriented inference using low-rank approximations, surrogates models, and optimization tools, [11, 12, 13].

In the specific case of recovering functions, the modeling on the representation of the function is directly related to the addressed strategies. Specifically, the well-posedness of the posterior in an infinite-dimensional setting is of paramount importance and is of current interest [14, 15, 16]. In [17], the well-posedness is addressed for inverse problems in machine learning where the regressor doesn't come from a dynamical system. The proper discretization of the infinite-dimensional problem is fundamental to ensure consistency and convergence,[18, 19]. Straightforward discretizations may lead to convergence problems due to not discretization-invariant schemes, as explained in [19, 20]. The Bayesian approach for recovering functions is significantly challenging since usually high dimensionality methods are required. MCMC methods are intractable under these conditions. Dimension reduction to implement MCMC methods for high dimensional problems is of current interest, [21] [22] [19]. A very popular tool to simplify the problem of high dimensionality is to compute a Gaussian approximation of the posterior distribution, [23]. This approach may be justified by the Berstein-Von-Misses theorem for the case of high dimensional data, see [24], [25], [26]. The Gaussian approximation of the posterior allows incorporating tools from the linear case studies as low-rank approximations, model selection, and goal-oriented inference. This approximation may be performed by linearizing the forward map around the MAP estimate, [23]. This approach proposes the posterior precision as a low-rank update of the prior precision where the spectra of the prior preconditioned Hessian misfit at the MAP reaches an invariance property under discretization. In this work, we analyze several uncertainty quantification strategies in different problems. The main contribution is for Bayesian model selection in the discretization of

parameter fields.

1.1 Previous work

Stuart introduced in [15] the Bayesian formulation for inverse problems in function spaces for Gaussian priors. The well-posedness of the posterior may be ensured for other priors too, see [14, 27, 28, 29]. The discretization of such formulation usually causes an inverse problem in high dimensions for the parameter, where conventional UQ methods fail. Dimension reduction has become an essential tool in tasks as the implementation of MCMC schemes [30], covariance matrices approximations [11, 23], and goal-oriented inferences [12, 31]. These dimension reductions may be formulated from the prior or the likelihood and may be implemented for both, the parameter and the state. As to the evaluation of the forward map, surrogate models have been applied to address the computational cost. Some approaches consider using polynomial chaos [32, 33], determine active subspaces [34, 35], or projection-based approaches [31]. Adaptative versions of the latter consider a data-driven implementation.

Authors in [23] address the large-scale problem for Bayesian inverse problems by approximating the posterior distribution by a Gaussian distribution. They propose the linearization of the forward map around the MAP estimate and apply this idea in the update of the posterior covariance. Also, they introduce a low-rank update of the posterior covariance based on the fact that data are informative in a low dimensional subspace of the parameter. Spantini *et al* in [11] introduce a class of loss functions to prove the optimality of the low-rank approximation of the posterior covariance based on the leading eigendirections of the prior preconditioned Hessian misfit. Authors in [18] propose a computational framework to discretize pde-constrained linearized problems in the finite element context. Similar approaches for MCMC are proposed in [7, 19].

The approximation of the posterior by the numerical/surrogate posterior is discussed for several cases [14, 31, 36, 37]. Authors in [14, 36, 38] focus on bayesian model selection based on Bayes Factors to analyze these

approximations. Some applications include determining the number of terms in a Fourier series or the resolution of an ODE solver. Another application that considers the resolution of the solver is mesh refinement/adaptivity. The refinement/adaptivity may be performed in the state and/or the parameter. Classical inversion approaches look for computational savings in the inference process. It has been demonstrated that parameter mesh refinement allows better reconstruction in regions of interest specifically in elastography applications [39, 40, 41]. Some approaches consider a posteriori error indicators to determine regions to refine/adapt the mesh [42, 43, 44]. Other strategies include variational mesh adaptation with a clustering technique [40], iteratively optimizing mesh connectivity and node positions [39], and high variance indicators of the strain (displacement/state) [41]. The Bayesian approach in this context is very challenging. The refinement/adaptivity in the state determines again a surrogate posterior that changes for each mesh. When performed in the parameter, the problem becomes more difficult since the refinement produces posterior distributions with different dimensions. How to compare these models take us back to Bayesian model selection, where some criteria as BIC, KL divergence, or Bayes Factors are the most popular strategies.

1.2 Contributions

The main contributions of this work are (1) The computation of the normalization constants for linear inverse problems for two problem types. The first problem considers the number of terms in a Fourier series. The second considers the low-rank approximation of the posterior on the big scale setting. Formulas for linearized models are proposed and apply to a nonlinear inverse problem governed by an elliptic pde. The ultimate goal of these calculations is to apply them in a model selection approach. In this case, a local refinement is performed and the computation of the normalization constants allows us to determine the best mesh. Also, we can compare several refinement criteria again by the computation of these normalization constants. (2) The comparison of two members of different families of transition kernels to perform the posterior distribution exploration in an inference problem

in 1D. HAMCMC is a Quasi-Newton method where proposals come from a continuous dynamic. T-walk is a sampler with the affine invariance property and free-derivate information. With an example that recovers four parameters, t-walk outperform HAMCMC. (3) The incorporation of elements of optimal experimental design in Multifrequency Algebraic Inversion with application to Magnetic Resonance Elastography. The aim is to decrease the uncertainty of the estimates in the AIDE inversion. This approach allows decreasing the variance out of the inclusion area. (4) A Bayesian approach to analyze Oral Glucose Tolerance Test data. The forward modeling considers Erlang distributions to reproduce the hormonal reaction to a sugary drink. From estimates of two parameters related to insulin production, we classify around 85% of 80 patients. These insulin indicators allow us to recognize possible alterations in healthy patients. (5) The inference for an ODE model that describes the early dynamics of the covid-19 in México. This approach considers possible infections through the environment and the estimation of its transmission rate. (6) The discretization of an accelerated scheme that preserves theoretical convergence rates with possible applications in optimization and machine learning.

1.3 Limitations and future work

The limitations of this work represent possibilities of future work: (1) The multimesh approach performs well for problems with a high signal-to-noise ratio (small noise). The modeling of the interpolation operators is of paramount importance to give consistency in the discretization and is part of future work. (2) The mesh refinement proposed allows us to obtain models with higher evidence and higher L^2 error with respect to the truth parameter. Explore other criteria with error indicators and uncertainty information is part of the future work. (3) To propose a fairer comparison between kernels, other examples should be included as one with high dimensional data or/and high dimensional parameter. (4) A more realistic solver that models the attenuation must be implemented to ensure the results on the optimal design of frequencies for the multifrequency AIDE inversion. (5) The forward modeling for the OGTT does not take account of possible insulin and glucagon measurement

data. This modification may improve the classification of patients. Future work contemplates how to adapt the model to incorporate insulin data. It is well known that the human body has a basal level of insulin and that insulin secretion follows pulsating patterns which represent new challenges in our modeling and the respective uncertainty quantification. (6) The modeling of the possible infections through the environment has no consequences on non-pharmaceutical interventions. Simpler models may be proposed to explore real scenarios. (7) The discretization that preserves theoretical convergence rates becomes computationally demanding as the order increases. This issue limits its application to machine learning tasks.

Chapter 2

Theoretical Framework

2.1 Well posedness of Bayesian inverse problem

According to [45], the objective of statistical inversion theory is to extract information and assess the uncertainty about the variables based on all available knowledge of the measurement process. In principle, under this approach, randomness describes our degree of information. All this information is coded in probability distributions. Finally, we obtain a (posterior) distribution as a solution to the inverse problem. In this section, we discuss the main elements of the formulation of the Bayesian inverse problem. First, we describe the formulation of the finite-dimensional setting using Bayes theorem. Then, we introduce some analysis elements to discuss the well-posedness in the infinite-dimensional setting. In the second case, Bayes formula makes sense from a Radon-Nikodym derivative.

2.1.1 Bayes' Theorem in $\mathbb{R}^n$

In the following and according to [45], we call the observable random variable Y *the measurement* and its realization, *the data*. The primary interest random variable X will be called *the unknown* or *the parameter*. Assume that before making the measurements of Y, we have some information about X. The

Bayesian framework assumes that this information can be codified under a probability density, $x \to \pi_{\text{pr}}(x)$ called *the prior density*. Now suppose that there exists a joint probability distribution for X and Y, denote by $\pi(x, y)$. Then, the marginal density for the unknown X is given by the formula

$$\int_{\mathbb{R}^m} \pi(x, y)dy = \pi_{\text{pr}}(x)$$

On the other hand, if we want the value of the unknown, then the conditional probability density of Y given X will be given by

$$\pi(y|x) = \frac{\pi(x, y)}{\pi_{\text{pr}}(x)}, \qquad \text{if } \pi_{\text{pr}}(x) \neq 0$$

We call the conditional probability of Y the *likelihood function* because it expresses the likelihood of different posible measurements given that $X = x$. Finally assuming that the observations $Y = y$ are given, the conditional probability distribution

$$\pi(x|y) = \frac{\pi(x, y)}{\pi(y)}, \qquad \text{if } \pi(y) = \int_{\mathbb{R}^n} \pi(x, y)dx \neq 0$$

will be called *the posterior distribution* of X. This distribution expresses what we know about X after the realization of observation $Y = y$.
Under the Bayesian approach, the inverse problem is expressed in the following way: *Given the data $Y = y$, find the conditional probability distribution $\pi(x|y)$ of the variable X*. The following result represents the main result of the theory

Theorem 2.1.1 (Bayes' Theorem) *Assume that the random variable $X \in \mathbb{R}^n$ has a known prior probability density $\pi_{pr}(x)$ and the data consist of the observed value y of an observable random variable $Y \in \mathbb{R}^k$ such that $\pi(y) > 0$. Then the posterior probability distribution of X, given the data y is*

$$\pi_{post}(x) = \pi(x|y) = \frac{\pi_{pr}(x)\pi(y|x)}{\pi(y)} \tag{2.1}$$

Now that we know of the existence of the solution of the inverse problem from the Bayesian approach, we would like to obtain some information about it. In

this work, we are considering models to fit the data that comes from the solution of a dynamical system (ODE/PDE). That means, to evaluate the likelihood, we need to solve the forward problem $\mathcal{F}(x)$. In this context, $\mathcal{F}$ typically is given by the numerical solution of a dynamical system. Just in a few cases, the posterior distribution has a close form. For example, it is well known in the literature the case that a Gaussian prior and a linear model produces a Gaussian posterior. Let $\pi_0(x) = \mathcal{N}(m_0, \mathcal{C}_0)$ and assume that the data y are given by

$$y = \mathcal{F}(x) + \eta = Ax + \eta, \qquad \eta \sim \mathcal{N}(0, \Gamma_{noise})$$

The conditional distribution of x given y is Gaussian $\pi(x|y) = \mathcal{N}(m, \mathcal{C})$ with

$$\mathcal{C} = A^T \Gamma_{noise}^{-1} A + \mathcal{C}_0^{-1} \tag{2.2}$$

and

$$m = \mathcal{C}(A^T \Gamma_{noise}^{-1} y + \mathcal{C}_0^{-1} m_0) \tag{2.3}$$

In this case, even if we have a close form, matrix A comes from the numerical solution of an ODE/PDE system. To get information from the posterior distribution, the more popular approach is by generating samples by a Monte Carlo method. This topic will be discussed in the next section. Regarding the existence of the posterior, the advantage of the finite-dimensional case lies in the existence of the Lebesgue measure and that the prior and posterior measures possess a density with respect to this Lebesgue measure. In infinite dimensions, there is not an equivalent measure as Lebesgue. In the next subsection, we discuss the main approach for the infinite-dimensional setting using Gaussian priors.

2.1.2 The infinite dimensional setting

An infinite-dimensional framework for Bayesian inverse problems is of current interest, specifically on a PDE-constrained formulation. In a finite-dimensional

setting for inverse problems, Bayes' rule is given by

$$\pi_{post}(m|y) = \frac{1}{Z}\pi_{like}(y|m)\pi_{prior}(m), \tag{2.4}$$

where $\pi_{post}(m|y)$ is the posterior distribution of the parameter m given the data y, $\pi_{like}(y|m)$ is the likelihood and $\pi_{prior}(m)$ is the prior distribution of m. Since in this case, all the quantities are in spaces of finite dimensions, all these distributions have a density with respect to the Lebesgue measure. This is the major drawback in the infinite-dimensional setting. From equation (2.4) we can deduce a more general relation between the measures μ^y and μ_0 defined by π_{post} and π_{prior}

$$\frac{d\mu^y}{d\mu_0}(m) = \frac{1}{Z(y)} \exp\left(-\Phi(m;y)\right). \tag{2.5}$$

This form, using the Radon-Nikodym derivative, generalizes readily Bayes' rule on a function space setting. Stuart in [15] highlights some properties of the map Φ, which are typically determined by the forward PDE problem, that is, the probability theory does not play a role in these properties. In the specific case where we consider

$$\Phi(m,y) = \frac{1}{2}|\Gamma_{noise}^{1/2}\left(y - \mathcal{G}(m)\right)|^2 = \frac{1}{2}|\left(y - \mathcal{G}(m)\right)|^2_{\Gamma_{noise}^{-1}}, \tag{2.6}$$

it is natural to derive the properties of Φ from the properties of $\mathcal{G}$. The typical assumption for $\mathcal{G}$ ([15, 29, 16, 17, 14]) is the Lipschitz continuity with respect to the parameter of interest.

***Assumptions* 1** *The function $\mathcal{G} : X \to \mathbb{R}^q$ satisfies that for every $r > 0$ there is a $K = K(r) > 0$ such that, for all $m_1, m_2 \in X$ with $\max\{||m_1||_X, ||m_2||_X\} < r$,*

$$|\mathcal{G}(m_1) - \mathcal{G}(m_2)|_\Gamma \leq K||m_1 - m_2||_X$$

After ensure or assume this property, the link to Bayesian inverse problems comes through the choice of the prior measure μ_0. Authors in [46] describe the construction of priors on separable Banach spaces using random series. This approach includes Gaussian, uniform, and Besov priors. A disintegration

approach to justify the well-posedness of the posterior distribution in function spaces can be found in [14, 47, 48]. In the following, we describe Stuart formulation [15] to the inverse problem using a Gaussian prior. The main properties of Gaussian distributions in a Hilbert/Banach space can be found in [49]. We start by recalling some properties that we use in this formulation.

***Proposition* 2.1.1** *If $\mathcal{N}(0, \mathcal{C})$ is a Gaussian measure on a Hilbert space $\mathcal{H}$, then $\mathcal{C}$ is self-adjoint, positive semi-definite trace-class operator on $\mathcal{H}$. Conversely, if $\mathcal{C}$ is a self-adjoint, positive semi-definite, trace-class linear operator on a Hilbert space $\mathcal{H}$, then there $\mu = \mathcal{N}(0, \mathcal{C})$ is a Gaussian measure on $\mathcal{H}$.*

From this proposition, it is important to note sufficient conditions to define a covariance operator. This operator is proposed in [15] through the idea of a negative power of a *Laplacian-like* operator. For example, consider a second-order differential operator $\mathcal{A}$ on a bounded open set $D \subset \mathbb{R}^d$, with domain chosen so that $\mathcal{A}$ is positive definite and invertible. For a detailed description of conditions on $\mathcal{A}$ see [15]. In this work, we focus on the property that the eigenfunctions/eigenvalues $\{\phi_k, \lambda_k\}_{k \in \mathbb{K}}$ of $\mathcal{A}$, with $\mathbb{K} \subset \mathbb{Z}^d \setminus \{0\}$, form an orthonormal basis of $\mathcal{H}$ and $\lambda_k \geq 0$ and satisfies a summability condition. With these assumptions, we can generate samples from a distribution $\mathcal{N}(0, \mathcal{C})$ by the KL expansion

Theorem 2.1.2 *Let $\mathcal{C}$ be a self-adjoint, positive semi-definite, nuclear operator in a Hilbert space $\mathcal{H}$ and let $m \in \mathcal{H}$. Let $\{\phi_k, \gamma_k\}_{k=1}^{\infty}$ be an orthonormal set of eigenvectors/eigenvalues for $\mathcal{C}$ ordered so that*

$$\gamma_1 \geq \gamma_2 \geq \cdots$$

Take $\{\xi_k\}_{k=1}^{\infty}$ to be an i.i.d. sequence with $\xi_1 \sim \mathcal{N}(0, 1)$. Then the random variable $x \in \mathcal{H}$ given by the Karhunen-Loeve expansion

$$x = m + \sum_{k=1}^{\infty} \sqrt{\gamma_k} \xi_k \phi_k \tag{2.7}$$

is distributed according to $\mu = \mathcal{N}(m, \mathcal{C})$.

Given conditions under the forward problem and the prior measure, let m be a random variable distributed according to the measure μ_0 on a separable Banach space X. Assume that the data $y \in \mathbb{R}^p$ are given in terms of an observation operator $\mathcal{G}$ by the formula

$$y = \mathcal{G}(m) + \eta \tag{2.8}$$

where η is independent of m and has density ρ. Then $m|y$ is distributed according to the probability measure for m given y, denoted by $\mu^y(dm)$, which is absolutely continuous with respect to $\mu_0(dm)$ and satisfies

$$\frac{d\mu^y}{d\mu_0}(m) \propto \frac{\rho(y - \mathcal{G}(m))}{\rho(y)} \tag{2.9}$$

Finally, one of the properties desired of the measure is to ensure some continuity of the samples. According to [15] using the Kolmogorov Continuity Theorem it can be prove the next lemma.

***Lemma* 2.1.1** *Let $\mathcal{A}$ satisfy laplacian-like assumptions in [15]. Consider a Gaussian measure $\mu = \mathcal{N}(0, \mathcal{C})$ with $\mathcal{C} = \mathcal{A}^{-\alpha}$ with $\alpha > d/2$. Then $u \sim \mu$ is almost surely s-Holder-continuous for any exponent $s < \min\{1, \alpha - d/2\}$.*

From this lemma, we can deduce that $\alpha = 1$ ensures the Holder continuity in a 1D problem, which is not the case for 2D or 3D. Considering $\mathcal{A}$ as the negative laplacian $(-\Delta\ )$ is a popular choice. A slight modification based on results in [15] was proposed by authors in [18] where

$$\mathcal{A} = \delta I - \gamma\Delta. \tag{2.10}$$

This operator belongs to a two-parameter family. As we mentioned before, from the connection to a common spatial statistics covariance matrix, we can propose the values of these parameters depending on the specific application. The link between Matérn prior covariance and the inverse power of a differential operator was established in [50]. Its authors define a Gaussian field with Matérn covariance under a stochastic partial differential equation. Since then, the use of a Matérn prior covariance becomes very common on Bayesian inverse problems,

[3, 51, 52, 53]. Following [50], the Matérn covariance function between locations $\mathbf{u}$ and $\mathbf{v} \in \mathbb{R}^d$ is defined as

$$r(\mathbf{u}, \mathbf{v}) = \frac{\sigma^2}{\Gamma(\nu)2^{\nu-1}} \left(\kappa||\mathbf{v}-\mathbf{u}||\right)^{\nu} K_{\nu} \left(\kappa||\mathbf{v}-\mathbf{u}||\right) \tag{2.11}$$

where K_ν is the modified Bessel function of second kind and order $\nu > 0$, $\kappa > 0$ is a scaling parameter and σ^2 is the marginal variance. The integer value of ν determines the mean square differentiability of the underlying process. A natural interpretation of the scaling parameter κ is as a range parameter ρ; the Euclidean distance where $x(\mathbf{u})$ and $x(\mathbf{v})$ is almost independent. An empirical derived definition is $\rho = \sqrt{8\nu}/\kappa$ and corresponds to correlations near 0.1 at the distance ρ. A Gaussian field $x(\mathbf{u})$ with the Matérn covariance is a solution to the linear fractional stochastic partial differential equation

$$\left(\kappa^2 - \Delta\right)^{\alpha/2} x(\mathbf{u}) = \mathcal{W}(\mathbf{u}), \qquad \alpha = \nu + d/2, \kappa > 0, \nu > 0 \tag{2.12}$$

The innovation process $\mathcal{W}$ is spatial Gaussian white noise with unit variance, and the marginal variance is

$$\sigma^2 = \frac{\Gamma(\nu)}{\Gamma(\nu + d/2)(4\pi)^{d/2}\kappa^{2\nu}} \tag{2.13}$$

Any solution of equation (2.12) is called a Matérn field. Authors in [3] propose a numerical approximation of the Whittle-Matérn prior using finite differences or finite elements. Given a Matérn prior as a stochastic partial differential equation, the finite element approach gives a discretization where the boundary conditions produce effects that break some properties of the Matérn. Some possible options to mitigate these effects are proposed in [3, 54]. The common approach is to impose Robin boundary conditions. Even if authors in [3] propose a fixed value for the robin coefficient based on numerical simulations, an optimization problem is solved in [54] to determine it. A domain extension or a normalization of the pointwise variance by rescaling the covariance operator are other possible solutions. It is important to note that the approach in [54] aims to build scalable solutions focus on large scale problems. We can see in figure (2.1)

two cases for the prior pointwise variance with different boundary conditions. Since a Matérn covariance satisfies that the marginal variance σ^2 is constant, it is clear that the case with Robin boundary conditions (figure (2.1)(b)) is more similar. Both articles pointed out that Neumann boundary conditions produce higher variance close to the boundary domain (figure (2.1)(a)) and the Dirichlet boundary produces lower variance close to the boundary domain. Since our work does not take into account the modeling on the boundary conditions, we try to mimic a Matérn covariance field, that is, a constant marginal variance.

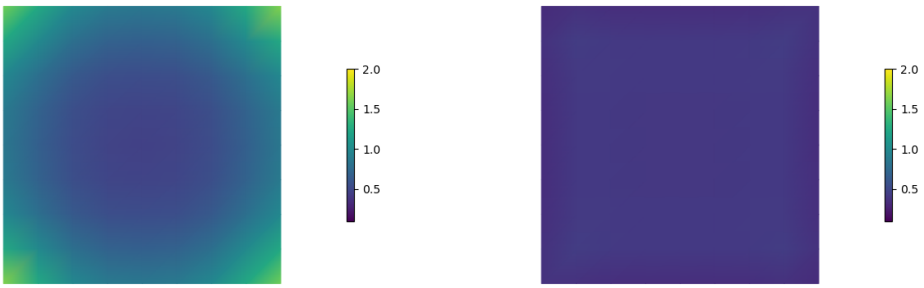

(a) (b)

Figure 2.1: Prior pointwise variance for $\gamma = 0.1, \delta = 2.0$ (a) Neumann boundary conditions. (b) Robin boundary conditions

Now, from the operator

$$\mathcal{A} = \delta I - \gamma \Delta \tag{2.14}$$

we propose the covariance operator $\mathcal{C}$ of a Gaussian measure as $\mathcal{C} = \mathcal{A}^{-2}$ guided by Lemma 2.1.1 for examples 2 and 3 in section 3. Since we work in dimension 2, we want to choose α satisfying $\alpha > d/2 = 1$. The choice of $\alpha = 2$ is convenient since this value makes easier the computations to generate samples. This case is implemented in the hIPPYlib library as the BiLaplacian prior, [55]. To propose the values for δ and γ in equation (2.14), we note the connection between these two parameters and the parameters from the Matérn approach:

$$\kappa^2 = \frac{\delta}{\gamma}, \qquad \alpha/2 = 2 \tag{2.15}$$

Since $d = 2$, we deduce that $\nu = 3$. Also,

$$\frac{\delta}{\gamma} = \frac{8\nu}{\rho^2} \tag{2.16}$$

According to [54], some computations leads to

$$\sigma^2 = \frac{\Gamma(\nu)}{\Gamma(\nu + d/2)(4\pi)^{d/2}\kappa^{2\nu}\gamma^{\nu+d/2}} \tag{2.17}$$

and by choosing a value for σ^2 and ρ, we can compute the value for γ and δ. A rectangular grid with possible values for ρ and σ^2 and its corresponding γ and δ values are shown in Figure (2.2) After make clear this connection, both

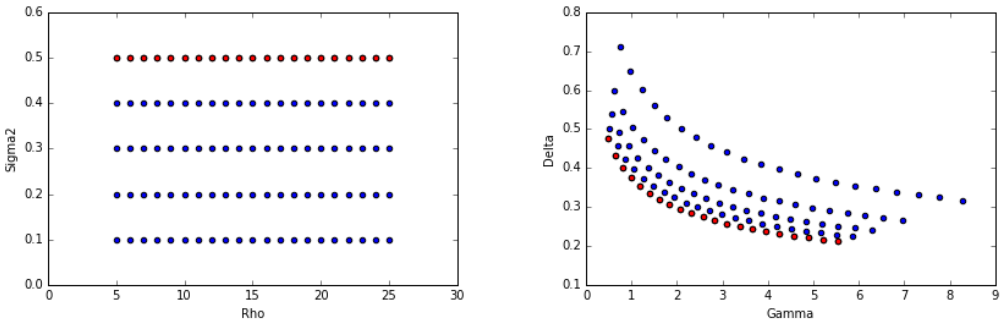

(a) (b)

Figure 2.2: Rectangular grid for possible values of ρ and σ^2 at left. Corresponding values of γ and δ at right.

values of ρ and σ^2 will depends on the specific application. To exemplify this statement, let us consider the case of liver MRE. To propose the value of ρ, we consider that the larger dimension of the liver is around 16 cm. To propose the value of σ^2 we consider that the specific application classifies all the fibrosis stages (4 stages) between a healthy liver ($\approx$ 2.0 KPa of stiffness) and a cirrhotic liver ($\approx$ 8.0 KPa of stiffness), see [56] for more details. That means, the choice of σ^2 must be proposed considering the range between stages, which is around 1.5 KPa.

Once we have ensured the posterior well-posedness, we need to perform computations with a numerical version of this posterior. Strategies to generate

samples from the posterior distribution can vary depending on the dimension of the parameter. Another advantage of a prior covariance given by equation (2.10) is the possibility of making profit of PDE solvers for elliptic equation. This tool allows us to generate samples from the prior in a very efficient way, see [18] for more details. It is well known that as the dimension increase, the performance of Monte Carlo becomes poor. In the next section, we describe two different approaches to perform this task. An affine invariant perspective may be very effective to get samples from the posterior in low dimensions. A dynamical proposal including derivative information may improve the performance of the Monte Carlo for high dimensions despite the possible limitation of sampling from multimodal distributions. Before that, in the next subsection, we discuss some results about the approximation of the theoretical posterior by its numerical version.

2.1.3 Posterior consistency

Having ensured the well-posedness of the posterior distribution for the Bayesian inverse problems, we are concerned with the numerical version of the posterior used to perform the computations. The posterior consistency may include (i) the analysis of the small noise limit [15, 57, 58], (ii) the stability of the posterior under data and likelihood perturbations [59, 60], (iii) the convergence rates of the finite- dimensional approximation of the posterior [37], (iv) the error bounds for approximate posteriors [61, 62]. As we mention before, we are interested in problems where the forward modeling comes from a dynamical system, that is, an ODE/PDE system. Numerical solvers are required since these systems usually do not have an explicit solution. Given a theoretical map $\mathcal{G}(m)$, we have a numerical version $\mathcal{G}_h(m)$ produced by the solver where h denotes some discretization level. This numerical regressor defines a numerical posterior $\pi_h(m|y)$. The posterior consistency allows us to analyze how and in what sense $\pi_h(m|y)$ approximates $\pi(m|y)$ [14]. To perform this analysis, a suitable notion of distance must be chosen. The Total Variation and Hellinger distances are the more popular choices. Hellinger's provides a bound for TV and the error in expected values [37, 62]. Authors in [63] illustrate how the choice of

a metric can affect rates of convergence. Authors in [36] propose Bayes factors as a measure to compare a theoretical model and its numerical approximate model in the context of ODEs governing equations. The main result lies in the error truncation of the numerical solver to evaluate the likelihood. The order of the solver determines the behavior of the Bayes factors. These results allow illustrating how the step size to solve the ODE system may be chosen. Specifically, the step size must be chosen such that the global error is small with respect to the noise level. Authors in [14] make use of weak convergence for the consistency of the numerical approximated posterior and the TV norm for the rates of convergence. In this case, the posterior well-posedness in infinite dimensions is ensured under a disintegration approach. Again, the consistency of the numerical approximation of the posterior is related to the order of the numerical solver for the ODE/PDE as was explained in [36]. Some rates of convergence consider the prior truncation too.

2.2 Sampling from the posterior

After being guaranteed the existence of the posterior density, we need to explore it. For that, we will use a Markov Chain Monte Carlo (MCMC) method. Markov Chain Monte Carlo (MCMC) methods provide systematic ways of generating samples from a target distribution $\pi(\theta)$. The main advantage of Monte Carlo methods is that we can sample from a probability measure only known up to a normalizing constant. The main limitation of this approach is that Monte Carlo methods deteriorate with the increase of the dimension of the parameter. In this subsection, we describe the main properties of Monte Carlo methods. Also, we will mention specific strategies for the sampling of a posterior corresponding to a discretized infinite-dimensional problem.

The basic idea is to design a Markov chain with the property that a single sequence of output for the chain $\{x_n\}_{n=0}^{\infty}$ is distributed according to the posterior measure μ associated with $\pi(x|y)$. We will say that this Markov Chain, with $x \in E$, is aperiodic and irreducible and has stationary distribution $\pi(x|y)$. E is called the support of x and is directly related to the support of our prior. Nevertheless, if $E \subset \mathbb{R}^n$, we need to determine *representative* points since, in practice, we can not sample all the domain. That selection will be made by the density itself. As [45] explains, to generate a chain with stationary distribution π, we need to find a transition kernel that verifies ergodicity conditions: aperiodicity, irreducibility, and the measure μ associated to π should be invariant under P.

The way that the chain *jump* from a state x_i to the next state x_{i+1} is determined by a transition kernel. Following [45], let P be a probability transition kernel. P is a map from $\mathbb{R}^n \times \mathcal{B} \to [0,1]$, where $\mathcal{B}$ denotes the Borel sets of $\mathbb{R}^n$. Then $P(x_i, A_{i+1})$ is the probability that the chain $X \in A_{i+1}$ conditioned that the state of X is x_i. P is related to the measure μ by

$$\mu_{X_{j+1}}(A_{j+1}|x_1, \ldots, x_j) = \mu_{X_{j+1}}(A_{j+1}|x_j) = P(x_j, A_{j+1}) \tag{2.18}$$

If $P^{(k)}(x_j, B_{j+k})$ denotes the transition kernel that propagates k steps forward in time, we will say that P is *irreducible* if for each $x \in \mathbb{R}^n$ and $A \in \mathcal{B}$, with

$\mu(A) > 0$, then there exist $k > 0$ such that $P^{(k)}(x, A) > 0$.
On the other hand, for stating the property of aperiodicity, we will define what a periodic kernel is. P is *periodic* if for some integer $m \geq 2$, there is a set of disjoint nonempty sets $\{E_1, \ldots, E_m\} \subset \mathbb{R}^n$ such that for all $j = 1, \ldots, m$ and all $x \in E_j$, $P(x, E_{j+1(\text{mod } m)}) = 1$. A kernel P is aperiodic if it is not periodic.

The probability transition kernel can be defined through a dynamical system as Ma *et al.* [64] explained. According to Ma *et al.*, the idea of sampling from the posterior then becomes simulating from continuous dynamics. However, as indicated above, there are infinitely many ways to define a probability transition kernel P. The construction of this transition kernel can vary relating to the observation operator, prior, and noise distributions. In the following subsections, we focus on two specific types of transition kernels: affine invariant and dynamical gradient informed.

2.2.1 Affine invariant samplers

Highly anisotropic distributions are targets hard to sample with MCMC. For this kind of distribution, having a kernel invariant to affine transformations can alleviate the difficulties. This notion was introduced for Monte Carlo methods in [65, 66, 67]. This property implies that the performance of the MCMC remains independent of the aspect ratio of the target distribution. To design an affine invariant kernel may be natural in specific applications as inverse scattering, see [68, 69]. According to [66], consider a sampler of the form $X(t+1) = R(X(t), \xi(t), \pi)$, where $X(t)$ is the sample after t iterations, $\xi(t)$ is a sequence of iid random variables and π a probability density. The algorithm is affine invariant if

$$R(Ax + b, \xi(t), \pi_{A,b}) = AR(x, \xi(t), \pi) + b \tag{2.19}$$

where $\pi_{A,b}(z) = \pi_{A,b}(Ax + b) \propto \pi(x)$. For example, if

$$\pi(x) \propto \exp\left(-\frac{(x_1 - x_2)^2}{2\epsilon} - \frac{(x_1 + x_2)^2}{2}\right) \tag{2.20}$$

then

$$\pi_A(y) \propto \exp\left(-\frac{y_1^2 + y_2^2}{2}\right) \tag{2.21}$$

with

$$A = \begin{pmatrix} \frac{1}{\sqrt{\epsilon}} & -\frac{1}{\sqrt{\epsilon}} \\ 1 & 1 \end{pmatrix} \tag{2.22}$$

An affine invariant sampler recognizes densities in 2.20 and 2.21 equally difficult. In this work, we will use *twalk* several times. T-walk is an MCMC sampler for arbitrary continuous distributions presented in [65]. The t-walk maintains two independent points in the sample space where all moves are based on proposals that are then accepted with a standard M-H acceptance probability on the product space. For an objective function $\pi(\theta)$, $\theta \in \mathcal{X}$, the sampler forms the new objective function $f(\theta, \theta') = \pi(\theta)\pi(\theta')$ on the corresponding product space $\mathcal{X} \times \mathcal{X}$. The rationale of this approach is to introduce a notion of scale with the product space. This property is justified by the following theorem

Theorem 2.2.1 *Let $V \in \mathcal{X} \times \mathcal{X}$ and $A \subset \mathcal{X} \times \mathcal{X}$. Let $\phi(z) = ax + b, a \in \mathbb{R}, a \neq 0, b \in \mathbb{R}^n$. The t-walk transition kernel using objective $\lambda(z) = |a^{-n}|\pi(\phi^{-1}(z))$, K_λ, and the t-walk kernel using objective π, K_π, have the invariance property*

$$K_\lambda(\phi(V), \phi(A)) = K_\pi(V, A) \tag{2.23}$$

The proof can be found in [65].

2.2.2 Dynamical gradient informed samplers

In high dimensions, methods as random walk become inefficient, with low acceptance rates, poor mixing (slow rate exploration), and highly correlated samples, see [70]. Design a good general-purpose proposal mechanism remains of active research. An approach that may circumvent these issues is when the proposal is derived from a discretized Langevin equation. Specifically, in [70], the authors suggested a proposal from a discretized Langevin diffusion with a drift term based on gradient information from the target. This method was named Metropolis Adjusted Langevin Algorithm (MALA). Another similar method was born in the field of molecular dynamics. This method suggested

a proposal in the setting of Hamiltonian dynamics. Initially named by Hybrid Monte Carlo (HMC), it would later become popular as Hamiltonian Monte Carlo. Despite the issues that these methods try to solve, they still have majors problems related to the tuning parameters.

For the case of MALA and a target density $p(\theta)$, the proposal is build by a first order Euler discretization of the SDE

$$d\theta(t) = \nabla_\theta \mathcal{L}(\theta(t))dt/2 + db(t) \tag{2.24}$$

which become

$$\theta^* = \theta^n + \epsilon^2 \mathbf{M} \nabla_\theta \mathcal{L}(\theta^n)2 + \epsilon\sqrt{\mathbf{M}} z^n \tag{2.25}$$

where $\mathcal{L}(\theta) \equiv \log p(\theta)$, $\mathbf{M}$ is used as a preconditioning matrix, ϵ is the integration step size and $z \sim \mathcal{N}(0, I)$. This discretization doesn't satisfy the invariance of the distribution. Typically, a Metropolis acceptance criterion may be included to correct this situation. We can find different approaches using equation (2.25), specifically, the proposal of the preconditioning matrix $\mathbf{M}$ typically is related to well-known optimization and numerical linear algebra literature, see for example [71, 72, 73, 7].

In the Hamiltonian approach, a way to tackle the problem of the invariance of the distribution is to add an extra term to the dynamics. This approach was introduced in [64] in a stochastic gradient approach. This extra term is a correcting term to ensure that the posterior distribution is the stationary distribution. From equation

$$dz = f(z)dt + \sqrt{2D(z)}dW(t) \tag{2.26}$$

consider $f(z)$ as

$$f(z) = -\left[D(z) + Q(z)\right]\nabla H(z) + \Gamma(z), \qquad \Gamma_i(z) = \sum_{j=1}^{d} \frac{\partial}{\partial z_j}\left(D_{ij}(Z) + Q_{ij}(z)\right) \tag{2.27}$$

where matrices $D(z)$ and $Q(z)$ can be adjusted to improve convergence ($D(z)$ positive semidefinite and $Q(z)$ skew-symmetric). In the following we will

describe HAMCMC, a sampler based in this rationale.

HAMCMC

Let $U(x) = -\log \pi(\theta)$, where $\pi(\theta)$ represents the target distribution as before. HAMCMC is introduced in [74] as follows. HAMCMC applies the following update rule for generating samples from the posterior distribution:

$$\theta_t = \theta_{t-M} - \epsilon_t H_t \left(\theta_{t-2M+1:t-1}^{\neg(t-M)} \right) \nabla U(\theta_{t-M}) + \eta_t \tag{2.28}$$

where $\theta_{a:b}^{\neg c} \equiv \{\theta_a, \theta_{a+1}, ..., \theta_{b-1}, \theta_b\} \setminus \{\theta_c\}$, $\eta_t \sim \mathcal{N}(0, 2\epsilon_t H_t(\cdot))$, based on the L-BFGS optimization algorithm with some modifications. H_t is an approximation of the inverse Hessian. Usually, the L-BFGS algorithm computes H_t by using the M most recent values of the past iterates. In this case, HAMCMC uses history samples for this approximation:

$$\theta_{t-2M+1:t-1}^{\neg(t-M)} = \{\theta_{t-2M+1}, \ldots, \theta_{t-M-1}, \theta_{t-M+1}, \ldots, \theta_{t-1}\}.$$

Since the inverse Hessian is approximated without including θ_{t-M} in the computations, the correction term $\Gamma(\theta)$ in equation (2.27), presented in [64] to ensure the convergence to the posterior, vanishes.

2.3 Gaussian approximation of the posterior

A Laplace approximation of the posterior is a Gaussian approximation of the distribution. It is well known that a Gaussian prior and a linear forward map produce a Gaussian posterior, see [15]. If the forward map is not linear, a way to obtain a Gaussian approximation of the posterior is by linearizing the forward problem. To follow this approach, an estimator of the posterior, typically the MAP estimate, is needed. After that, we apply explicit formulas to compute the posterior precision as an update of the prior precision. Authors in [23] propose this idea for high dimension uncertainty quantification problems. Consider the case with a model observation given by

$$y = f(m) + e \tag{2.29}$$

with y the data and m the parameter to recover. The map of parameter-to-observable f is defined implicitly by the solution of a PDE problem. To linearize this map, we compute the MAP (maximum a posteriori) estimate. Recall that

$$m_{\text{MAP}} = \arg\min V(m) \tag{2.30}$$

where $V(m)$ typically corresponds to the minus log posterior. Again, it is important to note that to evaluate $V(m)$ we need to evaluate the minus likelihood, that is, we need to solve the forward problem f in equation (2.29). In the next subsection, we will explain in detail the PDE-constrained optimization approach used to approximate m_{MAP}. The next step is to approximate f around m_{MAP} by a first-order Taylor expansion

$$f(m) \approx \tilde{f}(m) = f(m_{\text{MAP}}) + F(m - m_{\text{MAP}}) \tag{2.31}$$

where F is the Jacobian of f evaluated at m_{MAP}. All the computations for this Gaussian approximation may be performed in hIPPYlib, see [55].

Before presenting the details of this approach, we should discuss some aspects of why it is required this approximation instead of considering the true posterior. For high dimensional problems, typical uncertainty

quantification strategies are prohibitive, inefficient, or inaccurate. The Gaussian approximation of the posterior may provide information for high dimensional parameter with an efficient approach and a well understanding of the accuracy. The Bernstein-von Misses theorem is a result giving conditions under which the posterior distribution is asymptotically normal, centered at the maximum likelihood estimator (MLE) of the model used [75]. For instance, Bernstein-von Misses theorems are difficult to derive in complex models and other centering can be used. We can subdivide these theorems into three categories. The parametric models, for which the results are well-known, see [76], the nonparametric models where the parameter space is infinite-dimensional or growing, and the semiparametric models when the parameter of interest is a finite-dimensional functional of the complete infinite-dimensional parameter. In the context of Bayesian inverse problems several works approach this topic under the small noise limit, increasing data size, and numerical robustness for concentrated posterior where the efficiency of prior based approaches is compromised [26, 24, 25].

2.3.1 Approximation of the MAP estimate

To compute the MAP estimate, we solve an optimization problem. We follow the well known pde constrained optimization approach [4, 77]. In this case, we want to implemented a Newton method. To achieve this goal, we need expressions for the gradient and the Hessian of the function to be optimize. Consider the problem of minimizing the functional

$$\mathcal{J}(m) = \frac{1}{2}||y - f(m)||^2_{\Gamma^{-1}_{obs}} + \frac{1}{2}||\mathcal{A}(m - m_0)||^2_{L^2} \tag{2.32}$$

where $f(m)$ is the solution of a pde system. From the pde-constrained approach, we can construct a funtional to compute m_{MAP} that consider the condition of satisfying the pde solution. Now, we propose a Lagrangian formulation given by the problem of minimizing

$$\mathcal{L}(u, p, m) = \frac{1}{2}\int_{\mathcal{X}} (y - u)^T \Gamma^{-1}_{obs} (y - u)\, dx + \frac{1}{2}||\mathcal{A}(m - m_0)||^2_{L^2} + a(u, p) - L(p) \tag{2.33}$$

where $a(u,p)$ and $L(p)$ are given by the weak formulation of the pde system. We follow the approach of optimize then discretize. This is, we consider the first order optimality conditions computed from equation (2.33) and then we discretize these quantities. To determine the first order optimality conditions, consider the first variations of $\mathcal{L}$ with respect each of its variables

$$\delta_p \mathcal{L}(u,p,m)(\tilde{p}) = 0 \tag{2.34}$$

$$\delta_u \mathcal{L}(u,p,m)(\tilde{u}) = 0 \tag{2.35}$$

$$\delta_m \mathcal{L}(u,p,m)(\tilde{m}) = 0 \tag{2.36}$$

Let us recall the definition of first variation. Set

$$\pi(u) = \mathcal{L}(u,p,m) \tag{2.37}$$

The first variation of π with respect to u in the direction of $\tilde{u}$ is given by

$$\delta_u \pi(u)(\tilde{u}) = \lim_{\varepsilon \to 0} \frac{\pi(u+\varepsilon\tilde{u}) - \pi(u)}{\varepsilon} = \frac{d}{d\varepsilon}\left[\pi(u+\varepsilon\tilde{u})\right]_{\varepsilon=0} \tag{2.38}$$

This first variation is also known as the Gateaux derivative, which in fact is a generalization of the concept of directional derivative. It is important to note that $u+\varepsilon\tilde{u}$ must belong to the same space than u. In this case, u and $u+\varepsilon\tilde{u}$ must satisfy the same boundary conditions from the forward problem. Under this approach, we define the gradient as

$$\mathcal{G} = \delta_m \mathcal{L}(u,p,m)(\tilde{m}) \tag{2.39}$$

Far from trying to solve all three conditions simultaneously, we focus in solve equation (2.36) using solutions from equations (2.34) and (2.35). Equation (2.34) determines the forward problem, equation (2.35) determines the adjoint problem. Finally, to evaluate the gradient action we need to solve the forward and adjoint problems.

To evaluate the action of the Hessian $\mathcal{H}$, we consider the meta-Lagrangian

$$\mathcal{L}^H(u,m,p;\hat{u},\hat{m},\hat{p}) := \mathcal{G} + \text{forward} + \text{adjoint} \tag{2.40}$$

Considering the first variations of $\mathcal{L}^H$ we can determine the Hessian $\mathcal{H}$ in a weak form.

$$\delta_p \mathcal{L}^H(u, m, p; \hat{u}, \hat{m}, \hat{p})(\tilde{p}) = 0 \tag{2.41}$$

$$\delta_u \mathcal{L}^H(u, m, p; \hat{u}, \hat{m}, \hat{p})(\tilde{u}) = 0 \tag{2.42}$$

$$\delta_m \mathcal{L}^H(u, m, p; \hat{u}, \hat{m}, \hat{p})(\tilde{m}) = \mathcal{H} \tag{2.43}$$

Equation (2.41) determines the incremental forward problem, equation (2.42) determines the incremental adjoint problem and the hessian is given by $\mathcal{H}$. Numerically, to evaluate the hessian action is needed to solve the forward and adjoint problems, the incremental forward and adjoint problems. The Newton method computes an update direction $\hat{m}_k$ by solving the linear system

$$(\tilde{m}, \mathcal{H}(m_k)(\hat{m}_k)) = -\mathcal{G}(m_k)(\tilde{m}) \tag{2.44}$$

The Newton system is solved inexactly by early termination of CG iterations via Eisenstat-Walker(to prevent oversolving) and Steihaug (to avoid negative curvature) criteria. We choose Armijo backtracking line search as the globalization technique. All our computations are in hIPPYlib [55] which provides a robust implementation of the inexact Newton-conjugate gradient algorithm to compute the maximum a posterior (MAP) point. The gradient and Hessian actions are computed via their weak form specification in FEniCS.

Discretization of the equation (2.44) is given by the linear system

$$H_k \hat{m}_k = -g_k \tag{2.45}$$

Where H_k corresponds to the discretization of the Hessian and g_k of the gradient. To evaluate g_k, we need to solve the forward problem

$$A_k u_k = f \tag{2.46}$$

and the adjoint problem

$$A_k^T p_k = -W_{uu}(u_k - u_d) \tag{2.47}$$

where u_k is the solution of the forward problem, W_{uu} is the mass matrix corresponding to the L^2 inner product and u_d are the data. Then the gradient expression is given by

$$g_k = Rm_k + C_k^T p_k \tag{2.48}$$

where R is the matrix from the discretization of the first variation on the prior distribution and C_k corresponds to the discretization of the first variation of the pde constraint with respect to the parameter m. The Hessian action is defined by

$$\begin{aligned} H_k\hat{m} = \quad & (R + W_{mm})\hat{m} + \\ & \left(C_k^T A_k^{-T}\left(W_{uu}A_k^{-1}C_k - W_{um}\right) - W_{mu}A_k^{-1}C_k\right)\hat{m} \end{aligned} \tag{2.49}$$

which can be divided in the **Hessian of the regularization**

$$R + W_{mm} \tag{2.50}$$

and in the **Hessian of the data misfit**

$$C_k^T A_k^{-T}\left(W_{uu}A_k^{-1}C_k - W_{um}\right) - W_{mu}A_k^{-1}C_k \tag{2.51}$$

where the terms W_{mm}, W_{um} and W_{mu} corresponds to second variations of the forward problem. Since the convergence of the Newton step can be ensured just in a neighborhood of the minimum, sometimes it is better to use a less informative proposal to start the optimization. In this case, we use a Gauss-Newton approximation for the Hessian obtained by dropping the operators W_{um}, W_{mm} and W_{mu}. In this case, the Gauss-Newton hessian actions is

$$H_k^{GN}\hat{m} = R\hat{m} + C_k^T\hat{p} \tag{2.52}$$

A discussion around the limitations and benefits of using GN approximation of the Hessian matrix can be found in [78].

2.3.2 Gaussian approximation of the posterior covariance

A Gaussian prior distribution and a linear model to fit the data, as in equation (2.31), results in a Gaussian posterior distribution. It is well known that the posterior precision matrix can be computed as an update of the prior precision matrix. Using this formula, authors in [23] introduces the prior-preconditioned Hessian of the data misfit in a factorization for the posterior covariance

$$\Gamma_{post} = \left(F^T\Gamma_{obs}^{-1}F + \Gamma_{prior}^{-1}\right)^{-1} \tag{2.53}$$

$$= \Gamma_{prior}^{1/2}\left(\Gamma_{prior}^{1/2}F^T\Gamma_{obs}^{-1}F\Gamma_{prior}^{1/2} + I\right)^{-1}\Gamma_{prior}^{1/2} \tag{2.54}$$

$$= \Gamma_{prior}^{1/2}\left(\tilde{H}_{misfit} + I\right)^{-1}\Gamma_{prior}^{1/2}. \tag{2.55}$$

From the properties of the prior covariance operator, inherit in the prior covariance matrix, and the fact F typically behaves as the discretization of a compact operator, authors in [23] propose a low rank approximation of this matrix

$$\Gamma_{prior}^{1/2}F^T\Gamma_{obs}^{-1}F\Gamma_{prior}^{1/2} \approx V_r\Lambda_r V_r^T \tag{2.56}$$

where V_r constains only the r eigenvectors of $\tilde{H}_{misfit}$ corresponding to the r largest eigenvalues λ_i, and $\Lambda = \text{diag}(\lambda_i)$. In our work, it is important to note that the value of r should not depend on the resolution of the mesh which is very important when establishing the initial resolution. Also F, the Jacobian of f, is formally a dense matrix. This update take advantage that the action of F and F^T on a vector can be formed by solving a linearized forward and a linearized adjoint PDE, which is very convenient on high dimension problems.

More recent work [11] introduce the notion of optimal approximation based on a low-rank update of the prior covariance matrix and an update based on the leading eigendirections of the pencil $(H_{\text{misfit}}, \Gamma_{prior}^{-1})$.

In hIPPYlib [55], the posterior covariance is approximated by the inverse of the Hessian of the negative log posterior evaluated at the MAP point. This Gaussian approximation is exact when the parameter-to-observable map is linear as we mentioned before. In the nonlinear case, the posterior precision

agrees to two derivatives with the minus log posterior at the MAP point, and thus it can serve as a proposal for Hessian-based Markov chain Monte Carlo (MCMC) methods, as in [71], [72], [7] and [73].

hIPPYlib makes the construction of the posterior covariance tractable by invoking a low-rank approximation of the Hessian of the log-likelihood. To compute this low rank decomposition of the prior preconditioned hessian, hIPPYlib implements algorithms from results in [79] and [80] to approximate the solution for Hermitian Eigenvalues Problems (HEP) and Generalized Hermitian Eigenvalues Problems (GHEP). As explained in [23], to approximate the spectral decomposition of a matrix $\mathbf{A} \in \mathbb{R}^{n\times n}$, first we generate a random matrix $\mathbf{R} \in \mathbb{R}^{n\times r}$, where $r \ll n$ with i.i.d. Gaussian entries. Set $\mathbf{Y} = \mathbf{AR}$. If $\mathbf{Q}$ is an orthogonal basis for $\mathbf{Y}$, the single-pass algorithm in [79] compute $\mathbf{B}$, an approximation of $\mathbf{A}$ in the base $\mathbf{Q}$:

$$\mathbf{B} := \left(\mathbf{Q}^T\mathbf{Y}\right)\left(\mathbf{Q}^T\mathbf{R}\right)^{-1} \approx \mathbf{Q}^T\mathbf{AQ} \tag{2.57}$$

Note that $\mathbf{B}, \mathbf{Q}^T\mathbf{Y}$ and $\mathbf{Q}^T\mathbf{R}$ are in $\mathbb{R}^{r\times r}$, Then $\mathbf{B}$ can be decomposed as $\mathbf{Z\Lambda Z}^T$ using dense linear algebra. Finally,

$$\mathbf{A} \approx \mathbf{V\Lambda V}^T \tag{2.58}$$

with $\mathbf{V} = \mathbf{QZ}$. The double-pass algorithm describe in [79], compute the product $\mathbf{B} = \mathbf{Q}^T\mathbf{AQ}$ instead of the approximation in equation 2.57. Note that the matrix $\mathbf{Q}$ comes from a QR decomposition of $\mathbf{Y}$. According to [79], the aim is to compute the matrix $\mathbf{Q}$ to contain as few columns as possible but with high accuracy in the approximation

$$\mathbf{A} \approx \mathbf{QQ}^T\mathbf{A} \tag{2.59}$$

This task can be executed very efficiently with random sampling methods. Authors in [79] proposed some algorithm (see Section 4, Stage A) that given some tolerance ε, a matrix $\mathbf{Q}$ is compute satisfying

$$||\mathbf{A} - \mathbf{QQ}^T\mathbf{A}|| < \varepsilon \tag{2.60}$$

with some probability. Deterministic methods as Givens rotations and Householder reflectors can be applied too regarding the dimension n. Once we have the matrix $\mathbf{Q}$, the approximation in equation 2.57 may be completed with deterministic methods for the single or double pass algorithm. In our case study, the matrix $\mathbf{A}$ corresponds to the prior preconditioned Hessian given in 2.56. Each matrix vector product requires the solution of a pair of linearized forward/adjoint problems (to compute the action of F and F^T) and a pair of elliptic operator solves (to compute the action of $\Gamma_{prior}^{1/2}$).

2.3.3 Discretization of the inverse problem using the Finite Element Method (FEM)

An infinite dimensional inverse problem is characterized by dificulties under discretization. It is important to ensure convergence to solutions of the infinite-dimensional problem and to built scalable algorithms for the manipulation of very large parameter dimension problems. Of course, as we mentioned two subsections before, the beginning is to establish the well-posedness of the infinite dimensional bayesian inverse problem through a prior measure and regularity properties of the forward problem. Once we have establish the infinite dimensional problem, the discretized parameter space is high dimensional. Following [18], we will describe a computational framework for infinite dimensional Bayesian inverse problems. In the context of a finite element discretization, the finite dimensional space that approximates the function space is built from continuous Lagrange basis functions. Consider the finite-dimensional subspace $V_h \subset L^2(\Omega)$ originate from a finite element discretization with continuous Lagrange basis functions $\{\phi_j\}_{j=1}^n$. To a function $m \in L^2(\Omega)$ corresponds an approximation $m_h = \sum_{j=1}^{j=n} m_j \phi_j \in V_h$. We denote by $\boldsymbol{m} = (m_1, m_2, \cdots, m_n)^T$ the nodal vector of m_h. The next step is to give sense to the inner product that approximate $L^2(\Omega)$ inner product. Note that for $m_1, m_2 \in L^2(\Omega)$,

$$(m_1, m_2)_{L^2} \approx (m_{1h}, m_{2h})_{L^2} = (\boldsymbol{m}_1, \boldsymbol{m}_2)_{\boldsymbol{M}} = \boldsymbol{m}_1^T \boldsymbol{M} \boldsymbol{m}_2 \tag{2.61}$$

with $\boldsymbol{M}$ the finite element mass matrix defined by

$$\boldsymbol{M}_{ij} = \int_{\Omega} \phi_i \phi_j dx, \qquad i,j \in \{1,\ldots,n\} \tag{2.62}$$

The inner product $(\cdot,\cdot)_{\boldsymbol{M}}$ corresponds to a $\boldsymbol{M}-$weighted inner product in the usual euclidean space $\mathbb{R}^n$ denote by $\mathbb{R}^n_{\boldsymbol{M}}$. With this distinction between euclidean spaces, another specification needed is the differences between adjoint matrix and transpose matrix. Consider an operator $\boldsymbol{B} : \mathbb{R}^n_{\boldsymbol{M}} \to \mathbb{R}^n_{\boldsymbol{M}}$. The transpose matrix denote by $\boldsymbol{B}^T$ is given by $\boldsymbol{B}^T_{ij} = \boldsymbol{B}_{ij}$. On the other hand, the adjoint $\boldsymbol{B}^*$ must satisfy

$$(\boldsymbol{B}^* m_1, m_2)_{\boldsymbol{M}} = (m_1, \boldsymbol{B} m_2)_{\boldsymbol{M}}, \qquad \forall m_1, m_2 \in \mathbb{R}^n_{\boldsymbol{M}} \tag{2.63}$$

This implies that

$$\boldsymbol{B}^* = \boldsymbol{M}^{-1}\boldsymbol{B}^T\boldsymbol{M} \tag{2.64}$$

Other adjoint actions that we must consider are the adjoint $\mathbf{F}^\star$ of $\mathbf{F} : \mathbb{R}^n_{\mathbf{M}} \to \mathbb{R}^q$ and $\mathbf{V}^\diamond$ of $\mathbf{V} : \mathbb{R}^r \to \mathbb{R}^n_{\mathbf{M}}$. Let us justify the results. Since

$$(\mathbf{F}^\star m_1, m_2)_{\boldsymbol{M}} = (m_1, \mathbf{F} m_2), \qquad \forall m_1 \in \mathbb{R}^q, \forall m_2 \in \mathbb{R}^n_{\boldsymbol{M}}$$

then

$$(\mathbf{F}^\star m_1)^T \boldsymbol{M} m_2 = m_1^T \mathbf{F} m_2$$

Finally, we obtain the expressions

$$\mathbf{F}^\star = \mathbf{M}^{-1}\mathbf{F}^T \tag{2.65}$$

and

$$\mathbf{V}^\diamond = \mathbf{V}^T\mathbf{M} \tag{2.66}$$

Now, we analyze the matrix representation $\mathbf{B} : \mathbb{R}^n_{\mathbf{M}} \to \mathbb{R}^n_{\mathbf{M}}$ of an operator $\mathcal{B} : L^2(\Omega) \to L^2(\Omega)$. First, note that the nodal vector corresponding to $\phi_i \in V_h$

is $\boldsymbol{e}_i$. From equation (2.61), we can deduce that

$$\int_\Omega \phi_i \mathcal{B}\phi_j dx = (\phi_i, \mathcal{B}\phi_j)_{L^2} = (\boldsymbol{e}_i, \boldsymbol{B}\boldsymbol{e}_j)_{\boldsymbol{M}} = \boldsymbol{e}_i^T \boldsymbol{M}\boldsymbol{B}\boldsymbol{e}_j \tag{2.67}$$

so the matrix representation of the operator $\mathcal{B}$ can be write explicitly as $\boldsymbol{B} = \boldsymbol{M}^{-1}\boldsymbol{N}$, with

$$\boldsymbol{N}_{ij} = \int_\Omega \phi_i \mathcal{B}\phi_j dx, \qquad i,j \in \{1,\dots,n\} \tag{2.68}$$

With all these elements, we can derive now the finite-dimensional representation of the prior. We start by the matrix representation of the operator $\mathcal{A}$ defined in equation (2.10). From the weak form of this operator, its matrix representation is given by

$$\boldsymbol{K}_{ij} = \int_\Omega \gamma \nabla\phi_i \cdot \nabla\phi_j + \delta\phi_i\phi_j dx, \qquad i,j \in \{1,\dots,n\} \tag{2.69}$$

Note that this matrix representation can be modified to include the effects of Robin boundary conditions as explained in [54] and [3]. We consider $\boldsymbol{A} = \boldsymbol{M}^{-1}\boldsymbol{K}$. Note that $\boldsymbol{A}^* = \boldsymbol{A}$, that is $\boldsymbol{A}$ is self adjoint ($\boldsymbol{A}^{-1}$ too). Now, the finite-dimensional Gaussian prior measure is specified by the density

$$\pi_{prior}(\boldsymbol{m}) \propto \exp\left(-\frac{1}{2}||\boldsymbol{A}(\boldsymbol{m}-\boldsymbol{m}_0)||^2_{\boldsymbol{M}}\right) \tag{2.70}$$

Finally, the finite-dimensional posterior measure is specified by the density

$$\pi_{post}(\boldsymbol{m}) \propto \exp\left(-\frac{1}{2}||f(m_h)-y||^2_{\Gamma^{-1}_{noise}} - \frac{1}{2}||\boldsymbol{A}(\boldsymbol{m}-\boldsymbol{m}_0)||^2_{\boldsymbol{M}}\right) \tag{2.71}$$

2.4 Model Selection

Model selection is the task of using data to pick one model from a list of candidate models $\mathcal{M}_1, \mathcal{M}_2, \ldots, \mathcal{M}_p$. In Bayesian statistics, Bayes Factors [81] can be used as a measure of the evidence for model $\mathcal{M}_i$ over model $\mathcal{M}_j$. In Bayesian inverse problems, candidate models might be viewed as alternative hypotheses corresponding to (i) different representations of the parameter or (ii) different forward models to fit the data (see, e.g., [36, 38] and the references therein). In the following sections, we present the formulas to compute the normalization constants for two cases. In the first case, we consider a Gaussian linear problem. In the second case, we consider a linearized model.

2.4.1 The normalization constants: the Gaussian case

Consider the case where the data are fit by a linear model denote by X and we want to recover the parameter of interest β. Since we want to compare models, we include an index in the notation and consider

$$y = X_i\beta_i + \varepsilon. \tag{2.72}$$

We want to determine for which i, $X_i\beta_i$ is the best model for the data y. Let I the r.v. model indicator. I take values $1, 2, \ldots, m$.
The joint distribution for β and i can be expressed as

$$f_{\beta_i,I}(b, i) = f_{\beta_i|I}(b|i)f_I(i) \tag{2.73}$$

where the support of f_I is $\{1, 2, \ldots, n\}$. We propose $f_{\beta_i|I}$ as a normal distribution, that is

$$f_{\beta_i|I} \sim \mathcal{N}\left(\mu_0^i, \sigma^2(A_0^i)^{-1}\right) \tag{2.74}$$

The posterior distribution for the problem is

$$f_{\beta_i,I|Y}(b_i, i|y) = \frac{f_{Y|\beta_i,I}(y|b_i, i)f_{\beta_i,I}(b_i, i)}{f_Y(y)} \tag{2.75}$$

Using (2.73), we have

$$f_{\beta_i,I|Y}(b_i,i|y) = \frac{f_{Y|\beta_i,I}(y|b_i,i)f_{\beta_i|I}(b|i)f_I(i)}{f_Y(y)} \tag{2.76}$$

where

$$f_{\beta_i,I|Y}(b_i,i|y) \sim \mathcal{N}\left((X_i^TX_i + A_0^i)^{-1}(A_0^i\mu_0^i + X_i^Ty), \sigma^2(X_i^TX_i + A_0^i)^{-1}\right)$$

On the other hand,

$$\begin{aligned} f_{I|Y} &= \int f_{\beta_i,I|Y}(b_i,i|y)db_i \\ &= \int \frac{f_{Y|\beta_i,I}(y|b_i,i)f_{\beta_i,I}(b_i,i)}{f_Y(y)}db_i \\ &= \frac{f_I(i)}{f_Y(y)}\int f_{Y|\beta_i,I}(y|b_i,i)f_{\beta_i|I}(b_i|i)db_i \end{aligned}$$

Once the model is fixed, we obtain

$$f_{\beta_i|Y,I}(b_i|y,i) = \frac{f_{Y|\beta_i,I}(y|b_i,i)f_{\beta_i|I}(b_i|i)}{\int f_{Y|\beta_i,I}(y|b_i,i)f_{\beta_i|I}(b_i|i)db_i} \tag{2.77}$$

where $\int f_{Y|\beta_i,I}(y|b_i,i)f_{\beta_i|I}(b_i|i)db_i$ is the normalization constant for the model i, that is

$$f_{Y|I}(y,i) = \int f_{Y|\beta_i,I}(y|b_i,i)f_{\beta_i|I}(b_i|i)db_i$$

Finally, from (2.77), we obtain that

$$f_{Y|I}(y|i) = \frac{f_{Y|\beta_i,I}(y|b_i,i)f_{\beta_i,I}(b_i|i)}{f_{\beta_i|Y,I}(b_i|y,i)} \tag{2.78}$$

Now, recall that we assume that $f_{\beta_i,I}(b_i|i) \sim \mathcal{N}(\mu_0^i, \sigma^2(A_0^i)^{-1})$. In our case, b_i are the coefficients of a sine series and i is the number of terms in such series,

so we assume $\mu_0^i = 0$ for all i and

$$\sigma^2 (A_0^i)^{-1} = \begin{pmatrix} \frac{1}{1^2} & 0 & \cdots & 0 \\ 0 & \frac{1}{2^2} & \cdots & 0 \\ \vdots & & & \vdots \\ 0 & \cdots & 0 & \frac{1}{i^2} \end{pmatrix} \tag{2.79}$$

that is

$$A_0^i = \begin{pmatrix} \sigma^2 & 0 & \cdots & 0 \\ 0 & (2\sigma)^2 & \cdots & 0 \\ \vdots & & & \vdots \\ 0 & \cdots & 0 & (i\sigma)^2 \end{pmatrix} \tag{2.80}$$

We conclude that

$$f_{\beta_i|I}(b_i|i) = \frac{\exp\left(-\frac{1}{2\sigma^2} b_i^T A_0^i b_i\right)}{\sqrt{(2\pi\sigma^2)^i |(A_0^i)^{-1}|}} \tag{2.81}$$

Also, from the observation model, we have that

$$f_{Y|\beta_i,I}(y|b_i,i) = \frac{\exp\left(-\frac{1}{2\sigma^2}(y - X_i b_i)^T (y - X_i b_i)\right)}{\sqrt{(2\pi\sigma^2)^n}} \tag{2.82}$$

where n is the dimension of y.
Finally, we have

$$f_{Y|I}(y|i) = \frac{\exp\left(-\frac{1}{2\sigma^2}(Q_1 + Q_2 - Q_3)\right) |A_0^i|^{1/2}}{\sqrt{(2\pi\sigma^2)^n} |A_n^i|^{1/2}} \tag{2.83}$$

where

$$Q_1 + Q_2 - Q_3 = y^T \left(I - X_i \left(X_i^T X_i + A_0^i\right)^{-1} X_i^T\right) y$$

To avoid numerical issues, we will consider $\log f_{Y|I}(y|i)$. We want to compute

$$\log f_{Y|I}(y|i) = \log \frac{\exp\left(-\frac{1}{2\sigma^2}(Q_1 + Q_2 - Q_3)\right)|A_0^i|^{1/2}}{\sqrt{(2\pi\sigma^2)^n}|A_n^i|^{1/2}}$$

$$= \left(-\frac{1}{2\sigma^2}(Q_1 + Q_2 - Q_3)\right) + \frac{1}{2}\log\frac{|A_0^i|}{|A_n^i|} - \frac{n}{2}\log(2\pi\sigma^2)$$

$$= C - \frac{1}{2\sigma^2}Q + \frac{1}{2}\log\frac{|A_0^i|}{|A_n^i|}$$

where C does not depend on i and $Q = -y^T X_i \left(X_i^T X_i + A_0^i\right)^{-1} X_i^T y$.
Now, if $i = 1, 2, \cdots, M$, then

$$f_{I|Y}(i_0|y) = \frac{f_{Y|I}(y|i_0)f_I(i_0)}{\sum_{j=1}^{M} f_{Y|I}(y|j)f_I(j)}$$

Note that

$$\frac{f_{I|Y}(i_0|y)}{f_{I|Y}(j_0|y)} = \frac{f_{Y|I}(y|i_0)f_I(i_0)}{f_{Y|I}(y|j_0)f_I(j_0)} \tag{2.84}$$

In our case, for an uniform distribution for I, then the Bayes factor decides for the higher normalization constant.

2.4.2 The normalization constants: the linearized case

Computing the Bayes factor is a challenging problem that has received considerable attention [81, 82, 83]. To approximate the Bayes factors in this work we shall assume both models have the same probability *a priori*, i.e. $\pi_I(\mathcal{M}_1) = \pi_I(\mathcal{M}_2)$, and use the Laplace approximation of the posterior to obtain a Gaussian distribution. Recall the linearization of the forward map $f(\mu)$ around the MAP estimate is used to approximate the data by

$$y = f(\mu_{MAP}) + F(\mu - \mu_{MAP}) + \eta \tag{2.85}$$

where $F = \dfrac{\partial f}{\partial \mu}(\mu_{MAP})$. Let $\mathcal{M}_i$ be the model defined by a parameter mesh indexed by i. For a fixed mesh it corresponds a discretization of the inverse problem, i.e., a prior distribution $\mathcal{N}(\mu_0^i, \Gamma_{prior}^i)$.

Numerical details: Now, we can focus on the computation of $\pi_{Y|i}(y)$. In the following, we avoid the i superindex. Consider the quantity

$$\log \pi_{Y|i}(y) = -\frac{1}{2}Q + \frac{1}{2}\log \frac{|\Gamma_{post}|}{|\Gamma_{prior}|} \tag{2.86}$$

where

$$Q = \tilde{y}^T \Gamma_{obs}^{-1} \tilde{y} + \mu_{prior}^T \Gamma_{prior}^{-1} \mu_{prior} - \mu_{MAP}^T \left(F^T \Gamma_{obs}^{-1} F + \Gamma_{prior}^{-1} \right) \mu_{MAP}$$

and $\tilde{y}$ is

$$\tilde{y} = y - f(\mu_{MAP}) + F\mu_{MAP} \tag{2.87}$$

Simplifying the last expression, it can be noticed that

$$\begin{aligned} Q = &\left(y - f(\mu_{MAP})\right)^T \Gamma_{obs}^{-1} \left(y - f(\mu_{MAP})\right) + 2\left(y - f(\mu_{MAP})\right)^T \Gamma_{obs}^{-1} F\mu_{MAP} \\ &+ \mu_{prior}^T \Gamma_{prior}^{-1} \mu_{prior} - \mu_{MAP}^T \Gamma_{prior}^{-1} \mu_{MAP} \end{aligned} \tag{2.88}$$

These computations allow us to approximate the normalization constant of each model. To determine each normalization constant, we need to compute four quantities of which three are straightforward:

1. **Misfit** at μ_{MAP}:

$$\left(y - f(\mu_{MAP})\right)^T \Gamma_{obs}^{-1} \left(y - f(\mu_{MAP})\right)$$

2. **Prior evaluations**:

$$\mu_{prior}^T \Gamma_{prior}^{-1} \mu_{prior} - \mu_{MAP}^T \Gamma_{prior}^{-1} \mu_{MAP}$$

3. **Sensitivity** at μ_{MAP}:

$$2\left(y - f(\mu_{MAP})\right)^T \Gamma_{obs}^{-1} F \mu_{MAP}$$

4. **Log quotient covariance determinant**: To approximate the quantity $\frac{1}{2}\log\frac{|\Gamma_{post}|}{|\Gamma_{prior}|}$, we use the low rank approximation of the posterior covariance. Note that, since $\Gamma_{post} \approx \Gamma_{prior} - V_r D_r V_r^T$ then

$$\frac{|\Gamma_{post}|}{|\Gamma_{prior}|} = |\Gamma_{post}\Gamma_{prior}^{-1}| \approx |I - V_r D_r V_r^T \Gamma_{prior}^{-1}| \tag{2.89}$$

and applying Sylvester formula, we obtain that

$$|I - V_r D_r V_r^T \Gamma_{\text{pr}}^{-1}| = |I - V_r^T \Gamma_{prior}^{-1} V_r D_r| = |I - D_r| \tag{2.90}$$

since $V^T \Gamma_{prior}^{-1} V = I$.

Remarks:

- Sylvester formula allows to change the dimension of the problem and compute the quotient between covariance matrices using just r eigenvalues.
- To compute each normalization constant, we use the low rank approximation of the posterior covariance. To compare two models, this rank need to be specified. That is, all models have the same numerical rank r_0. We choose the rank as the number for the first eigenvalue less than 1 in the coarse mesh.
- To evaluate the sensitivity can be unstable because of the data term and the backtracking stopping of the optimization step. To avoid this, we use the fact that the gradient is zero in the stationary point.
- We compute the Bayes' factor between two consecutive models and stop the refinement when this quotient is close or lower than 1 or when the

resolution is very high (we can not differentiate between one mesh and other).

2.4.3 More on model selection criteria

Well known criteria as Akaike Information Criteria (AIC) and Bayesian Information Criteria (BIC) are used as approximation of quantities to perform model selection. AIC is based on a approximation of Akaike for the KL information given by

$$AIC = -2\ln\mathcal{L} + 2d \tag{2.91}$$

where $\mathcal{L}$ is the maximum of the likelihood function and d is the number of model parameters. Very similar to AIC is BIC, which is based on an approximation of the evidence, and is given by

$$BIC = -2\ln\mathcal{L} + 2d\ln N \tag{2.92}$$

with N the number of data points. Note that for the case of BIC, the extra number of degrees of freedom in the model is penalized by $\ln N$, which for sparse observations may choose for models as AIC does.
The KL-divergence between two Gaussians has closed form [84, 85]:

$$\mathrm{KL}(\mathcal{N}(\mu_1,\Sigma_1)||\mathcal{N}(\mu_2,\Sigma_2)) =$$

$$\frac{1}{2}\left(\mathrm{tr}\left(\Sigma_1^{-1}\Sigma_2 - I\right) + (\mu_1-\mu_2)^T\Sigma_1^{-1}(\mu_1-\mu_2) - \log\det\left(\Sigma_2\Sigma_1^{-1}\right)\right) \tag{2.93}$$

For our porpuses, we would like to compute the KL divergence between the gaussian prior and the gaussian posterior

$$\mathrm{KL}(\mathcal{N}(\mu_{pr},\Sigma_{pr})||\mathcal{N}(\mu_{post},\Sigma_{post}))$$

To compute this quantity, we will use the low rank approximation of the posterior covariance. From previous computations in equation (2.90), we know that

$$\log\det\left(\Sigma_{post}\Sigma_{pr}^{-1}\right) = -\sum\log(\lambda_i+1) \tag{2.94}$$

and using the cyclic property of the trace, we have

$$\mathrm{tr}\left(\Sigma_{pr}^{-1}\Sigma_{post} - I\right) = -\mathrm{tr}\left(\Sigma_{pr}^{-1}V_r D_r V_r^T\right) = -\mathrm{tr}\left(V_r D_r V_r^T \Sigma_{pr}^{-1}\right) = -\mathrm{tr}\left(D_r\right) \tag{2.95}$$

with $D_r = \mathrm{diag}\left(\dfrac{\lambda_i}{\lambda_i + 1}\right)$

2.5 Multimesh Approach

In this section, we describe the multimesh approach for inverse problems. This approach may be implemented for the cases with high dimensional data as the MRE problem, see [86]. We assume that the pde system is solved by the Finite Element Method. It is important to note that this discretization of the forward problem must be considered at the time of properly discretize the inverse problem, see [18], [19]. Recall the optimization problem in function spaces was formulated in equation (2.33)

$$\mathcal{L}(u,p,m) = \frac{1}{2}\int_{\mathcal{X}} (y-u)^T \Gamma_{obs}^{-1} (y-u)\, dx + \frac{1}{2}||\mathcal{A}(m-m_0)||_{L^2}^2 + a(u,m,p) - L(p) \tag{2.96}$$

Once we discretize this problem, we know that the data $y \in \mathbb{R}^n$ and our discretization defines the dimension for u, p and m. The traditional approach assumes that $u, m \in \mathbb{R}^p$ and needs to introduce an observation operator $\mathcal{F} : \mathbb{R}^p \to \mathbb{R}^n$ to compute the misfit. The misfit term becomes

$$\frac{1}{2\sigma^2}||y - \mathcal{F}(u_h)||_{\mathbf{M}}^2 \tag{2.97}$$

where u_h is the discretization of u and $\mathbf{M}$ is the finite element mass matrix as in [18]. The idea of the multimesh is to avoid the previously mentioned observation operator. Let us consider two discretization levels with $u_h \in \mathcal{E}_{h_1}$ and $m_h \in \mathcal{E}_{h_2}$. Also, we assume that the discretized state space $\mathcal{E}_{h_1}$ corresponds to a fine mesh. To generate u_h, we need to solve the forward problem. Recall that the forward problem is obtained from the computation of the first variation of $\mathcal{L}$ with respect to p. So, the week form of the pde is given by

$$\delta_p \mathcal{L}(u,m,p)(\tilde{p}) = a(u,m,\tilde{p}) - L(\tilde{p}) = 0 \tag{2.98}$$

To solve this pde, we need that $u, m, \tilde{p}$ belong to the same discretized space. Since we are proposing that $m_h \in \mathcal{E}_{h_2}$, we need to introduce an interpolation operator $\mathcal{I}^p : \mathcal{E}_{h_2} \to \mathcal{E}_{h_1}$ and finally solve

$$a(u_h, \mathcal{I}^p(m_h), p_h) - L(p_h) = 0 \tag{2.99}$$

to obtain u_h. To implement this notion in an hIPPYlib script, we describe in the following lines the changes on the code:

```
def solveFwd(self, state, x, tol):

    if self.solver is None:
        self.solver = self._createLUSolver()

    u = dl.TrialFunction(self.Vh[STATE])
    m = vector2Function(x[PARAMETER], self.Vh[PARAMETER])
    p_hat = dl.TestFunction(self.Vh[ADJOINT])

    m.set_allow_extrapolation(True)
    m_interp = dl.interpolate(m, self.Vh_interp[PARAMETER])

    res_form = self.varf_handler_state(u, m_interp, p_hat)
    A_form = dl.lhs(res_form)
    b_form = dl.rhs(res_form)

    A, b = dl.assemble_system(A_form, b_form)
    self.solver.set_operator(A)
    self.solver.solve(state, b)
```

Analogously, we consider the adjoint problem. The equation for the adjoint problem is given by

$$\delta_u \mathcal{L}(u, m, p)(\tilde{u}) = \int_{\mathcal{X}} \tilde{u}^T \Gamma_{obs}^{-1} (y - u)\, dx + \delta_u a(u, m, p)(\tilde{u}) = 0 \tag{2.100}$$

Finally we solve

$$\frac{1}{\sigma^2} \langle \tilde{u}, y - u_h \rangle_{\mathbf{M}} + \tilde{a}(u_h, \mathcal{I}^p(m_h), p_h)(\tilde{u}) = 0 \tag{2.101}$$

where $\tilde{a}$ corresponds to $\delta_u a$ and u_h is the solution of the forward problem given in equation (2.99). Note that the final form for $\tilde{a}$ depends on the original pde.

Following the pde constrained optimization approach, we need to adapt the

quantities in the evaluation of the gradient and hessian actions to perform the optimization in the parameter space. In this case, we need an interpolation operator $\mathcal{I}^s$ to change the resolution of the solutions of the forward and adjoint problems u_h and p_h. In this case, the week form for the gradient is obtained by

$$\delta_m \mathcal{L}(u, m, p)(\tilde{m}) = \int_\Omega \tilde{m} \mathcal{A}^2 (m - m_0) dx + \delta_m a(u, m, p)(\tilde{m}) \tag{2.102}$$

The expression that we compute is given by

$$\mathcal{G} = \tilde{m} \mathbf{A}^2 (m_h - m_0) dx + \bar{a}(\mathcal{I}^s(u_h), m_h, \mathcal{I}^s(p_h))(\tilde{m}) \tag{2.103}$$

where $\mathbf{A}^2$ correspond to the discretized action of $\mathcal{A}^2$ inside the inner product and $\bar{a}$ corresponds to $\delta_m a$. In an analogous way, the quantities for the linearized forward, linearized adjoint, and the Hessian are determined. These interpolations between meshes produces that the Hessian is not symmetric any more. We will show in examples the weak form for the optimization and use an inexact Newton GMRES in hIPPYlib, see the Appendix A for a GMRES reminder. We use GMRES implementation in scipy library for python [87].

2.6 Algebraic Inversion for Magnetic Resonance Elastography

Magnetic Resonance Elastography (MRE) is a diagnostic technique for the detection and characterization of a wide range of disease processes. MRE may be incorporated into a standard MRI examination to provide a rapid, reliable and comprehensive imaging assessment at a single patient appointment, [86]. This technique can visualize and quantitatively measure propogating acoustic strain waves in tissue-like materials subjected to harmonic mechanical excitation. Shear waves at frequencies in the 10-1000 Hz range are used as a probe because they are much less attenuated than at higher frequencies and because shear modulus varies widely in bodily tissues, [88, 89, 90]. MRE allows to infer mechanical properties of many tissues including liver, muscle, brain, lung, spleen, pancreas, kidneys among others [56, 91]. Most soft tissues have mechanical properties that are intermediate between those of fluids and solids. Authors in [92] introduced a Complex-Valued Stiffness Reconstruction for MRE by Algebraic Inversion of Differential Esquations (AIDE) in which they find the shear modulus locally by estimating the local spatial derivatives of the displacement. Since the derivatives of the displacement must be estimated from the noisy displacement data, authors propose to estimate derivatives using a least-square fitting procedure made popular by Savitsky and Golay, see [93]. Specifically, the data are fit to a separable polynomial using information from a certain number of neighbors in a set named window. For a fixed window, derivatives of the best-fit polynomial are used as estimates of the data derivatives. Other approaches to approximate the derivatives proposed wavelets transforms, see [94].

To apply a Savistky Golay filter in 2D, we need three steps: to fit a polynomial around a point to smooth just the value of this point, To choose a window that contains other points data (the order of the polynomial define the minimum window size) and To apply a least squares estimation to fit the polynomial values. The variance of the estimation decreases if the window size increases, nevertheless, the bias of the estimate increases too, see [95].

This local estimate corresponds to assume that the shear modulus is constant

by element. According to [96], this assumption limits the local variability of the parameters in the estimate. Futhermore, whenever the true parameters do vary significantly, the estimate is invalid. From a clinician's point-of-view, regions where the true stiffness changes rapidly are perhaps the most important, for they indicate the boundaries of any patology. According to [97], it should be noted that filters, like those for suppressing noise, change the effective wavelengths in the image. Thus a careful match of filter threshold may be able to compensate for dispersive effects.

The governing equation for solids under time-harmonic motion [98], together with the boundary conditions is given by

$$\begin{aligned} \nabla \cdot \sigma = &\quad -\omega^2 \rho u, \quad \text{in } \Omega \\ u = &\quad 0, \quad \text{on } \Gamma_D \\ \mathbf{n} \cdot \sigma = &\quad f_0, \quad \text{on } \Gamma_N \\ \mathbf{n} \cdot \sigma = &\quad 0, \quad \text{on } \Gamma_0 \end{aligned} \tag{2.104}$$

where ω denotes the actuation frequency, ρ is the density of the solid; u is the complex-valued time-harmonic displacement field, σ is the Cauchy stress tensor defined over the body Ω and $\mathbf{n}$ the unit outward surface normal. In this work, we mimic an abdomen slice as our domain Ω. Γ_D is the region of the domain corresponding to the lumbar region. We assume no displacement in this area so we impose homogeneous Dirichlet conditions on Γ_D. f_0 is the traction condition corresponding to the passive actuator acting on an abdomen area denoted by Γ_N and finally, Γ_0 is the complement of $\Gamma_D \bigcup \Gamma_N$. For linear elastic isotropic materials, the Cauchy stress tensor can be expressed as

$$\sigma = \lambda \text{tr}(\varepsilon) I + 2\mu\varepsilon \tag{2.105}$$

with

$$\varepsilon = \frac{1}{2}\left(\nabla u + \nabla u^T\right) \tag{2.106}$$

where ε represents an infinitesimal strain tensor; λ and μ are the Lamé's material parameters (μ is the shear modulus), which are the material parameters to be reconstructed in the elastography problem.

To generate data, we use a 2nd order Continuous Galerkin scheme in FEniCS, [99]. Continuous Galerkin (CG) methods may have a bad performance for cases where materials are highly incompressible. In these cases, CG provides a smaller displacement solution, called **volume locking**. Mixed formulations and Discontinuous Galerkin (DG) methods are possible solution for counteract the locking phenomenon, among others [100, 101, 102, 103]. According to [100], the p-version of the finite element does not suffer of this phenomenon and optimal rate error estimates may be show independent of the Poisson ratio. From our simulations, a 2nd order CG is enough to generate data for the examples we'll show.

The estimation of a local value for the stiffness is as follows: 2D displacement values are generated with the model in equation (2.104), a Savistky Golay filter is applied to eliminate high frequency effects, second derivatives of the displacement are estimated using the same filter, on each element we compute an estimate of μ by a least-squares approach using the equations

$$-\Delta u_i^a \mu = \rho\omega^2 u_i^a, \qquad i = 1, 2, 3, \qquad a = x, y \tag{2.107}$$

where u_i^x is the x displacement obtained from the filter application on the i-th node of the element. In the simplest under homogeneity and incompressibility assumptions, it can be seen that poorly-interrogated regions correspondend to regions where $\Delta u \approx 0$ or $u \approx 0$ (see equation (2.107)).

According to [101], the simplifying assumptions are local homogeneity and incompressibility. Since the divergence of the displacement for nearly incompressible material is almost zero, this assumption simplify the expression in equation (2.105) by

$$\mathrm{tr}(\varepsilon) = \nabla \cdot u \approx 0. \tag{2.108}$$

After this, local homogeneity and some computations allow us to arrive to equation (2.107).

Figure (2.3) shows the parameter to recover and the AIDE estimate for frequency 20 Hz. Frequency wave effects and artifacts can be nottice in the recovered estimate. According to [104], finite tissue boundaries and waveguide effects give rise to wave interferences which are not accounted for the standard

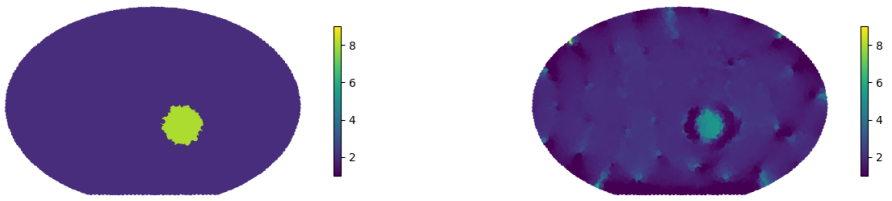

(a) (b)

Figure 2.3: Algebraic Inversion: (a) True parameter. (b) Parameter recovered at freq 20 Hz.

elasticity reconstruction methods. Also, a multifrequency inversion produces fewer artifacts in the viscoelastic parameter map than standard single-frequency parameter recover. According to [105], acquisitions at different frequencies can be used to circumvent the conditioning and uniqueness concerns in the inversion process.

(a) (b)

Figure 2.4: Algebraic Inversion: (a) Parameter recovered at freq 20 Hz. (b) Parameter recovered at multiple frequencies: $15, 18, 20, 22$ and 25 Hz

Figure (2.4) shows the parameter to recover and the AIDE estimate using data at frequencies $15, 18, 20, 22$ and 25 Hz. Figure (2.5) shows relative errors with respect the parameter to recover of estimates in figures (2.3) and (2.4).

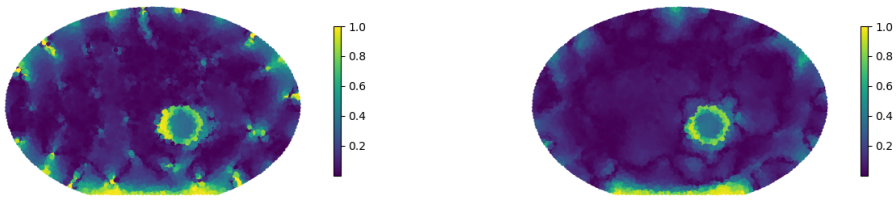

(a) (b)

Figure 2.5: Relative Error at Algebraic Inversion: (a) Parameter recovered at freq 20 Hz. (b) Parameter recovered at multiple frequencies: $15, 18, 20, 22$ and 25 Hz

2.7 Optimization algorithms from a contact geometry perspective

Consider the problem of

$$\min f(x) \tag{2.109}$$

where f is a convex function with $x \in \mathbb{R}^n$. In the differentible case, Newton method may have a high computational cost in problems with increased size. That is why first order methods had become very popular in the machine learning community. The phenomenon named as acceleration has been topic of theoretical and computational research. Among the best known methods, we can find Nesterov accelerated gradient method. Recently in [106], authors derived a second-order ODE which is the exact limit of Nesterov's scheme. Relating optimization to ordinary differential equations is not new, see [107], [108], [109]. The idea behind is to consider small step sizes such that the solution of the optimization converges to a curve from the ODE solution. In the opposite direction we can obtain several discretizations from the same second-order ODE. Of course, the aim is to find a discretization that preserves theoretical properties as the convergence rates. The analysis of the ODE can provide insights for the optimization, see [110], [111]. In this section, we describe the main elements of

this approach to explain latter the results in [112].

2.7.1 Bregman Hamiltonian and contact systems

Authors in [113] introduced the Bregman Lagrangian as

$$\mathcal{L}(X, V, t) = e^{\alpha_t + \gamma_t} \left(D_h \left(X + e^{-\alpha_t} V, X \right) - e^{\beta_t} f(X) \right) \tag{2.110}$$

for α, γ and β continuous and differentiable functions. h is a distance-generating function that satisfies convexity and smoothness. They defined ideal scaling conditions by

$$\dot{\beta}_t \leq e^{\alpha_t} \tag{2.111}$$

$$\dot{\gamma}_t = e^{\alpha_t} \tag{2.112}$$

For the case of $h(X) = \frac{1}{2} \|X\|^2$, the resulting Euler-Lagrange equations are

$$\ddot{X} + (e^{\alpha} - \dot{\alpha}) \dot{X} + e^{2\alpha + \beta} \nabla f(X) = 0. \tag{2.113}$$

Also, they introduced specific functions for α, γ and β that satisfy a convergence rate of $\mathcal{O}(1/t^p)$, that is

$$f(X) - f(X^*) \leq \mathcal{O}(1/t^p) \tag{2.114}$$

with X^* the unique minimizer. The discretization of the equation does not always preserve this continuous convergence rate. Finally they mentioned that another option to explore the Bregman Lagrangian is to study its Hamiltonian. This approach was considered in [114]. The Bregman Hamiltonian is the result of apply the Legendre transform to the Bregman Lagrangian. In this case, the second-order Euler-Lagrange equation is transformed into a pair of first-order equations. Authors in [114] advocate for symplectic integrators to obtain reliable and rate-matching discretizations. In this case, the Bregman

Hamiltonian becomes

$$H(X,P,t) = \frac{1}{2}e^{\alpha_t - \gamma_t}\left\|P\right\|^2 + e^{\alpha_t+\beta_t+\gamma_t}f(X). \tag{2.115}$$

In the next subsection, we introduce some basic notions for the contact geometry. A more general expression can be deduced under this approach. Bregman Hamiltonians as in equation (2.115) are specific cases under the contact formulation, see [112].

Authors in [112] propose a geometric approach to optimization using contact geometry. In the Euclidean context a contact state space is odd–dimensional, $\mathbb{R}^{2n+1}$, and coordinated by the variables (X,P,S), where the $X \in \mathbb{R}^n$ play the role of *generalized coordinates*, the $P \in \mathbb{R}^n$ the corresponding *momenta* and $S \in \mathbb{R}$ the *action* of the system. In this subsection, we recall a result around the dynamical system that allows to connect with the problem in equation 2.109.

***Lemma* 2.7.1 (Contact Hamiltonian systems)** *Given a (possibly time–dependent) differentiable function $\mathcal{H}(X,P,S,t)$ on the contact state space $(\mathbb{R}^{2n+1}, \eta_{\text{std1}})$, the associated contact Hamiltonian system is the following dynamical system*

$$\dot{X} = \nabla_P \mathcal{H} \tag{2.116}$$

$$\dot{P} = -\nabla_X \mathcal{H} - P\frac{\partial \mathcal{H}}{\partial S} \tag{2.117}$$

$$\dot{S} = \nabla_P \mathcal{H}\, P - \mathcal{H}\,. \tag{2.118}$$

To solve numerically this system, a geometric integrator is proposed based on results in [115].

2.7.2 Splitting methods for ODEs

In order to solve the system (2.116)-(2.118) we appeal to splitting methods. According to [116], a splitting method is a class of time integration of ODEs and PDEs. For the differential equation

$$\dot{x} = X(x) \tag{2.119}$$

an splitting method involves

- choosing a set of vector fields X_i such that $X = \sum X_i$
- integrating either exactly or approximately each X_i
- combining these solutions to yield an integrator for X.

It is assume that the pieces X_i are simpler to treat than X, that is:

1. X_i is of a simpler type than X
2. X_i is of the same type than X but easier to treat numerically.

The main objective of construct a geometric integrator is to preserve structural features of the flow of X as symplecticity, volume preservation, integrals and/or symmetries. We have

***Proposition* 2.7.1** *If a vector field $X(x)$ can be split as a sum*

$$X(x) = \sum_{i=1}^{i=n} X_i(x) \tag{2.120}$$

where each vector field X_i is exactly integrable, then

$$S_2(\tau) = e^{\frac{\tau}{2}X_1} e^{\frac{\tau}{2}X_2} \cdots e^{\tau X_n} \cdots e^{\frac{\tau}{2}X_2} e^{\frac{\tau}{2}X_1} \tag{2.121}$$

is a second order integrator for the differential equation (2.119).

Chapter 3

Results

In this chapter, we solve several problems based on the results of the previous section. As we mentioned before, a statistical approach for inverse problems introduce new components to propose solutions with quantified uncertainty and produce predictions. Implementation of computational models on the treatment of data uncertainties demands regularity on the forward modeling, consistency on the discretization and stability on the numerical posterior distribution which allows to encode the uncertainty of the solutions. In this section we will present examples on (1) The computation of the normalization constants for linear inverse problems for two problem types. The first problem considers the number of terms in a Fourier series. The second considers the low-rank approximation of the posterior on the big scale setting. Formulas for linearized models are proposed and apply to a nonlinear inverse problem governed by an elliptic pde. The final aim of these computations is under a model selection approach. In this case, a local refinement is performed and the computation of the normalization constants allows us to determine the best mesh. Also, we can compare several refinement criteria again by the computation of these normalization constants. (2) The comparison of two members of different families of transition kernels to perform the posterior distribution exploration in an inference problem in 1D. HAMCMC is a Quasi-Newton method where proposals come from a continuous dynamic. T-walk is a sampler with the affine invariance property and free-derivate information. With an example that recovers four parameters, t-walk outperform HAMCMC. (3) The incorporation of elements of optimal

experimental design in Multifrequency Algebraic Inversion with application to Magnetic Resonance Elastography. The aim is to decrease the uncertainty of the estimates in the AIDE inversion. This approach allows decreasing the variance out of the inclusion area. (4) A Bayesian approach to analyze Oral Glucose Tolerance Test data. The forward modeling considers Erlang distributions to reproduce the delays in the body reaction to a sugary drink. From estimates of two parameters related to digestive absorption and insulin production, we classify around 85 % of 80 patients. (5) The inference for an ODE model that describes the early dynamics of the covid-19 in México. This approach considers possible infections through the environment and the estimation of its transmission rate. (6) The discretization of an accelerated scheme that preserves theoretical convergence rates with possible applications in optimization and machine learning. The main goal illustrated by these examples is the systematic treatment of model, data, and computational errors to produce predictions with quantied uncertainty.

3.1 Inference on the Initial Condition of the Wave Equation

In this section, we use Bayesian model selection to determine the number of coefficients in the representation of a function as a Fourier series. Specifically, we apply formulas explained in subsection 2.4.1 to compute Bayes factors. We show this technique in the linear inverse problem of recovering the initial condition of the wave equation. We present three cases to exemplify our results.

3.1.1 Forward map and Observation Model

Consider the homogeneous Dirichlet conditions for the wave equation:

$$\begin{aligned} u_{tt} &= u_{xx}, \qquad x \in (0,1) \\ u(0,t) &= 0 = u(1,t) \end{aligned} \tag{3.1}$$

with initial conditions

$$u(x,0) = \phi(x) \qquad u_t(x,0) = \psi(x) \tag{3.2}$$

Under a separation of variables technique, a solution of the problem (3.1)-(3.2) can be found substitying $u(x,t) = X(x)T(t)$ in the PDE. This problem becomes a pair of separate ordinary differential equations for $X(x)$ and $T(t)$ given by

$$X'' + \beta^2 X = 0 \qquad \text{and} \qquad T'' + \beta^2 T = 0 \tag{3.3}$$

Finally, using Dirichlet and initial conditions, we obtain

$$u(x,t) = \sum_n \left(A_n \cos(n\pi t) + B_n \sin(n\pi t)\right) \sin(n\pi x) \tag{3.4}$$

Note that

$$\begin{gathered} \phi(x) = \textstyle\sum_n A_n \sin(n\pi x) \\ \psi(x) = \textstyle\sum_n n\pi B_n \sin(n\pi x) \end{gathered} \tag{3.5}$$

Now, assume that $\psi(x) = 0$, then $B_n = 0$ for all n. Then we have

$$u(x,t) = \sum_n A_n \cos(n\pi t) \sin(n\pi x) \tag{3.6}$$

where

$$A_n = 2\int_0^1 \phi(x) \sin(n\pi x) dx \tag{3.7}$$

Now, suppose that we can obtain measurements at $t = 1$. Then from equation (3.6) we have that

$$\mathcal{G}(\phi) = u(x,1) = \sum_{n=0}^{\infty} A_n (-1)^n \sin(n\pi x) \tag{3.8}$$

Suppose that $\phi_1 = \sum_n A_n^1 \sin(n\pi x), \phi_2 = \sum_k A_k^2 \sin(k\pi x)$ and $\lambda \in \mathbb{R}$. Note that

$$\mathcal{G}(\phi_1 + \lambda\phi_2) = \mathcal{G}(\phi_1) + \lambda\mathcal{G}(\phi_2) \tag{3.9}$$

that is, $\mathcal{G}$ is linear. From Riesz theorem, there is g such that

$$\mathcal{G}(\phi) = \langle g, \phi \rangle$$

Finally, by Schwarz inequality we have the Lipschitz continuity of the forward map with respect to ϕ

$$|\mathcal{G}(\phi_1) - \mathcal{G}(\phi_2)| = |\langle g, \phi_1 - \phi_2 \rangle| \leq C||\phi_1 - \phi_2||$$

For the inverse problem, let us assume that we have observations given by

$$y_j = u(z_j, 1) + \varepsilon_j, \qquad j = 1, 2, ..., p \tag{3.10}$$

where $\varepsilon_j \sim \mathcal{N}(0, \sigma^2)$. Note that under these conditions, Assumptions 1 are satisfied. Since u has the form (3.8), to generate data, we must consider a truncated sum. Since we do not have prior knowledge about this number, our results will depend strongly on the number of terms of the series in the finite-dimensional approximation of the prior and p, the number of observations. Let us assume that the data was generated for a $K = K_{Truth}$. In the numerical examples, we compute the normalization constants using formulas given in equation 2.83 to determine the optimal number of coefficients to recover the desired ϕ_{Truth}.

3.1.2 Bayesian formulation

Let us consider a Gaussian prior for ϕ following the ideas in [15] and [37]. Let $\mathcal{A} = -\dfrac{d^2}{dx^2}$ with domain

$$D(\mathcal{A}) = \{v \in H^2[0, 1] : v(0) = v(1) = 0\} \tag{3.11}$$

Note that for $\lambda > 0$, the general solution of the problem

$$-\frac{d^2}{dx^2}v - \lambda v = 0 \tag{3.12}$$

is

$$v(x) = A\cos(\sqrt{\lambda}x) + B\sin(\sqrt{\lambda}x) \tag{3.13}$$

Since $v(0) = A\cos(\sqrt{\lambda}0) + B\sin(\sqrt{\lambda}0) = A$, then $A = 0$. From $v(1) = 0$, we obtain the eigenvalues

$$\lambda_k = k^2\pi^2, \qquad k = 1, 2, 3, ... \tag{3.14}$$

We propose a Gaussian prior μ_0 for $\phi(x)$ in $\mathcal{H} \subset L^2[0,1]$ such that

$$\phi(x) \sim \mathcal{N}(0, \mathcal{C}) \tag{3.15}$$

with $\mathcal{C} = \mathcal{A}^{-1}$. Note that the set

$$\left\{\sqrt{2}\sin(k\pi x), \quad \frac{1}{(k\pi)^2}\right\}_{k=1,2,3...} \tag{3.16}$$

is an orthonormal set of eigenvectors/eigenvalues for $\mathcal{C}$. Recall from equation (2.7) that the random variable $q(x)$ given by its Karhunen-Loeve expansion

$$q(x) = \sum_{k=1}^{\infty} \frac{\sqrt{2}}{k\pi}\xi_k \sin(k\pi x) \tag{3.17}$$

with $\xi_k \sim \mathcal{N}(0,1)$, is distributed according to $\mu_0 = \mathcal{N}(0, \mathcal{C})$. Also, note that from lemma 2.1.1, we have that $\phi \in C^{0,\alpha}[0,1]$ almost surely for $0 < \alpha < 1/2$. From representation in equation (3.17), we can identify μ_0 with

$$\mu_0 = \mathcal{N}(0, \pi^{-2}) \otimes \mathcal{N}(0, (2\pi)^{-2}) \otimes \mathcal{N}(0, (3\pi)^{-2}) \otimes \mathcal{N}(0, (4\pi)^{-2}) \otimes \cdots \tag{3.18}$$

as in [37]. Finally, since we propose a Gaussian prior and the forward map is linear, it is well known that the posterior distribution μ^y is well posed and is Gaussian too, see [15]. Also, we know that

$$\frac{d\mu^y}{d\mu_0} = \frac{1}{Z}\exp\left(-\frac{1}{2}\left|\mathbf{y} - \mathcal{G}(\phi)\right|_{\Gamma}^2\right) \tag{3.19}$$

Now, we need to consider finite dimensional spaces to perform our

computations. Let us introduce the operator Q_m such that for $q \in \mathcal{H}$ given by its representation in equation (3.17),

$$Q_m(q) = q_m(x) = \sum_{k=1}^{m} \beta_k \sqrt{2} \sin(k\pi x) \tag{3.20}$$

with $\beta_k \sim \mathcal{N}(0, (k\pi)^{-2})$. This truncated sum allow us to introduced a finite dimensional approximation of the prior μ_{0m} in the subspace $V_m = \text{span}\{\sqrt{2}\sin(k\pi x)\}_{k=1}^{k=m}$. As in [37], we can write $\mu_0 = \mu_{0m} \otimes \mu_{0m}^{\perp}$.

Since the forward map introduced in the previous subsection has a closed form, we may rewrite equation (3.19) as

$$\frac{d\mu_m^y}{d\mu_0} = \frac{1}{Z_m} \exp\left(-\frac{1}{2} |\mathbf{y} - \mathcal{G}(\phi_m)|_{\Gamma}^2\right) \tag{3.21}$$

where μ_m^y is an approximation of the posterior μ^y obtained by approximating the likelihood. Since in this approximation, the right hand side is a function of $\phi_m \in V_m$, we may express μ_m^y as

$$\mu_m^y = \rho_m \otimes \mu_{0m}^{\perp} \tag{3.22}$$

where

$$\frac{d\rho_m}{d\mu_{0m}} = \frac{1}{Z_m} \exp\left(-\frac{1}{2} |\mathbf{y} - \mathcal{G}(\phi_m)|_{\Gamma}^2\right) \tag{3.23}$$

Note that μ_m^y is a measure in infinite dimensions while ρ_m is a measure in finite dimensions. Also ρ_m is part of μ_m^y where we take account of the approximation of the likelihood and the prior.

3.1.3 Numerical Results

In this subsection, we show our numerical results. From the last subsection, in each case, we propose a Gaussian prior μ_{0m} for m coefficients in the representation of the initial condition ϕ of the wave equation described in equation (3.1). Note that we don't know the number m_T of terms used to generate the data a priori. Our aim is to exemplify how the computation of Z_m in equation (3.23) allows us to determine the optimal m to perform the inference.

To compute Z_m, we use formulas in subsection 2.4.1. For each example, we generate more observations than the number of terms that we want to recover. In the following, we consider 15 observations on interior points in a regular grid in $(0, 1)$ for examples 1 and 2, and 25 observations for example 3.

1. **Example with 4 terms series.** We consider the function $\phi(x) = 1.5\sin(\pi x) + 0.8\sin(2\pi x) + 0.7\sin(3\pi x) + 0.3\sin(4\pi x)$ as initial condition. In Figure (3.1) we show the normalization constants. Note that Z_4 is the highest normalization constant for $m = 1, 2, ..., 7$. Actually, the normalization constant increase until its maximum at $m = 4$ and then decrease.

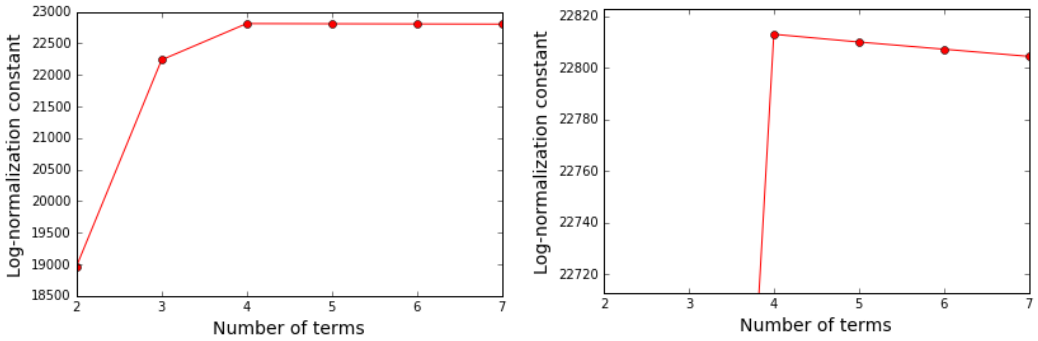

(a) (b)

Figure 3.1: (a) Normalization constants Z_m for each model. (b) Zoom of (a). The highest normalization constant is achieved with four terms.

2. **Example with 6 terms series**: We consider the function $\phi(x) = 0.9\sin(\pi x) + 0.2\sin(6\pi x)$ as initial condition. We present the normalization constants in Figure (3.2) (a). Note that adding extra terms at the beginning produces lower normalization constants, see Figure (3.2) (b). In principle, if we propose a model with the number of terms lower than 6, the highest normalization constant is for the model with just 1 term. That may be justified by noting that the coefficients for $n = 2, 3, 4, 5$ are null. This phenomenon may lead us to a wrong answer in the model selection if we compute just the first models. The highest normalization constant is achieved for 6 terms, see Figure (3.2) (c).

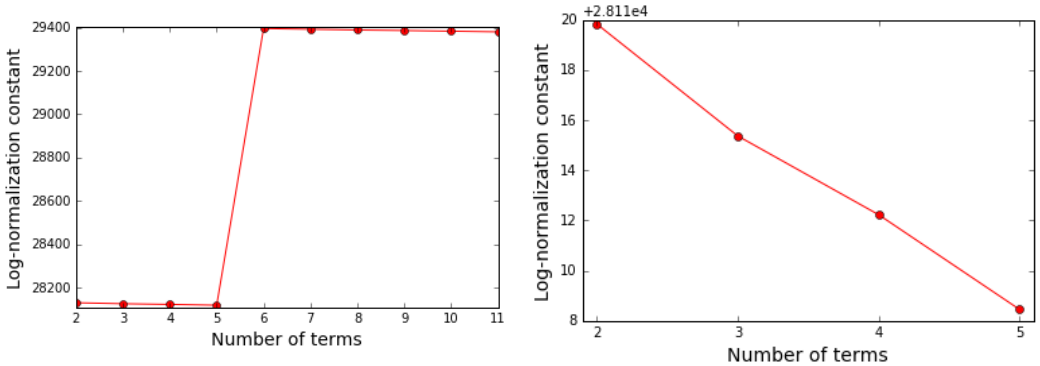

(a)

(b)

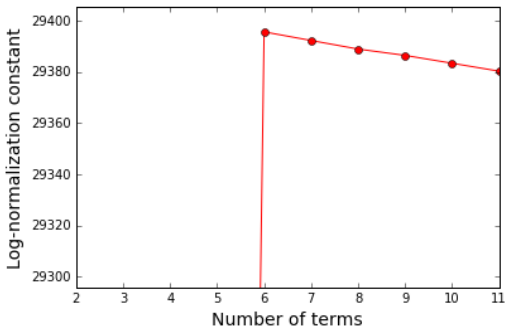

(c)

Figure 3.2: (a) Normalization constants for each model. (b) Normalization constants for the first models from 2 terms to 5 terms. (c) Normalization constants for the last models from 6 terms to 11 terms. The highest normalization constant is achieved with 6 terms. Note that model with 2 terms have more evidence than models with 3, 4 or 5 terms.

3. **Example with 20 terms series**: We consider the function $\phi(x) = \sum_{n=1}^{20} b_n \sin(n\pi x)$ where

$$b_n = \frac{(-1)^{n+1} \cdot 2n}{\pi\left(n^2 - 1/4\right)} \tag{3.24}$$

Again, the model selection strategy supports the model with 20 terms in the Fourier series, see Figure 3.3.

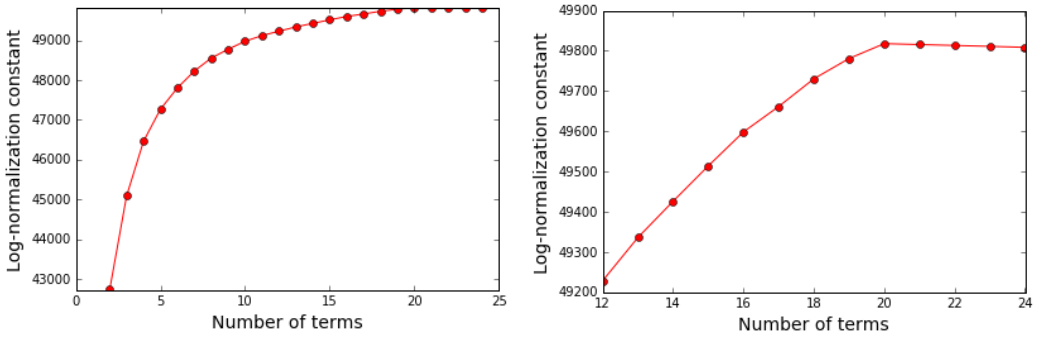

(a) (b)

Figure 3.3: (a) Normalization constants for each model. (b) Zoom of (a). The highest normalization constant is achieved with twenty terms.

3.2 Inference on the source on an elliptic equation

In this section, we propose a local mesh refinement to recover a hard inclusion for a linear problem. We compare several model selection criteria for the multimesh approach in section 2.5. To establish the initial resolution, we consider the spectrum of the prior preconditioned at the MAP estimate for uniform meshes. We consider a prior of the form in equation (2.10). Since we consider an example in dimension 2, our covariance operator is given by $\mathcal{C} = \mathcal{A}^{-2}$ to ensure the Holder-continuity in possible samples.

3.2.1 Forward map

Consider the Poisson's equation

$$-\Delta u = f, \qquad (x, y) \in \Omega = (0, 1) \times (0, 1) \tag{3.25}$$

with boundary conditions

$$u = 0, \qquad (x, y) \in \partial\Omega \tag{3.26}$$

According to [117], under these conditions, classical PDE theory guarantees that for $f \in C(\Omega)$ there exists at most one solution $u \in C^2(\Omega) \cap C(\bar{\Omega})$ of the boundary-value problem given by equations (3.25)-(3.26).

Let us assume that we have observations of u in all the mesh points of a fine mesh and we want to recover for f. We consider the multimesh case as in section 2.5 where

$$y = u_h + \eta \tag{3.27}$$

that is, we solve the forward problem at the high resolution of the data. Note that the parameter to observables $\mathcal{G}(f)$ is linear. For linear forward maps, Assumptions 1 in subsection 2.1.2 are satisfied. Typically, partial differential equations need numerical methods to be discretized and solved numerically. The Finite Element Method (FEM) is the more popular method for elliptic problems. This method requires the weak formulation of the equation (3.25). Let us consider the test function $p \in H_0^1(\Omega)$ and $f \in L^2(\Omega)$. The weak formulation for Poisson's problem is

$$\int_\Omega \nabla u \cdot \nabla p dx = \int_\Omega f p dx \tag{3.28}$$

where the integral part over the boundary disappears due to boundary conditions. $u \in H_0^1(\Omega)$ is a weak solution for the problem (3.25)-(3.26) if it satisfies equation (3.28) for all $p \in H_0^1(\Omega)$. Lax Milgram Theorem ensures the existence of the solution of this problem, see [117]. We will use this weak form to formulate the PDE-constrained optimization problem to compute the MAP estimate as explained in section 2.3. The MAP estimate will match the posterior mean since the forward model is linear and the prior is Gaussian.

3.2.2 Bayesian Formulation

We propose a Gaussian prior $\mu_0 = \mathcal{N}(f_0, \mathcal{C}_0)$, with $\mathcal{C}_0 = \mathcal{A}^{-2}$ and $\mathcal{A} = \delta I - \gamma\Delta$. Since the forward problem is linear, we know that the posterior measure will be Gaussian too. Let $\mu_{post} = \mathcal{N}(f_{post}, \mathcal{C})$. f_{post} must match the MAP estimate of the posterior measure. In this subsection, we present the formulation of the pde-constrained optimization problem as in subsection 2.3.1 to determine f_{post}. To compute the MAP, let us consider de minus log of the posterior measure

given by

$$\mathcal{J}(u,f) = \frac{1}{2}\int_{\Omega}(y-u)\,\Gamma_{obs}^{-1}\,(y-u)\,dx + \frac{1}{2}||\mathcal{A}\,(f-f_0)\,||_{L^2}^2 \tag{3.29}$$

where u is the solution of the pde problem describe in the last subsection. The lagrangian propose to solve the previous pde constrained optimization problem is given by

$$\mathcal{L}(u,p,f) = \mathcal{J}(u,f) + a(u,p) - L(p) \tag{3.30}$$

where

$$a(u,p) - L(p) = \int_{\Omega}\nabla u\cdot\nabla p dx - \int_{\Omega} f p dx$$

Recall that the forward problem is obtained by computing $\delta_p\mathcal{L}(u,p,f)(\tilde{p}) = 0, \quad \forall\tilde{p}\in H_0^1$. The adjoint problem is obtained by computing $\delta_u\mathcal{L}(u,p,f)(\tilde{u})$ and is given by

$$-\int_{\Omega}\tilde{u}\Gamma_{obs}^{-1}\,(y-u)\,dx + \int_{\Omega}\nabla\tilde{u}\cdot\nabla p dx = 0, \qquad \forall\tilde{u}\in H_0^1 \tag{3.31}$$

The weak form of the gradient is given by

$$\mathcal{G} = \int_{\Omega}\tilde{f}\mathcal{A}^2(f-f_0)dx - \int_{\Omega}\tilde{f}p dx, \qquad \forall f\in L^2 \tag{3.32}$$

where p is the solution of the adjoint problem in equation (3.31). The meta-lagrangian to compute the hessian action is given by

$$\begin{aligned}\mathcal{L}^H(u,p,f;\hat{u},\hat{p},\hat{f}) = &\textstyle\int_{\Omega}\hat{f}\mathcal{A}^2(f-f_0)dx - \int_{\Omega}\hat{f}p dx + \\ &+\textstyle\int_{\Omega}\nabla u\cdot\nabla\hat{p}dx - \int_{\Omega} f\hat{p}dx + \\ &-\textstyle\int_{\Omega}\hat{u}\Gamma_{obs}^{-1}\,(y-u)\,dx + \int_{\Omega}\nabla\hat{u}\cdot\nabla p dx\end{aligned} \tag{3.33}$$

Note that the terms W_{mm}, W_{um} and W_{mu} described in subsection 2.3.1 are null for this example. The Hessian for this case matches the Gauss-Newton Hessian

approximation. The incremental forward is given by $\delta_p \mathcal{L}^H(u, p, f; \hat{u}, \hat{p}, \hat{f})(\tilde{p})$

$$\int_\Omega \nabla \hat{u} \cdot \nabla \tilde{p} dx - \int_\Omega \hat{f} \tilde{p} dx = 0, \qquad \forall \tilde{p} \in H_0^1 \tag{3.34}$$

the incremental adjoint is given by $\delta_u \mathcal{L}^H(u, p, f; \hat{u}, \hat{p}, \hat{f})(\tilde{u})$

$$\int_\Omega \nabla \tilde{u} \cdot \nabla \hat{p} dx + \int_\Omega \hat{u} \Gamma_{obs}^{-1} \tilde{u} dx = 0, \qquad \forall \tilde{u} \in H_0^1 \tag{3.35}$$

and finally, the Hessian action on $\hat{f}$ is given by $\delta_f \mathcal{L}^H(u, p, f; \hat{u}, \hat{p}, \hat{f})(\tilde{f})$

$$\mathcal{H} = \int_\Omega \hat{f} \mathcal{A}^2 \tilde{f} dx - \int_\Omega \tilde{f} \hat{p} dx, \qquad \forall \tilde{f} \in L^2 \tag{3.36}$$

where $\hat{p}$ is the solution of the incremental adjoint. All this weak forms are computed in hIPPYlib. The optimization problem is solved by an Inexact GMRES in hIPPYlib too. We show the results of the mesh refinement in the next subsection. We compute the normalization for each mesh to determine the best model.

3.2.3 Numerical Results

In this subsection, we apply the computations of the previous section to determine the Gaussian posterior for the inverse problem described. Since the posterior is Gaussian, we can compute explicitly the normalization constant. We propose a model selection strategy to perform a local mesh refinement to recover a source with a hard inclusion. The refined meshes define a sequence of meshes. For each mesh, we can compute the evidence. By comparing the evidence of each mesh we can determine the better model. To start, we must determine an initial resolution for the problem. In figure 3.4 we show the spectrum of the prior preconditioned Hessian misfit at the MAP for several uniform discretizations. To perform a fair comparison, we need this spectrum to be invariant as in Figure 3.4 (b). This feature determines our initial resolution and causes it to not be very coarse.

To refine the mesh, we first perform the inference in the first mesh. We

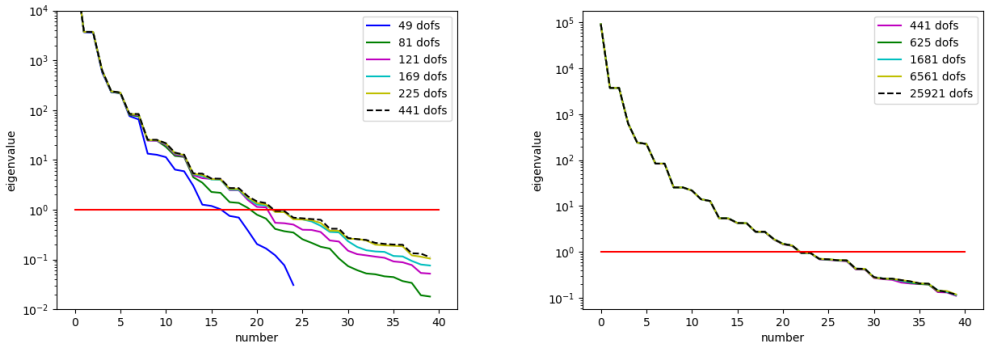

(a) (b)

Figure 3.4: Spectrum of the prior preconditioned Hessian misfit in uniform meshes: (a) Change for discretization with few degrees of freedom (b) Is invariant for discretizations with more than 441 degrees of freedom.

compare the parameter values from the posterior to the prior by computing this quantity in each node of the mesh

$$\mathcal{MS} = \frac{f_{post}}{f_0} \tag{3.37}$$

We decide to refine regions with higher $\mathcal{MS}$. That is, we define a threshold by a quantile and we refine elements where the barycenter value is higher than this threshold. This value stays fix in the following refinements. Now, we analyze the changes in quantities as normalization constants, KL divergence from the prior, L^2 errors in the parameter, and BIC with respect to the number of degrees of freedom for the mesh refinement. To perform this comparison, we generate data with a SNR of 1000. Recall that the Bayesian Information Criteria (BIC) penalized the extra number of degrees of freedom by a factor depending on the dimension of the data, see equation (2.92). For this problem, BIC does not show a typical convexity that determines an optimum, see Figure 3.5 (a). The minimum is obtained for the lower resolution considered, that is, the initial mesh. This phenomenon may be due to the strategy to obtain u_h. Recall that in the multimesh approach, the parameter is interpolated in the fine mesh to solve the forward map and obtain u_h. This strategy causes no big changes in the misfit. Nevertheless, the misfit term decreases as the number of degrees

of freedom increases. In figure 3.5 (b), we show again the logarithm of the normalization constants and the KL divergence from the prior. Note that the change between the third and fourth model is small compared to the previous ones for both quantities. In figure 3.5 (c), we can see that the L^2 error in the parameter with respect to the truth parameter increases as we refine the mesh. That means that a better model from the point of view of the evidence may not help to decrease this error.

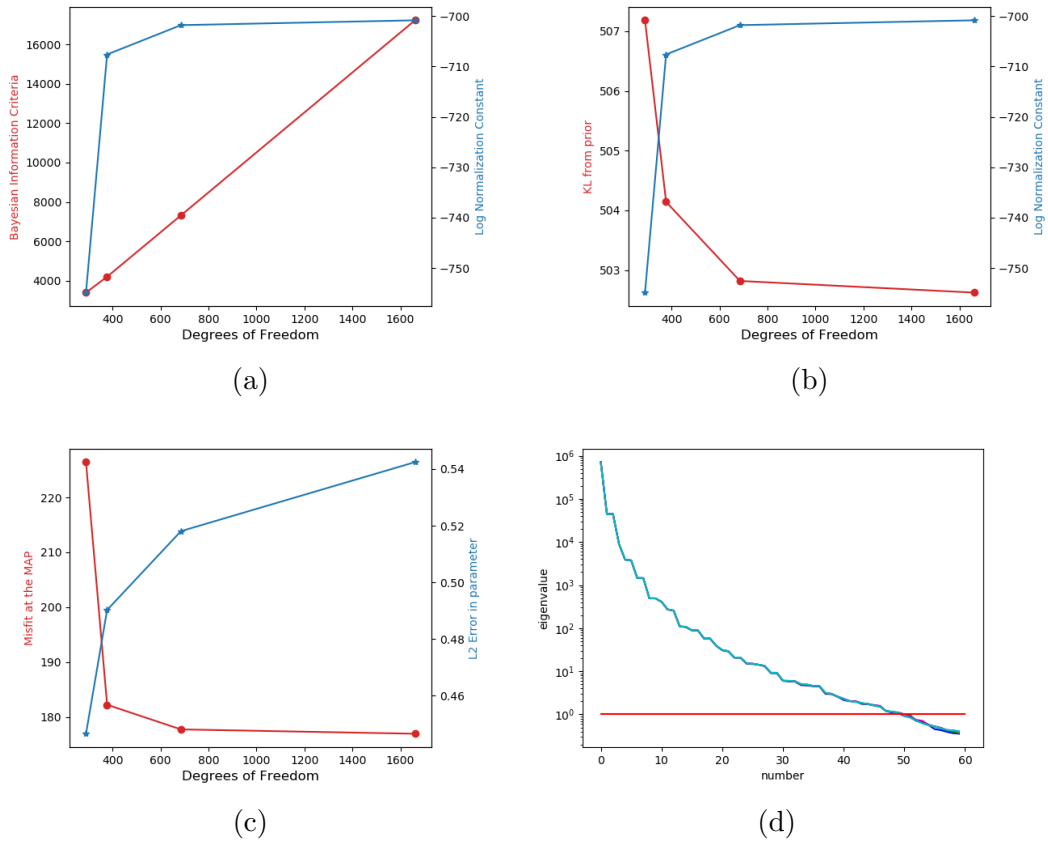

Figure 3.5: (a) The Bayesian Information Criteria (BIC) reaches its optimum value in the initial mesh. The normalization constant increases until the fourth mesh, (b) The KL divergence from the prior decreases and stabilize around the fourth mesh, similar behavior has the normalization constants, (c) The misfit decreases and the L2 error with respect to the true parameter increases for each new refined mesh, (d) The spectrum of the prior preconditioned Hessian at the posterior mean for each mesh.

Other quantities may be included in the criteria to refine. In this case, since we work for Gaussian prior and posterior, it is natural to think about including variance information. Figure 3.8 (b) shows the posterior pointwise variance for the first mesh. It can be noticed that high variance regions are outside the inclusion area. Including this information in the criteria may lead to refining other regions besides that of inclusion, see Figure 3.9 (a). Again the evidence may allow us to compare meshes generated by different criteria, see Figure 3.9 (b). Finally, as may be expected, the big trouble in this inference process is that we can not recover the boundary of the inclusion, see 3.8 (a).

In the next section, we show results in a linearized problem that mixes information about the mean and the variance to obtain better refinement strategies.

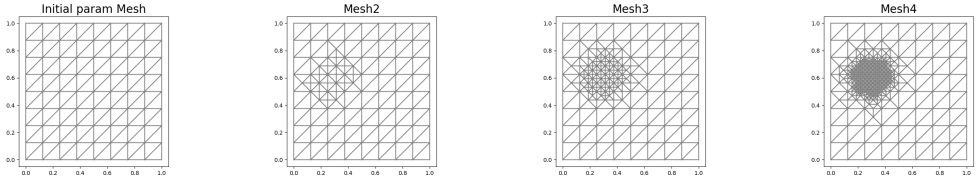

(a) (b) (c) (d)

Figure 3.6: Succesive meshes obtained by the mesh refinement. We compute the quotient between the posterior mean and the prior mean on the parameter. We refine refine areas with higher values of this quotient.

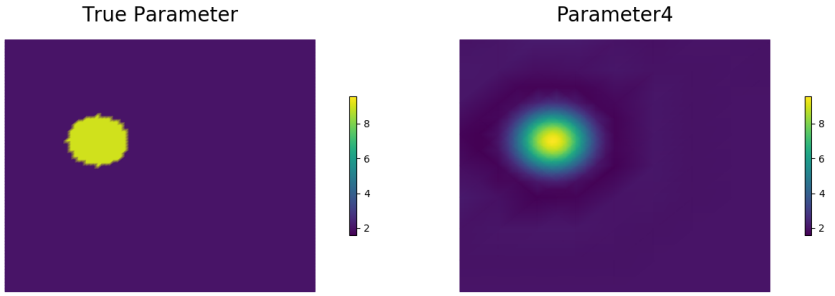

Figure 3.7: True param at left and parameter recovered at right using mesh4

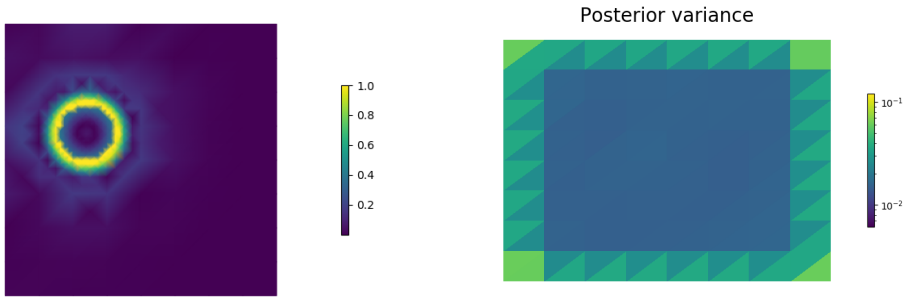

(a) (b)

Figure 3.8: (a) Relative error at mesh 4, (b) Pointwise posterior variance in the initial mesh.

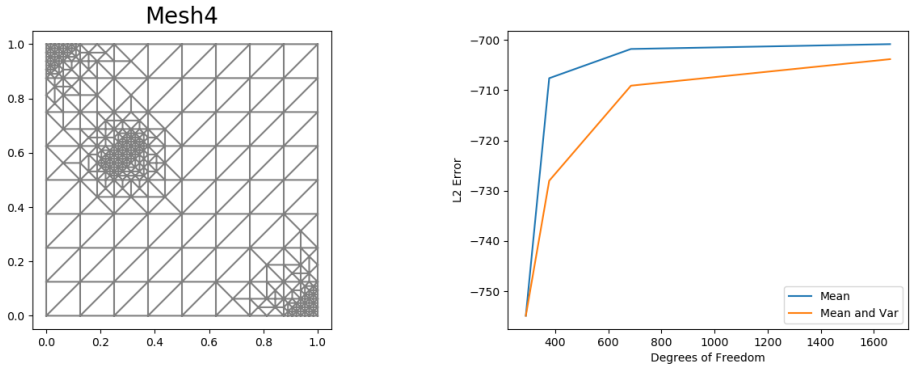

(a) (b)

Figure 3.9: (a) Mesh 4 using a criteria with the mean and the variance, (b) Comparison of normalization constant of each model(mesh).

3.3 Mesh Refinement in the Inference of a coefficient on an elliptic equation

In this subsection, we perform the local mesh refinement in a nonlinear example governed by an elliptic PDE. To approximate the evidence of each model we linearized the forward map around the MAP estimate. As we mentioned in the previous example, we can add information from the Gaussian approximation of the posterior distribution to the refinement criterion.

3.3.1 Forward map

Consider the elliptic equation

$$-\nabla \cdot (k\nabla u) = f, \qquad (x, y) \in \Omega = (0, 1) \times (0, 1) \tag{3.38}$$

with boundary conditions

$$u = 0, \qquad (x, y) \in \partial\Omega \tag{3.39}$$

Consider the function f given by

$$f(x, y) = 1 \tag{3.40}$$

Let us assume that we have observations of u in all the mesh points of a fine mesh and we want to recover the coefficient $k = k(x, y)$. For this case, we need

$$k(x, y) \geq k_{min} > 0 \tag{3.41}$$

Lax-Milgram theory yields that if k satisfies condition (3.41) then problem (3.38) with bondary conditions (3.39) has a weak solution. Since $k_{min} > 0$, we will consider

$$k(x, y) = \exp(m(x, y)) \tag{3.42}$$

to avoid the numerical problems caused by trying to force positivity. We perform the inference for the field $m(x, y)$. We consider the multimesh case as in section 2.5 where we assume the data y satisfies

$$y = u_h(m) + \eta \tag{3.43}$$

with η is a random gaussian noise. In this case, the parameter to observables $\mathcal{G}(m) = u_h(m)$ is nonlinear. As we mentioned before, partial differential equations needs numerical methods to be discretized and solved numerically. We show the weak formulation of the equation in (3.38) used to implemented the Finite Element Method (FEM) in FEniCS. Let us consider the test function

$p \in H_0^1(\Omega)$ and $f \in L^2(\Omega)$. The weak formulation for this elliptic problem is

$$\int_\Omega e^m \nabla u \cdot \nabla p dx = \int_\Omega f p dx \tag{3.44}$$

where the integral part over the boundary disappear due to boundary conditions. $u \in H_0^1(\Omega)$ is a weak solution for the problem (3.38)-(3.39) if it satisfies equation (3.44) for all $p \in H_0^1(\Omega)$. We will use this weak form to formulate the pde-constrained optimization problem to compute the MAP estimate as explained in section 2.3.

3.3.2 Bayesian Formulation

We propose a Gaussian prior $\mu_0 = \mathcal{N}(m_0, \mathcal{C}_0)$, with $\mathcal{C}_0 = \mathcal{A}^{-2}$ and $\mathcal{A} = \delta I - \gamma\Delta$. In this case, we want to approximate the posterior measure by a Gaussian measure centered at the MAP estimate. Let $\mu_{post}^G = \mathcal{N}(m_{MAP}, \mathcal{C})$. m_{post} is the MAP estimate of the posterior measure μ_{post}. In this subsection, we present the formulation of the pde-constrained optimization problem as in subsection 2.3.1 to determine m_{MAP}. To compute the MAP, let us consider de minus log of the posterior measure given by

$$\mathcal{J}(u, m) = \frac{1}{2}\int_\Omega (y - u)\, \Gamma_{obs}^{-1}\, (y - u)\, dx + \frac{1}{2}||\mathcal{A}\,(m - m_0)\,||_{L^2}^2 \tag{3.45}$$

where u is the solution of the pde problem described in the last subsection. The lagrangian proposed to solve the previous pde constrained optimization problem is given by

$$\mathcal{L}(u, p, m) = \mathcal{J}(u, m) + a(u, p, m) - L(p) \tag{3.46}$$

where

$$a(u, p, m) - L(p) = \int_\Omega e^m \nabla u \cdot \nabla p dx - \int_\Omega f p dx$$

Recall that the forward problem is obtained by computing $\delta_p \mathcal{L}(u, p, m)(\tilde{p}) = 0, \quad \forall \tilde{p} \in H_0^1$. The adjoint problem is obtained by computing $\delta_u \mathcal{L}(u, p, m)(\tilde{u})$

and is given by

$$-\int_\Omega \tilde{u}\Gamma_{obs}^{-1}(y-u)\,dx + \int_\Omega e^m \nabla\tilde{u}\cdot\nabla p dx = 0, \qquad \forall \tilde{u}\in H_0^1 \tag{3.47}$$

The weak form of the gradient is given by

$$\mathcal{G} = \int_\Omega \tilde{m}\mathcal{A}^2(m-m_0)dx + \int_\Omega \tilde{m}e^m\nabla u\cdot\nabla p dx, \qquad \forall \tilde{m} \tag{3.48}$$

where p is the solution of the adjoint problem in equation (3.47). The meta-lagrangian to compute the hessian action is given by

$$\begin{aligned}\mathcal{L}^H(u,p,m;\hat{u},\hat{p},\hat{m}) = \quad & \textstyle\int_\Omega \hat{m}\mathcal{A}^2(m-m_0)dx + \int_\Omega \hat{m}e^m\nabla u\cdot\nabla p dx + \\ & + \textstyle\int_\Omega e^m\nabla u\cdot\nabla\hat{p}dx - \int_\Omega f\hat{p}dx + \\ & - \textstyle\int_\Omega \hat{u}\Gamma_{obs}^{-1}(y-u)\,dx + \int_\Omega e^m\nabla\hat{u}\cdot\nabla p dx\end{aligned} \tag{3.49}$$

The incremental forward is given by $\delta_p\mathcal{L}^H(u,p,m;\hat{u},\hat{p},\hat{m})(\tilde{p})$

$$\int_\Omega \hat{m}e^m\nabla u\cdot\nabla\tilde{p}dx + \int_\Omega e^m\nabla\hat{u}\cdot\nabla\tilde{p}dx = 0, \qquad \forall\tilde{p}\in H_0^1 \tag{3.50}$$

the incremental adjoint is given by $\delta_u\mathcal{L}^H(u,p,m;\hat{u},\hat{p},\hat{m})(\tilde{u})$

$$\int_\Omega \hat{m}e^m\nabla\tilde{u}\cdot\nabla p dx + \int_\Omega e^m\nabla\tilde{u}\cdot\nabla\hat{p}dx + \int_\Omega \hat{u}\Gamma_{obs}^{-1}\tilde{u}dx = 0, \qquad \forall\tilde{u}\in H_0^1 \tag{3.51}$$

and finally, the Hessian action on $\hat{m}$ is given by $\delta_m\mathcal{L}^H(u,p,m;\hat{u},\hat{p},\hat{m})(\tilde{m})$

$$\begin{aligned}\mathcal{H} = \quad & \textstyle\int_\Omega \hat{m}\mathcal{A}^2\tilde{m}dx + \int_\Omega \hat{m}\tilde{m}e^m\nabla u\cdot\nabla p dx + \\ & + \textstyle\int_\Omega \tilde{m}e^m\nabla u\cdot\nabla\hat{p}dx + \int_\Omega \tilde{m}e^m\nabla\hat{u}\cdot\nabla p dx, \qquad \forall\tilde{m}\in\end{aligned} \tag{3.52}$$

where $\hat{u}$ is the solution of the incremental forward and $\hat{p}$ is the solution of the incremental adjoint. All this weak forms are computed in hIPPYlib. The optimization problem is solved by an Inexact Newton GMRES in hIPPYlib too.

We show the results of this problem in the next subsection and we compare these results for different resolutions in the parameter.

3.3.3 Score Oriented Mesh Refinement

To decide which elements must be refined to improve the inference, we must define a criterion. From the point of view of Bayesian statistical decision theory [118], the criterion may be understood as the optimum value of the expectation of a weighted loss function. In this case, the criterion proposed includes information about the mean and the variance of the parameter of interest. Note that this information is obtained straightforwardly from the Gaussian approximation of the posterior. Also, the criterion includes the comparison with respect to the corresponding values imputed from the prior.
Let us consider the loss function

$$\mathcal{L}(\mu, a) = w(\mu)(\mu - a)^2 \tag{3.53}$$

with $w(\mu) = w = \dfrac{\mu_{post}}{\mu_{prior}\sigma^2_{prior}}$, where μ is our parameter of interest and a an estimator. Then, the expected loss function under the posterior distribution of μ is

$$\mathcal{L}^*(a) = w\left(\sigma^2_{post} + (\mu_{post} - a)^2\right) \tag{3.54}$$

The global minimum of $\mathcal{L}^*(a)$ defined by (3.54) is reached at $a = \mu_{post}$. The value at this local minimum is precisely

$$ADS = \frac{\mu_{post}}{\mu_{prior}} \cdot \frac{\sigma^2_{post}}{\sigma^2_{prior}} \tag{3.55}$$

Since ADS is a pointwise criterion, we refine regions with higher ADS when the application expected higher values of the mean for the anomalies. The rationale of ADS (3.55) is that anomalous values of the parameter are to be decided upon the reference parameter values. By introducing the ADS, we aim at addressing several issues: (i) to refine a region with inclusion with higher of lower stiffness with respect to the prior, (ii) to refine more than one region, if it is the case of two or more stiff inclusions and (iii) not to refine regions with

accurate prior knowledge. Since ADS is dimensionless by construction, we will define a refinement threshold in terms of a quantile. As in the previous examples, we compute the evidence for each mesh to decide which mesh is better. Also, we consider other refinement criteria and compare meshes for different criteria by computing its normalization constants. The refinement is performed directly by FEniCS [99] tools.

3.3.4 Numerical Results

In this subsection, we present the results of the model selection. We compare four types of refinement:

1. Comparing the changes on the posterior mean with respect to the prior mean.

2. Comparing the changes on the posterior mean and variance with respect to the prior mean and variance (ADS introduced the previous subsection).

3. Refining the region of the boundary of the inclusion.

4. Refining the element with a higher gradient.

In figure 3.10 we show the successive meshes for criterion 1. We show the successive meshes for other criteria in Appendix B. For each criterion, we compute the evidence for each mesh 5 times. Finally, we compare the log of the normalization constants against the degrees of freedom in figure 3.11 (d). Note the criteria based on ADS reaches high evidence with fewer degrees of freedom than other criteria. If we compare the fifth mesh for each criterion, the criteria that focus in recover the boundary reaches the highest evidence with the price of a high number of degrees of freedom. Other examples can be seen in Appendix B including examples with two inclusions and with prior knowledge included to not refine a known region.

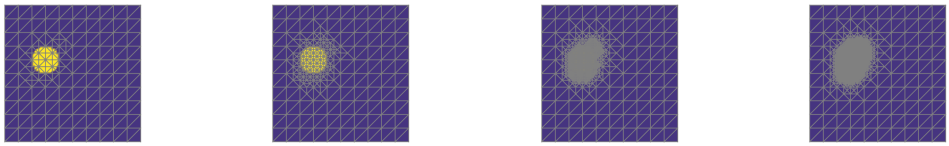

(a) (b) (c) (d)

Figure 3.10: Local refinement based on the change of the posterior mean with respect to the prior mean (a) mesh 2, (b) mesh3, (c) mesh4, (d) mesh5.

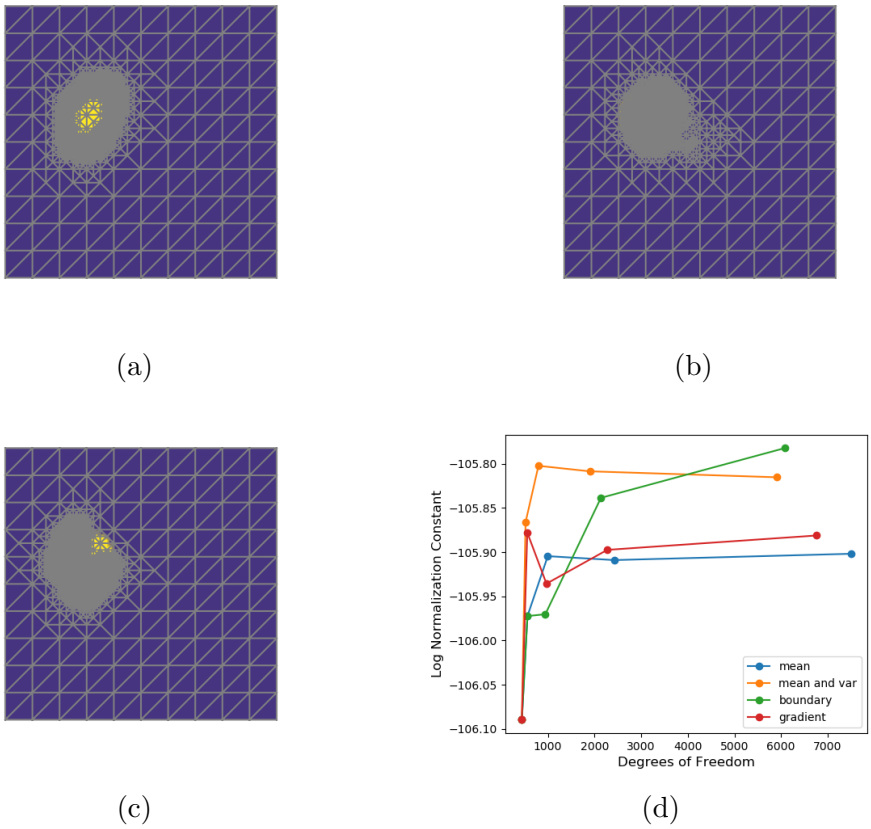

(a) (b) (c) (d)

Figure 3.11: Last mesh of the refinement for several criteria (a) for the boundary, (b) using variance and mean, (c) using the gradient. In (d) we show the normalization constants for each mesh and each criteria. Note that the criterion with mean and variance achieves a high normalization constant with less degrees of freedom.

3.4 A comparison of sampling methods applied to the Bayesian inference of a diffusion coefficient in 1D

In this section, we compare two different approaches to sampling the posterior probability distribution that arises in the Bayesian solution of an inverse problem. The idea is to compare the performance of two methods representing different families of probability transition kernels: Hessian approximated Monte Carlo (HAMCMC) [74], which is a quasi-Newton method, and affine invariant Monte Carlo (t-walk) [65], which is a derivative-free method. To achieve our goal, we have considered the problem of estimating a diffusion coefficient in 1D as a case study. To carry out our analysis we have chosen an intrinsically finite-dimensional problem arising from estimating a piece-wise constant diffusion coefficient in a two-point boundary value problem.

3.4.1 Forward map

Let us consider the two-point boundary value problem

$$-\left(k(x,\theta)p_x\right)_x = 0, \quad x \in (0,1) \tag{3.56}$$

$$p(0) = p^-, \qquad p(1) = p^+. \tag{3.57}$$

where $p^+ > p^-$, $k(x,\theta) > 0$ is the diffusion coefficient, and $\theta \in \mathbb{R}^m$ is a vector of input parameters. Then, the solution of problem (3.56)-(3.57) can be explicitly written as follows

$$-(k(x,\theta)p_x)_x = 0 \quad \Rightarrow \quad k(x,\theta)p_x = C, \quad C \in \mathbb{R}$$

$$\Rightarrow \quad p_x = \frac{C}{k(x,\theta)} \quad \Rightarrow \quad \int_0^x p_x dt = \int_0^x \frac{C}{k(t,\theta)} dt$$

$$\Rightarrow \quad p(x) - p(0) = \int_0^x \frac{C}{k(t,\theta)} dt + D \quad \Rightarrow \quad p(x) = p^- + \int_0^x \frac{C}{k(t,\theta)} dt$$

Since $p(1) = p^- + \displaystyle\int_0^1 \frac{C}{k(t,\theta)}dt = p^+$, then

$$C\int_0^1 \frac{1}{k(t,\theta)}dt = p^+ - p^-$$

Recall that $k(x,\theta) > 0$, so consider $u(x,\theta)$ such that $k(x,\theta) = \exp(u(x,\theta))$. So

$$C\int_0^1 \exp(-u(t))dt = p^+ - p^-$$

Finally, the solution for the problem (3.56)–(3.57) is

$$p(x) = p^- + \frac{p^+ - p^-}{\int_0^1 \exp(-u(t,\theta))dt}\int_0^x \exp(-u(t,\theta))dt \tag{3.58}$$

In [15], the author consider the observation operator

$$\mathcal{G}(u) = (p(x_1), \ldots, p(x_q))^T \tag{3.59}$$

and state in Lemma 3.3 that $\mathcal{G} : C[0,1] \to \mathbb{R}^q$ is Lipschitz and satisfies the bound

$$|\mathcal{G}(u)| \leq \sqrt{q}p^+ \tag{3.60}$$

This bound allows to proof the Lipschitz continuity of the forward map with respect to the parameter given by

$$|\mathcal{G}(u) - \mathcal{G}(v)| \leq \frac{3}{2}(p^+ - p^-)\exp(||v||_\infty + \max\{||u||_\infty, ||u||_\infty\})||u - v||_\infty \tag{3.61}$$

This condition establish the well-posedness of the posterior measure using a Gaussian prior on u, see details in Section 3.3 of [15].

In this subsection, we consider that equation (3.58) defines a direct problem or *forward mapping* $\mathcal{M}$ from input parameters θ in $k = k(x,\theta)$ to a quantity of interest $p = p(x)$ evaluated at points $0 < x_1 < \ldots < x_q < 1$

$$\mathcal{M} : k \longrightarrow \{p(x_i)\}_{i=1}^q \tag{3.62}$$

From equation (3.62) we define the inverse problem of estimating a piece-wise constant diffusion coefficient $k = k(x, \theta)$, given measurements $\{p(x_i)\}_{i=1}^{q}$.

We shall consider a piece-wise constant diffusion coefficient $k = k(x, \theta)$

$$k(x) = \begin{cases} k_1, & 0 \le x \le a, \\ k_2, & a < x \le b, \\ k_1, & b < x \le 1, \end{cases} \tag{3.63}$$

for some $0 \le a \le b \le 1$. Here, the vector of input parameters is $\theta = (a, u_1, b, u_2)$, where $u_1 = \log k_1$ and $u_2 = \log k_2$.

3.4.2 Observational Model and Bayesian Formulation

Let us consider noisy observations of $p(x_i)$ for k defined by equation (3.63)

$$y_k = p(x_i) + \epsilon_i, \qquad i = 1, 2, \dots q$$

where $0 < x_1 < \ldots < x_q < 1$, and $\epsilon_i \sim \mathcal{N}(0, \sigma^2)$ with $\sigma = 0.01$.

To generate synthetic data, we have solved the problem (3.56)-(3.57) using 100 quadrature points in the interval $[0, 1]$ and the trapezoidal rule. Then, we introduce noise on q evenly spaced points. To simulate the direct problem during the MCMC sampling, we solve the problem (3.56)-(3.57) using 60 points on the interval $[0, 1]$. The choice of the standard deviation σ is based on the signal to noise ratio:

$$\text{SNR} \stackrel{\text{def}}{=} \frac{\min y_i}{\sigma} = 100.$$

Assuming that input parameters and noise in the data are independent, and θ denotes the vector of input parameter, then for each $i = 1, 2, \dots q$ we have

$$\pi_{Y_i|\Theta}(y_i|\theta) = \frac{1}{\sqrt{2\pi\sigma^2}} \exp\left(-\frac{1}{2\sigma^2}|y_i - p(x_i)|^2\right). \tag{3.64}$$

Consequently,

$$\begin{aligned}\pi_{Y|\Theta}(\mathbf{y}|\theta) &= \frac{1}{(2\pi\sigma^2)^{q/2}} \prod_{i=1}^{q} \exp\left(-\frac{1}{2\sigma^2}|y_i - p(x_i)|^2\right) \\ &= \frac{1}{(2\pi\sigma^2)^{q/2}} \exp\left(-\frac{1}{2\sigma^2}\sum_{i=1}^{q}|y_i - p(x_i)|^2\right)\end{aligned} \tag{3.65}$$

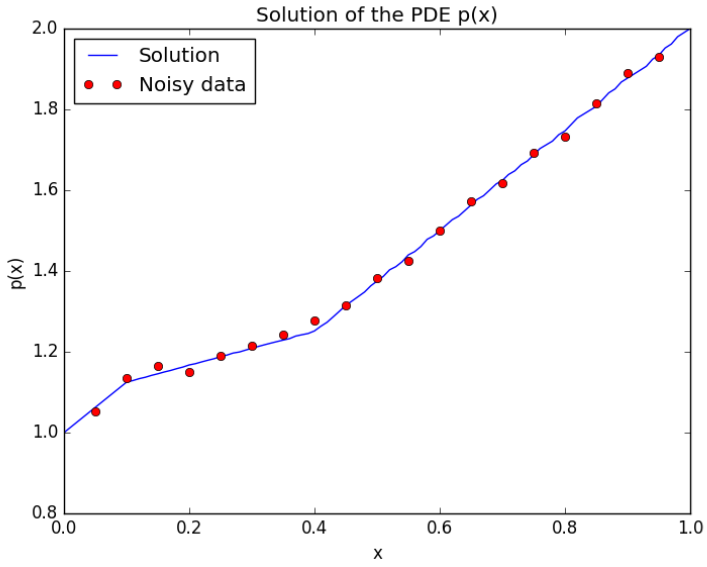

Figure 3.12: **Synthetic data**. For the numerical experiment we consider $q = 19$ synthetic data points.

In the present case, we propose Gaussian prior distributions for all the parameters. Recall that a Gaussian distribution can be described just with two instrumental parameters μ and η. That is, $\pi(x) \sim \mathcal{N}(\mu, \eta^2)$ means that x follows a Gaussian distribution with mean μ and variance η^2. The proposals for each parameter on θ are

$$\begin{aligned} a &\sim \mathcal{N}(0.2, 0.2^2), \qquad & b &\sim \mathcal{N}(0.5, 0.2^2), \\ u_1 &\sim \mathcal{N}(0.2, 1.0), \qquad & u_2 &\sim \mathcal{N}(0.5, 1.0). \end{aligned}$$

We may use the definitions above to write the prior distribution as follows

$$\pi_\Theta(\theta) = \prod_{j=1}^{4} \frac{1}{\sqrt{2\pi\eta_j^2}} \exp\left(-\frac{1}{2\eta_j^2}|\theta_j - \mu_j|^2\right) \tag{3.66}$$

3.4.3 Numerical Results

In Figures 3.13 and 3.14, we compare the sampling between HAMCMC, HAMCMC-MH and t-walk. Our results show a meaningful difference when a Metropolis-Hastings criterion is introduced in HAMCMC algorithm. For HAMCMC-MH, the sampling shows posterior distributions more concentrated.

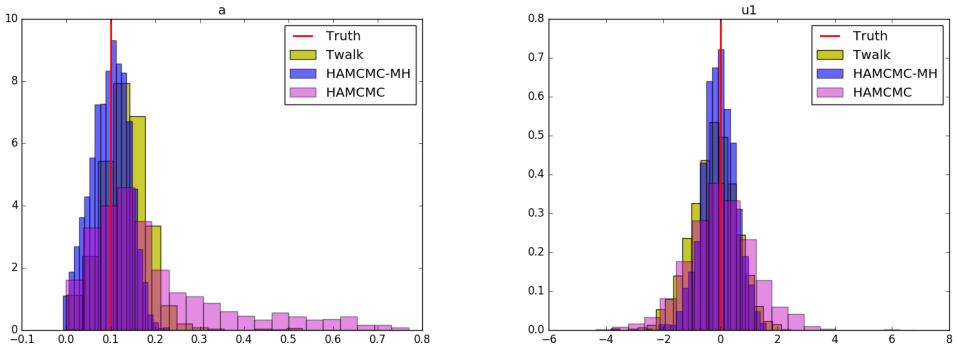

(a) Posterior distributions for a (b) Posterior distributions for u_1

Figure 3.13: **Sampling of the three algorithms** HAMCMC fails to recover the variance of parameter a.

The above results were obtained through three chains. For t-walk: a chain with 200000 points in yellow; for HAMCMC: a chain with 30000 points in magenta; for HAMCMC-MH: a chain with 10000 points in blue. Table 3.1 shows conditional means (CM) of a, u_1, b, u_2 for each algorithm. Table 3.2 shows the values of the maximum a posteriori (MAP) estimators, which can produce a better fit to the data (see Figure 3.15). The estimated variance for each parameter is shown in Table 3.3.

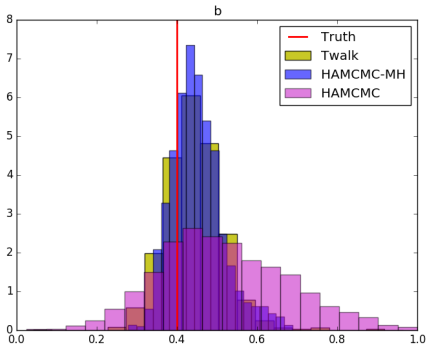

(a) Posterior distributions for b

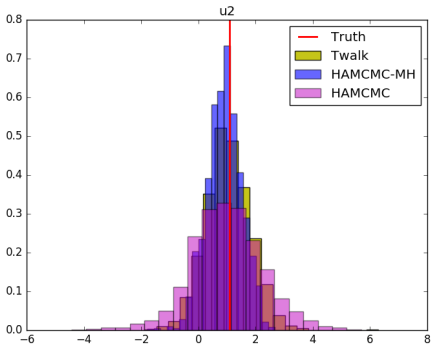

(b) Posterior distributions for u_2

Figure 3.14: **Sampling of the three algorithms** HAMCMC fails to recover the variance of parameter a.

	a	u_1	b	u_2
HAMCMC	0.19	0.03	0.51	1.0
HAMCMC-MH	0.097	-0.06	0.45	0.9
Twalk	0.13	-0.24	0.44	1.04
Truth	0.1	0.0	0.4	1.09

Table 3.1: CM Estimators

	a	u_1	b	u_2
HAMCMC	0.10	-0.39	0.41	0.75
HAMCMC-MH	0.11	-0.02	0.44	0.88
Twalk	0.11	-0.18	0.44	0.8
Truth	0.1	0.0	0.4	1.09

Table 3.2: MAP Estimators

	a	u_1	b	u_2
HAMCMC	0.024	1.39	0.025	1.59
HAMCMC-MH	0.0018	0.34	0.0041	0.36
Twalk	0.003	0.647	0.005	0.62

Table 3.3: Estimated value of the variance

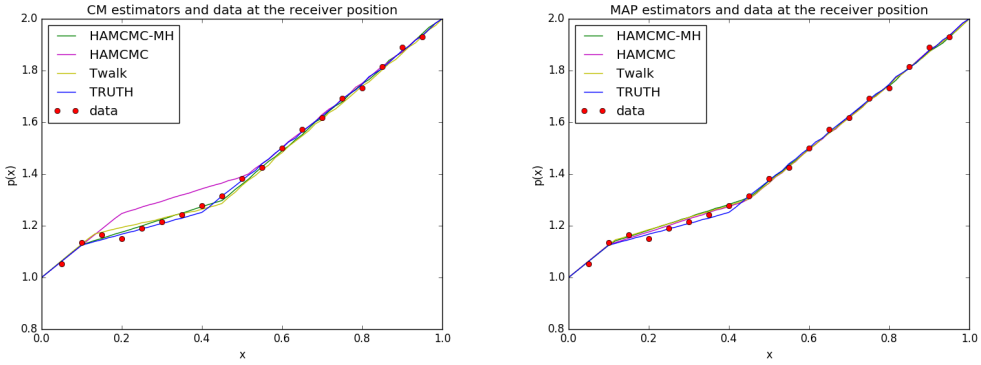

(a) CM estimators (b) MAP estimators

Figure 3.15: Fit to the data and solution of estimators

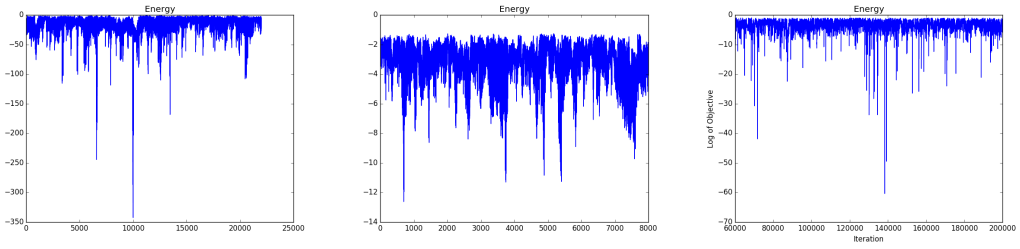

(a) HAMCMC (b) HAMCMC-MH (c) Twalk

Figure 3.16: Trace plots: Note that the number of points in the chain may vary according to the sampling scheme. HAMCMC-MH spend less than half of iterations than the non-metropolized version. Even if t-walk needs considerable more iterations, since is free derivative information, it spend less time.

3.5 Frequency design on the Algebraic Inversion for MRE

In this subsection, the aim is to apply an optimal design approach to decide about the number and which frequencies to incorporate in the multifrequency algebraic inversion in MRE described in subsection 2.6.

3.5.1 Experimental Design

Experimental design dictates how data should be collected. According to [119], an optimal experimental design (OED) should provide the maximum amount of information with the minimum cost. OED is very challenging in this context due to the high cost in the evaluation of the model, which is governed by a partial differential equation. Assumptions in the Algebraic Inversion allow us to propose and apply some methods of OED well established in statistics.

Let us consider the following equation:

$$y_j = u(w_j, \mu) + \varepsilon_j, \qquad j = 1, \cdots, N \tag{3.67}$$

where y_j is a generated data for each j, $u(w_j, \mu)$ is the solution of the PDE given by equation (2.104), μ is the unknown parameter and w_j are experimental conditions, in this case, the frequencies at which the data is generated. Let us denote by $\mathcal{W}$ the design region. The idea is to determine a design to decrease model uncertainty. According to [119], two parts must be considered in this process. First, an excitation part, related to the conditions in the model, for example, the frequencies. Second, the response part, related to how and where to measure the system response. In this work, we will consider just the first part.

To compare different designs and find an optimal, we need objectives and criteria. As we mentioned before, the objective in this section is to propose a design in the frequencies to decrease the uncertainty of the AIDE estimate. A design in the frequencies includes which and how many frequencies are needed. Recall that assumptions in the algebraic inversion can produce artifacts in the estimates, see Figure 3.17 (a). In this case, from equation (2.107), we can approximate the variance of the estimator in a specific element K_i by

$$Var(\mu_i) = \frac{\sigma^2}{X_i^T X_i} \tag{3.68}$$

where X_i corresponds to the vector values of the laplacian in the element and σ^2 the noise in the data. We show the variance associated with the AIDE estimate in Figure 3.17 (b).

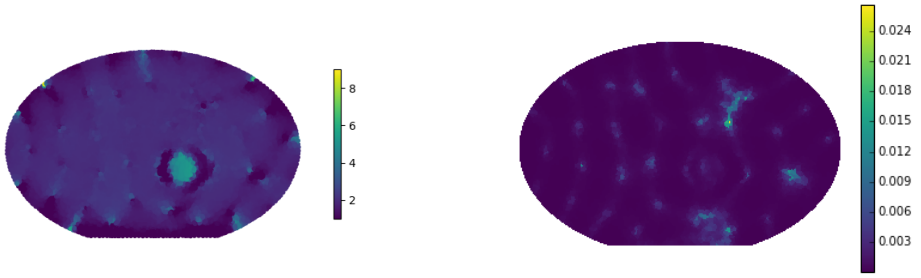

(a) (b)

Figure 3.17: (a) Parameter recover with Algebraic Inversion at frequency 20 Hz. (b) Variances of the least-square estimates in (a).

Recall that acquisitions at different frequencies can be used to circumvent the conditioning and uniqueness concerns in the inversion process and to produce fewer artifacts. To exemplify this, we compute the AIDE estimate using data at two frequencies, one corresponds to the 20 Hz estimate shown previously. We show the variances of our results in Figure 3.18. Note that the maximum decrease one order of magnitude by adding data at a second frequency.

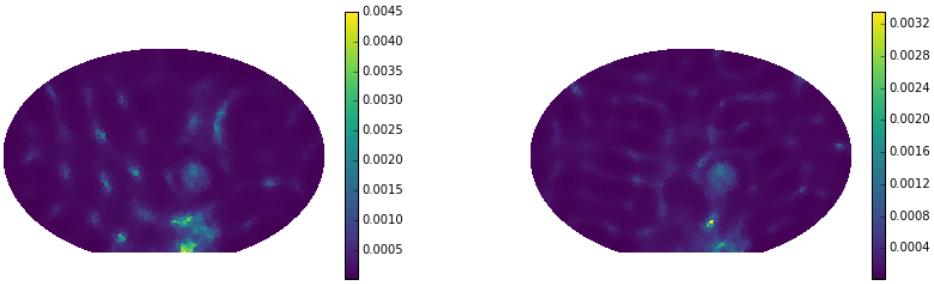

(a) (b)

Figure 3.18: Adding data at a second frequency (a) Variances of the least-square estimates with data at frequencies 20 and 25 Hz, (b) Variances of the least-square estimates with data at frequencies 20 and 30 Hz.

According to [120], the aim in the MV-Criterion is to minimize the sum of the variances of the-least squares estimator. This criterion is also known as

the A-optimal approach. In this work, we compute the trace of the variance matrix of the multifrequency AIDE estimate. The optimal design will choose the frequency which minimizes this trace. Figure 3.19 shows the traces using data at a single frequency in (a) and adding a second frequency in (b). The comparison between the values of the traces for one and two frequencies or two and three are shown in Figure 3.20.

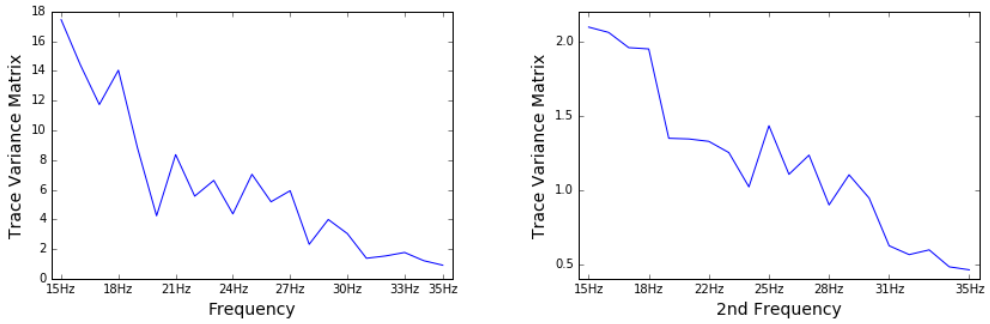

(a) (b)

Figure 3.19: Trace of the variances matrix (a) for estimates at one single frequency, (b) Adding data at a second frequency to data at 20 Hz.

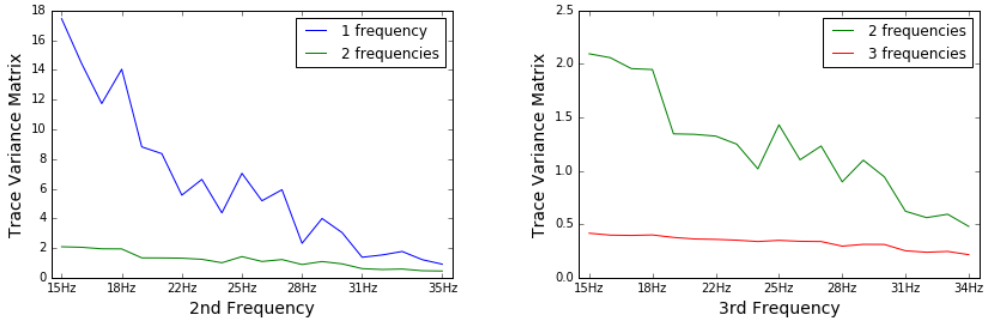

(a) (b)

Figure 3.20: Trace of the variances matrix (a) values for one and two frequencies, (b) values for two and three frequencies.

3.5.2 Numerical Results

Following the idea introduced in the last subsection, we determine a design for the frequencies. Since we work with generated data, we can compute the L^2 error between the estimated parameter and the true parameter. Note that after 8 frequencies, the trace value continues to decrease, while the L^2 error reaches a minimum at the sixth frequency, see Figure 3.21.

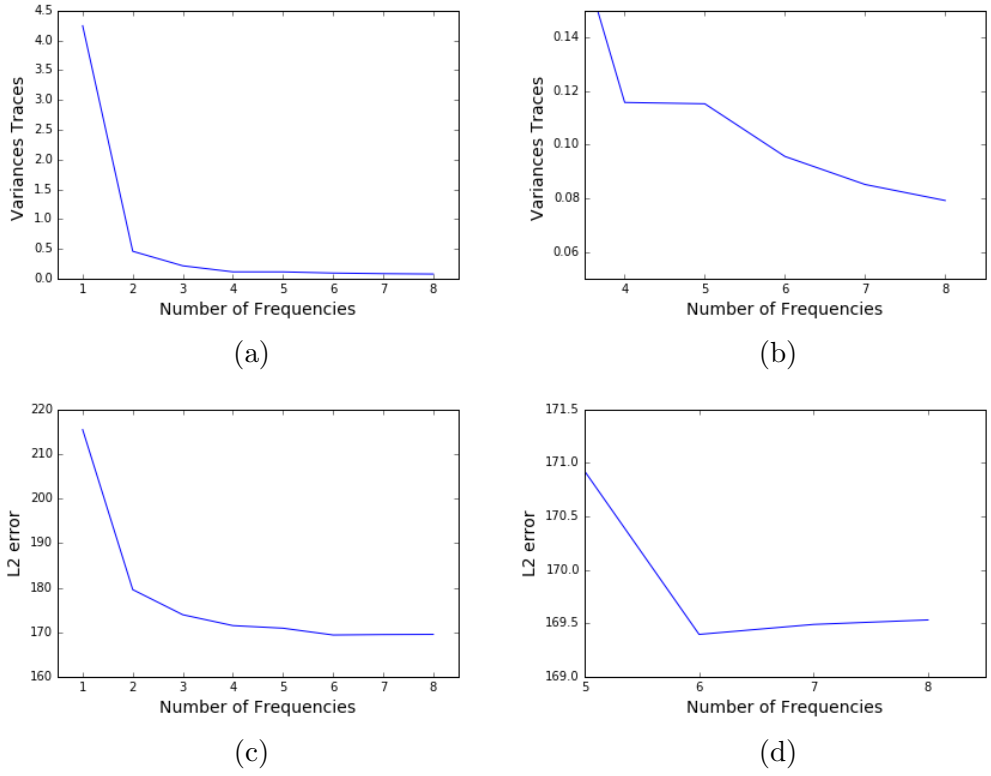

Figure 3.21: Optimal design with frequencies $20, 35, 34, 32$ and 33 Hz (a) The trace of the variances matrix decrease by adding frequencies, (b) The trace remains almost constant from fourth to fifth frequency (c) The L^2 error between the estimate and the true parameter decrease by adding frequencies until the sixth frequency, (d) The L^2 error reach a minimum in the sixth frequency.

The idea of minimizing the trace allows us to choose the next frequency to add to the design. Now, to determine the last frequency, we will compute the

absolute decrease by adding an extra frequency. Consider the next quantity

$$\mathcal{G}_i = Tr_i - Tr_{i+1} \tag{3.69}$$

where Tr_i denotes the Trace in the design with i frequencies. For the optimal design, we show the values of $\mathcal{G}_i$ in Figure 3.22. Note that the minimum is achieved when we add the fifth frequency.

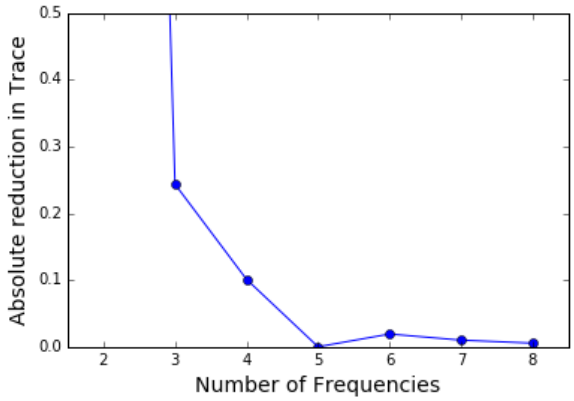

Figure 3.22: Absolute reduction in the Trace of the optimal design

We compare the results of the optimal design against the results displayed in Figure 2.4 (b) in Figure 3.24. We show the true parameter to recover in Figure 3.23. Also, we show the relative errors for each design in Figure 3.25 and the variance of the estimates in Figure 3.26. Note that the optimal design allows the bigger variance of the estimates to correspond to the inclusion area. Also, the maximum of the variances is a decrease three times for the optimal design. The relative error decrease in the inclusion area and in the zone corresponding to the back of the patient. Recall that the forward problem has homogeneous Dirichlet boundary conditions in this area what produces a big uncertainty in the AIDE estimate.

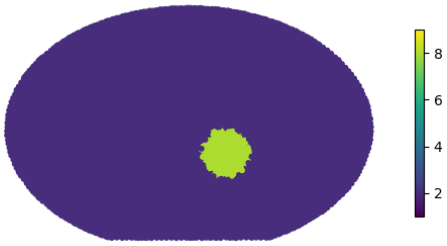

Figure 3.23: True paramater to recover

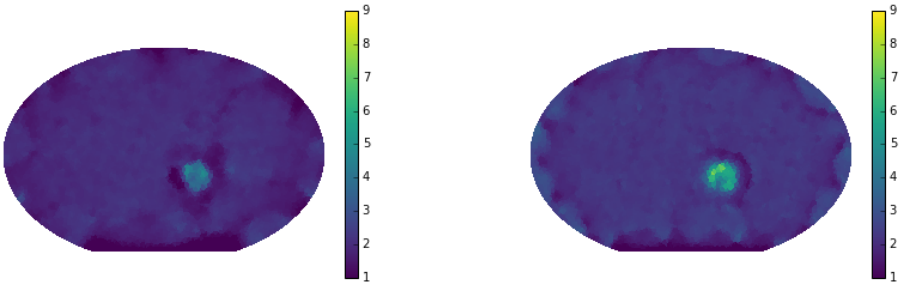

(a) (b)

Figure 3.24: AIDE estimates using 5 frequencies (a) frequencies around 20 Hz, (b) optimal design.

3.6 Modeling the Glucose-Insulin dynamics during OGTT

Carbohydrates are one of the main nutrients of humans. The body breaks down carbohydrates into glucose. Most tissues and organs need glucose constantly as an important source of energy. The process of maintaining blood glucose at a steady-state level is called glucose homeostasis [121]. This state is constantly perturbed throughout the day by food ingestion, fasting, physical activity, or exercise. A low blood concentration of glucose can causes seizures, loss of

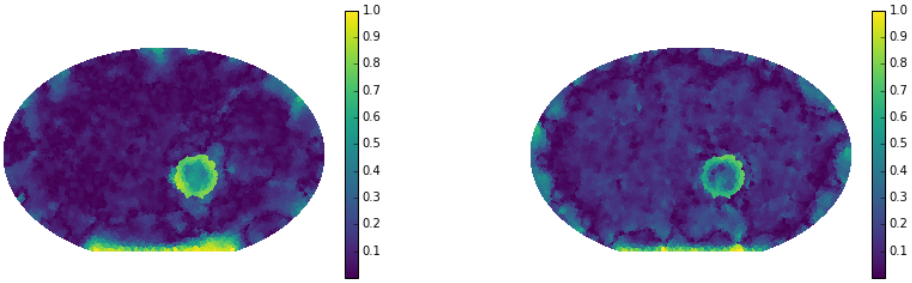

(a) (b)

Figure 3.25: Relative error of the AIDE estimates using 5 frequencies (a) frequencies around 20 Hz (L^2 error $= 208.04$), (b) optimal design (L^2 error $= 170.92$).

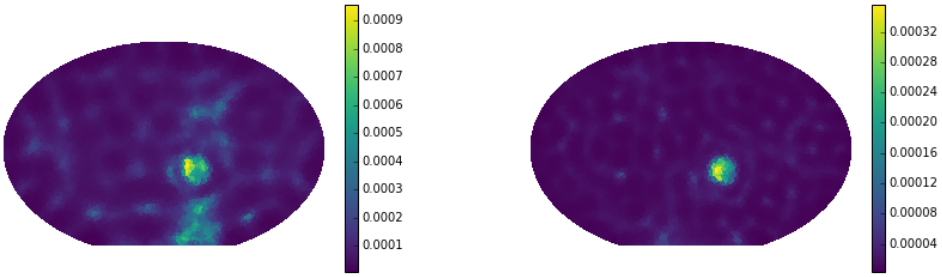

(a) (b)

Figure 3.26: Variances of the AIDE estimates using 5 frequencies (a) frequencies around 20 Hz (Trace $= 0.60$), (b) optimal design (Trace $= 0.11$).

consciousness, or even death. On the other hand, the long-lasting elevation of blood glucose concentrations can result in blindness, renal failure, vascular disease, and neuropathy. Therefore, blood glucose concentration needs to be maintained within narrow limits. Blood glucose level is regulated by two main hormones secreted by the pancreas: insulin and glucagon. The World Health Organization (WHO) refers to diabetes as a chronic and metabolic disease characterized by elevated levels of blood glucose. The most common is type 2 diabetes, usually in adults, which occurs when the body becomes resistant to insulin or does not make enough insulin. One common test for diabetes

diagnosis is the Oral Glucose Tolerance Test (OGTT). In this procedure, the patient must arrive with eight-hour fasting and take a sugary drink. Several blood samples are taken over the process, the first before consuming the drink, the others to observe the body's reaction to the oral stimulus. A prediabetic state is characterized by an impaired fasting glucose level (IFG), an impaired blood glucose level at two hours after consuming the drink, named by impaired glucose tolerance (IGT), or both. This diagnostic process is characterized by uncertainties along the test [122] as the amount of glucose absorbed and its absorption rate. A popular approach to describe glucose dynamics is by compartmental models, [123, 124]. The inference of model parameters from glucose observations may be described as an inverse problem. Predictions obtained from inferences processes must be reliable due to several error sources as a simplification of biological process in the modeling, numerical implementation, and measurement errors. The Bayesian paradigm allows producing predictions with quantified uncertainties. Under this approach, the solution of the inverse problem is a probability distribution for the parameter of interest [45] which describes multiple consistent scenarios to fit the data. In this work, we follow this statistical approach to model the inference process on OGTT data, where the regressor comes from an ODE system that describes the glucose dynamics. We model insulin and glucagon secretion originated from blood glucose concentration. Also, we consider delays and hormonal effects from the gastrointestinal tract. We model reactions of the body to the sugary drink by a gamma distribution.

Related Work Describing the glucose dynamics by compartmental models is very common, see [123, 124] for reviews. Usually, the level of description is related to the important features of the dynamic involved in the diagnostic test implemented. For the Oral Glucose Tolerance Test, one of the main effects to be modeled is the process in the gastrointestinal tract [125, 121, 122]. Most of the models include the insulin effect on the glucose homeostasis process. Glucagon action is less popular to include. The process in the gastrointestinal tract has become important in the last years. Incretins are hormones secreted by the gut which stimulate insulin secretion before blood glucose level increases. This

effect is reduced or even vanished for type 2 diabetes patients, see [126, 127]. Reactions of the body to the rise of the glucose level comes with a delay which may be model by explicit delays in time [128, 129], or by extra compartments in the dynamical system [122, 130, 131]. In epidemiology, usually latency and infections periods are describe by an exponential distribution. Authors in [132] argued the inadequacy of this distribution since this proposal overestimates shorter and longer durations of the phenomenon in the period. More realistic distributions may be described by a gamma distribution. This can be obtained by subdivide the compartment into n stages. Specifically, the distribution obtained is an Erlang distribution, which is a gamma distribution with a shape integer parameter [133]. Bayesian approaches for estimate parameters of compartmental models were proposed in [131, 134, 135]. Authors in [135] proposed a minimal model for glucose-insulin dynamics. Their classification parameters have not biological meaning. Authors in [134] proposed a Bayesian experimental design for the time at which samples are collected.

Contributions The main contributions of this work are: (i) Insulin secretion is modeled with two possible sources of stimulation: direct glucose rise and incretin hormones. Incretin effect has a major role in insulin secretion when the body suffers an oral stimulus. Separately, these two sources allows us to propose a classification between patients. These parameters may suggested possible alterations in healthy patients. (ii) Delays of the body in the gastrointestinal tract and the endocrine system are model by a gamma distribution. We introduce Erlang distributed periods in the hormonal dynamics for incretin, insulin and glucagon.

Limitations We remark some limitations for this approach: (i) Since the glucagon dynamics turns on when the glucose level is lower than the basal level, for patients with measurements greater than this basal level we do not have information about the parameter corresponding to this reaction. The consequence is that the posterior marginal for θ_2 matches the prior marginal. This situation may be circumvent by monitoring the glucose level during more than two hours. (ii) The classification proposed is based on two parameters.

Each is the product of two quantities with biological meaning. Nevertheless, we can not recover each action separately. Adding insulin data in the inference may allow recover each action parameter.

The rest of this report is organized as follows. In Section 3.6.1 we present the ODE system that describes the biological situation for the glucose dynamics during OGTT. This section is followed by the description of the Bayesian inference problem in Section 3.6.2. Our numerical results are present in Section 3.6.3. Finally we discuss our results and findings in Section 3.6.4.

3.6.1 Forward Modeling

In this section we describe the biological situation in detail to justify our approach. The biological modeling on which we rely is given by the following ODE system

$$\dot{G} = \lambda_1 L - \lambda_2 I + \lambda_3 V \tag{3.70}$$

$$\dot{I} = \lambda_4 (G - G_b)^+ + \lambda_8 V - \lambda_5 I \tag{3.71}$$

$$\dot{L} = \lambda_6 (G_b - G)^+ - \lambda_7 L \tag{3.72}$$

$$\dot{V} = -\lambda_3 V \tag{3.73}$$

where G denotes the glucose blood level, I the insulin level, L the glucagon level, and V the glucose from the sugary drink in the gastrointestinal tract. Equation 3.70 models the dynamics of the glucose which decreases proportional to the insulin level and increases according to two sources, first by the glucose of the sugary drink from the intestinal tract, second by the glucagon action. λ_1 and λ_2 are efficacy rates for the glucagon and the insulin. The dynamics of insulin and glucagon are very similar and depends on the basal glucose level of the body. The pancreas secretes insulin when the blood glucose level is higher than the basal glucose level on the body. Conversely, secretes glucagon when the blood glucose level is lower than the basal glucose level on the body. We model this secretion action by a switch on the quantity $G - G_b$. Mathematically speaking, we use the positive part of $G - G_b$, denoted by $(G - G_b)^+$, to model

the secretion of insulin, conversely $(G_b - G)^+$ to the secretion of glucagon. λ_4 and λ_6 are secretion rates for the insulin and the glucagon and λ_5 and λ_7 are its disintegration rates. In addition to the insulin dynamics, hormones from the gut play a main role in the insulin secretion on the oral glucose consumption. The second term on equation (3.71) mimics the secretion due to these hormones, the incretin effect. Incretin effect is reduced or even vanished in diabetic patiens, [127, 126]. Therefore, insulin secretion may be due by the glucose stimulation and/or the incretin effect. Model defined by equations (3.70)- (3.73) has 8 parameters. Parameters λ_5 and λ_7 will be taken from the literature. For the other 6 parameters, we will face an identifiability problem, that is, the structure of the model may lead to inference problems related to the uniquely estimation of parameters. To face this problem, we introduce scaled version of insulin and glucagon. Note that by multiplying equation 3.71 by a constant, we obtain a scaled insulin

$$\lambda_I \dot{I} = \lambda_I \lambda_4 (G - G_b)^+ + \lambda_I \lambda_8 V - \lambda_I \lambda_5 I \tag{3.74}$$

If we name $I_s = \lambda_I I$, we have $\dot{I}_s = (\dot{\lambda_I I}) = \lambda_I \dot{I}$. By substituying in equation 3.74, we obtain

$$\dot{I}_s = \theta (G - G_b)^+ + \gamma V - \lambda_5 I_s \tag{3.75}$$

We will apply this idea to obtain a scaled insulin and glucagon by multiplying equation 3.71 by λ_2 and equation 3.72 by λ_1. Finally we obtain the system

$$\dot{G} = L_1 - I_1 + \lambda_3 V \tag{3.76}$$

$$\dot{I}_1 = \theta_1 (G - G_b)^+ + \theta_3 V - \lambda_5 I_1 \tag{3.77}$$

$$\dot{L}_1 = \theta_2 (G_b - G)^+ - \lambda_7 L_1 \tag{3.78}$$

$$\dot{V} = -\lambda_3 V \tag{3.79}$$

where $L_1 = \lambda_1 L, I_1 = \lambda_2 I, \theta_1 = \lambda_2 \lambda_4, \theta_3 = \lambda_2 \lambda_8$ and $\theta_2 = \lambda_1 \lambda_6$. Note that these substitutions allow us to decrease the number of parameters in the system which will be useful in the inference to fight the identifiability problem. Finally, note that this model is centered around the value G_b, which tipically take values in the range $[75, 100]$.

In addition, we would like to address the possible delays of the body

reaction. To introduce explicit delays in time in the ODE system is very common [128, 129]. The same effect may be obtained by introducing extra compartments. In epidemiology, these extra compartments model aspects as latency and infection periods with a more realistic distribution. This technique is known as an Erlang model, [133, 136, 137, 132]. Typically, the exponential distribution is used. Nevertheless, the exponential distribution overestimates the number of individuals whose duration of infection is shorter or longer than the mean [132]. In a classical SEIR compartment model, this approach subdivides stage I (and/or E) into identical substages. This modeling matches the renewal approach [133], which considers the cohorts of infectious(exposed) individuals while the ODE approach considers each infectious(exposed) individual. In this work we consider the same idea to model hormonal behavior during the OGTT test. We propose a modification of the model in [36], deduced before in equations (3.76)-(3.79). This modification is given by

$$\dot{G} = L_m - I_n + \theta_0 V_s \tag{3.80}$$

$$\dot{I}_1 = \theta_1 (G - G_b)^+ + \theta_3 V_s - n\sigma_I I_1 \tag{3.81}$$

$$\dot{I}_i = n\sigma_I I_{i-1} - n\sigma_I I_i, \qquad i = 2, \ldots, n \tag{3.82}$$

$$\dot{L}_1 = \theta_2 (G_b - G)^+ - m\sigma_L L_1 \tag{3.83}$$

$$\dot{L}_j = m\sigma_L L_{j-1} - m\sigma_L L_j, \qquad j = 2, \ldots, m \tag{3.84}$$

$$\dot{V}_1 = -s\theta_0 V_1 \tag{3.85}$$

$$\dot{V}_k = s\theta_0 V_{k-1} - s\theta_0 V_k, \qquad k = 2, \ldots s \tag{3.86}$$

We propose $n = m = s = 2$. After ingestion, glucose is absorbed in the upper gastrointestinal tract, transported to the liver, and finally reaches the peripheral circulation [138]. Introducing a second compartment for V allows us to model this behavior of glucose due to the sugary drink in the digestive system as in [131, 139]. Second compartments for I and L allow us to model the delays due to the pancreas reaction as in [128]. These delays are a consequence of recurrent inhibitory dynamics [140, 141]. In recurrent inhibition, we can see how the activation of a quantity produces excitation in a second quantity that inhibits the activity of the first. This phenomenon is present in the dynamics

of glucose-insulin-glucagon. The specific case for glucose-insulin dynamics is known as a negative feedback loop [142]. In the next subsection, we propose a regressor from the dynamical system in equations (3.80)-(3.86) to fit the glucose data provided by the application of the OGTT. The inference process follows a Bayesian approach.

3.6.2 Bayesian Formulation for the Inference Problem

In this section, we consider the inverse problem of determining the posterior distribution for the parameter $\Theta = (\theta_0, \theta_1, \theta_2, G_b, \theta_3)$. Under the Bayesian approach, the solution of the inverse problem is a probability distribution conditioned on the information of the data. We have glucose measurements at five times $t_i = 0.0, 0.5, 1.0, 1.5$ and 2.0 hours. We assume that the data $\mathbf{y}$ follow the noise model

$$\mathbf{y}_i = \mathcal{G}(\Theta)_i + \eta_i \tag{3.87}$$

where $\mathcal{G}(\Theta)_i = G(t_i, \Theta)$ and G is the solution for the glucose on the ODE system given in equation (3.80) and $\eta_i \sim \mathcal{N}(0, \sigma^2)$. The parameters σ_I, σ_L and σ are determined from previous works [131, 139].
Our prior knowledge about the parameters are that $\theta_i > 0$ and the basal level of glucose is in the range of 75 and 100. We assumed independence on the prior parameters, that is

$$\pi_0(\Theta) = \pi_0^0(\theta_0)\pi_0^1(\theta_1)\pi_0^2(\theta_2)\pi_0^3(G_b)\pi_0^4(\theta_3) \tag{3.88}$$

We propose gamma distribution for each parameter. Le us recall that if $Z \sim \Gamma(\alpha, \beta)$ then $\mathbb{E}[Z] = \alpha/\beta$ and $\mathbb{V}ar[Z] = \alpha/\beta^2$. Our priors proposal are given by:

$$\begin{aligned}
\theta_0 &\sim \Gamma(2, 1) \\
\theta_1 &\sim \Gamma(10, 1) \\
\theta_2 &\sim \Gamma(10, 1) \\
\theta_3 &\sim \Gamma(10, 1) \\
G_b &\sim \Gamma(90^2/20, 90/20).
\end{aligned} \tag{3.89}$$

The prior distribution for the parameter θ_0 corresponding to the gastrointestinal dynamic is truncated. From simulations, we propose values greater than 0.5 to avoid almost constant trajectories for the glucose. Having the likelihood and the prior, and since we are working in finite dimensions, Bayes theorem ensures the posterior distribution existence $\pi(\Theta|\mathbf{y})$. To generate samples, we used the t-walk [65]. We perform 10000 iterations for each patient with a burnin of 1000. We show our results in the next subsection.

3.6.3 Numerical Results

In this subsection, we show the results of the inference. We perform a MCMC using t-walk for 80 patients classified at follows:

1. 51 healthy patients (H).
2. 4 patients with Impaired Fasting Glucose (IFG): Fasting blood glucose level ≥ 100.
3. 15 patients with Impaired Glucose Tolerance (IGT): Blood glucose level ≥ 140 at $t = 2$.
4. 7 patients with IFG and IGT (BA: both alterations).
5. 3 patients with Diabetes Mellitus 2 (DM2): Fasting blood glucose level ≥ 126 and blood glucose level ≥ 200 at $t = 2$.

In Figure 3.27 (a) we show the fitting to the data for several estimators as the posterior mean, the posterior median, and the maximum a posteriori (MAP) for a patient with oscillatory data. We show the corresponding trajectories for the digestive compartment V_2 in Figure 3.27 (b), scaled insulin compartment I_2 in (c), and scaled glucagon compartment L_2 in (d). In Figures 3.28-3.29 we show the fitting to the glucose data and the uncertainty associated with healthy and non-healthy patient respectively.

From the information of the inference, we would like to explore the values of the parameters that describe different situations on patients. In Figure 3.30 (a) we show chain values for five different scenarios. The corresponding glucose

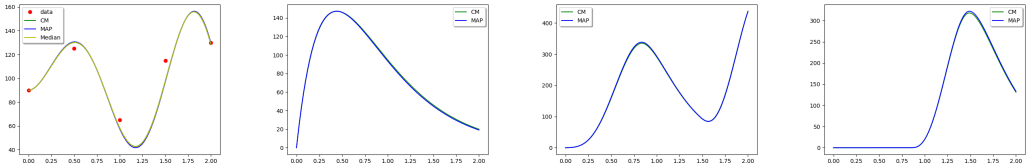

(a) (b) (c) (d)

Figure 3.27: (a) Glucose level and fit to data for some estimators, (b) digestive compartment V_2, (c) scaled insulin compartment I_2, (d) scaled glucagon compartmentL_2.

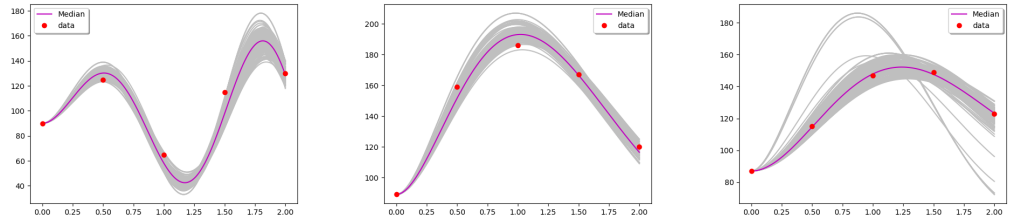

(a) (b) (c)

Figure 3.28: Fit to data and uncertainty in healthy patients.

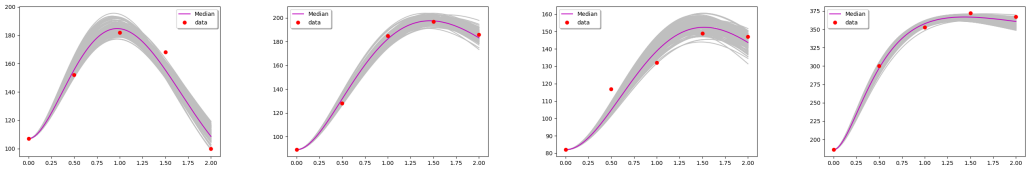

(a) (b) (c) (d)

Figure 3.29: Fit to data and uncertainty in unhealthy patients. (a) Patient with IFG, (b) Patient with IGT, (c) Patient with IGT, (d) Diabetic patient.

measurements are shown in Figure 3.30 (b). Note that parameters θ_1 and θ_3 allow us to recognize low secretion insulin levels. The gastric emptying parameter θ_0 allows us to recognize the initial slope during the test. Two patients with low gastrointestinal emptying labeled as impaired2 and diabetic2 present higher values close to two hours instead of at the beginning.

In Figure 3.31 (a), we show the values of the MAP estimate for parameters θ_1 and θ_3 inferred. We plotted $1/\theta_3$ against $1/\theta_1$. A high value for $1/\theta_1$ may

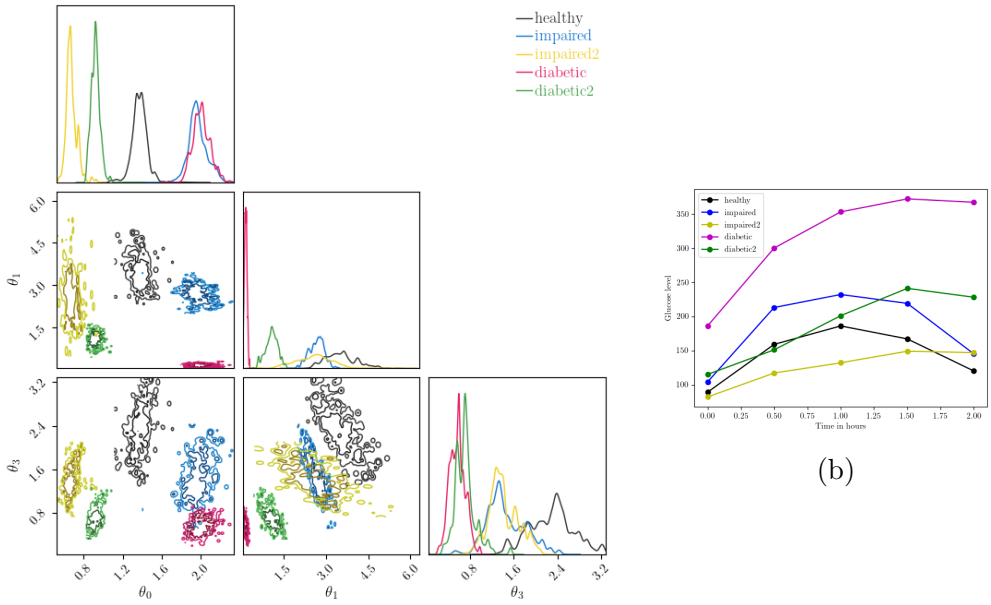

(a) (b)

Figure 3.30: (a) Chain values for parameters θ_0, θ_1, and θ_3 for two diabetic patients, two patients with impaired Glucose Tolerance and a Healthy patient. Gastric emptying parameter θ_0 allow us to recognize initial slope during the test. (b) Glucose level measurements from patients in (a).

be produced by a high glucose level at time 30 minutes whilst a high value for $1/\theta_3$ may be produced by a high glucose level at time 1 hour and 30 minutes. Patients diagnosed with IFG are considered healthy in the classification based on insulin secretion indicators. In Figure 3.31 (b)-(c), we show the results from a k-means performed using the package scikit-learn in python [**?**]. The idea behind this method is to identify possible clusters of data in a database. We are interested in determine three centroids see Figure 3.31 (b). The labeling proposed by the algorithm classifies into three groups shown in Figure 3.31 (c). Note that the results match a possible classification based on θ_3 values.

3.6.4 Discussion and conclusions

In this work, we propose a Bayesian approach to analyze OGTT data. The modeling includes two insulin indicators, one related to blood level glucose,

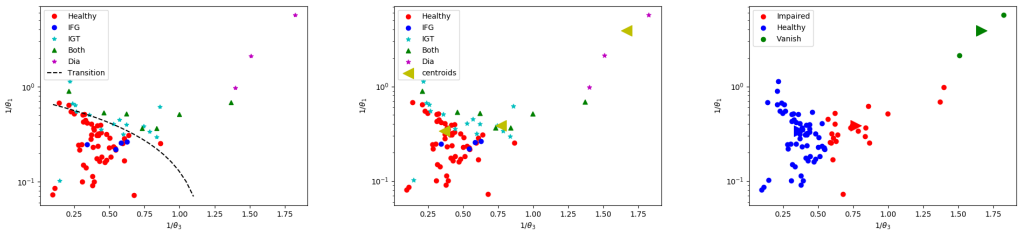

(a) (b) (c)

Figure 3.31: (a) Plot $1/\theta_3$ against $1/\theta_1$ for the MAP estimate values. (b) Centroids computed by the clustering method of kmeans, (c) Labeling generate from the clustering process.

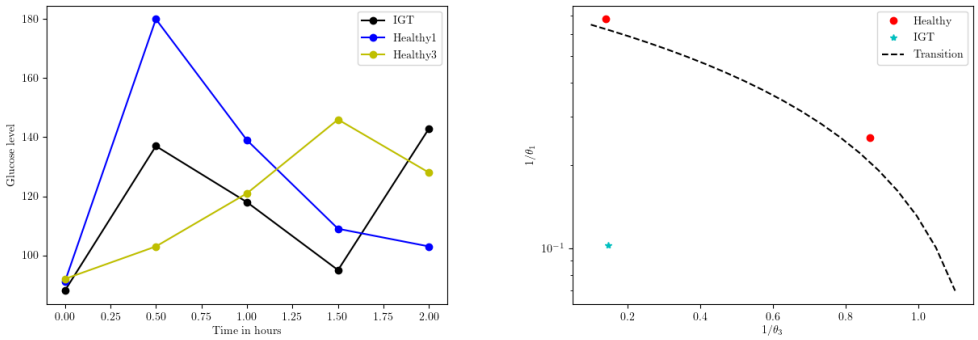

(a) (b)

Figure 3.32: Discussion: (a) Data from three patients, (b) Classification according to insulin indicator θ_1 and θ_3 values at the MAP. Patient diagnose with IGT has an impaired value of the glucose at $t = 2$ because of its glucagon secretion effect. Indicators of insulin secretion take values inside the healthy zone. Two patients diagnose as healthy are close of the transition limit due to a small value of one of the insulin indicators.

the other with the glucose level in the gastrointestinal tract. These indicators describe insulin dynamics due to oral stimulus. A possible classification for patients is described in Figure 3.31 (a). Now, we discuss its scope and limitations. Patients diagnosed with IFG have an impaired value at fasting state and unimpaired values at two hours. Their insulin indicators classify these patients as healthy because their situation is not a consequence of the oral stimulus. A patient with IGT may have normal values for its insulin

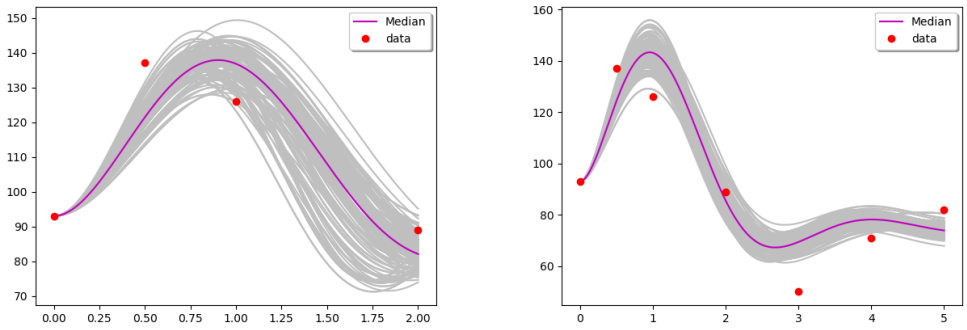

(a) (b)

Figure 3.33: Data from a healthy patient and fit glucose trajectories (a) during two hours, (b) during five hours. In the inference performed in (a), glucagon indicator is hardly recognize due to his action starts close of the two hours. Having more time monitoring glucose levels may allow to have a reliable inference about its value.

indicators as shown in Figure 3.32. From its glucose values, we can deduce that its situation is a consequence of impaired glucagon secretion. This anomaly will not be detected by the insulin indicators. To recognize this situation, the parameter θ_2 may provide information. As we discussed before, this parameter is not identifiable for all patients with their glucose values greater than the basal glucose level. Have measurements for more than two hours could solve the identifiability situation as we exemplify in Figure 3.33. Finally, the classification places some healthy patients close to the transition zone. This situation may be a consequence of a high glucose level at 30 minutes, for θ_1, or at 1 hour and 30 minutes for θ_3, see Figure 3.32 (a). This may be the beginning of an anomaly which may be confirmed if patients stay under control and follow up for several months or years. From our results, it seems to us that the classification in healthy, IFG, IGT, IFG-IGT, and T2D could be modified to recognize more specific details about the cause of an impaired condition. Future work contemplates how to adapt the model to incorporate insulin data. It is well known that the human body has a basal level of insulin and that insulin secretion follows pulsating patterns which represent new challenges in our modeling and the respective uncertainty quantification.

3.7 Modeling the transmission dynamics for the COVID-19 epidemic outbreak

In this subsection, we show the results on the inference of the transmission rates in a dynamical system that models the dynamics of COVID-19 in México. This model was presented in [143]. Under some assumptions, we formulate the Bayesian inverse problem for two parameters: the transmission rate from infected individuals and the transmission from the environment.

3.7.1 Forward Model

Based on the clinical progression of the disease, we propose a deterministic compartmental epidemic model under the *SEIR* structure as in [144, 145, 146]. One important aspect of our model is that, in addition to human-to-human transmission, we consider the indirect infections caused by contact with a contaminated environment.

For our model formulation, we divide the total human population (denoted N) into five compartments: susceptible individuals (denoted S), exposed/latent individuals (denoted E), infectious asymptomatic individuals (denoted A), infectious with symptoms (denoted I), and recovered (denoted R). Finally, we consider a compartment for the free-living COVID-19 in the environment (denoted V).

For our model formulation, we consider a short time horizon in which the total human population is relatively fixed. Therefore, demographic dynamics are not considered in the model. The susceptible population S can acquire the infection when they come in contact with asymptomatic A and symptomatic I infectious individuals at rates β_A and β_I, respectively. They also can be infected by contact with contaminated surfaces with coronavirus at a rate β_V. A proportion p of the exposed individuals E will transition to the symptomatic infectious class I at a rate σ, while the other proportion $1-p$ will enter the asymptomatic infectious class A. The recovery rates for individuals in classes A, I are γ_A, γ_I, respectively. These individuals gain permanent immunity and move to the recovered class R. However, individuals in the symptomatic infectious

class I can die due to the disease at a rate μ. Asymptomatic and symptomatic infected individuals release the virus into the environment with shedding rates c_1 and c_2, respectively as presented in [147]. Hence, the free-living virus in the environment grows with a factor $c_1A + c_2I$. The parameter μ_V represents the mortality rate of the free-living virus in the environment.

These assumptions lead to the following system of differential equations:

$$\begin{aligned}
\dot{S} &= -\lambda S, \\
\dot{E} &= \lambda S - \sigma E, \\
\dot{A} &= (1-p)\sigma E - \gamma_A A, \\
\dot{I} &= p\sigma E - \gamma_I I - \mu I, \\
\dot{R} &= \gamma_A A + \gamma_I I, \\
\dot{V} &= c_1 A + c_2 I - \mu_V V,
\end{aligned} \tag{3.90}$$

where $\lambda = \beta_A A + \beta_I I + \beta_V V$ is the force of the infection.

According to the WHO, the SARS-CoV-2 is primarily transmitted between people through respiratory droplets and contact routes. Droplet transmission occurs when a person is in close contact (within 1 m) with an infectious individual and is therefore at risk of having his mouth, nose, or eyes exposed to potentially infectious respiratory droplets [148]. The parameters β_k $(k = A, I)$ model this direct person-to-person transmission and are of the form $\beta_k = b_k\phi_k$, where b_k is the average number of contacts per person per unit of time and ϕ_k is the probability of successful infection given a contact. For example, $\beta_A = b_A\phi_A$, where b_A is the average number of close contacts in which a susceptible is exposed to respiratory droplets produced when an asymptomatic infected person coughs, sneezes or talks, and ϕ_A is the probability of successful infection given this contact. Since the virus can survive on inanimate surfaces [149], the transmission may also occur through contaminated fomites. The parameter β_V models these indirect infections caused by touching an object or surface contaminated (due to an infected person) with the virus. Therefore, $\beta_V = b_V\phi_V$, where b_V is the average number of times a susceptible person touches a surface contaminated with SARS-CoV-2, and ϕ_V is the probability of infection given this contact. The parameters $c_i \geq 0$ $(i = 1, 2)$ measure the

number of virus particles released through respiratory droplets produced per infected individual (during coughs or sneezes) that remain alive and infectious on surfaces or objects per unit of time.

From results in [143], we know that the basic reproduction number is given by

$$\mathcal{R}_0 = \left[\left(\frac{\beta_A}{\gamma_A} + \frac{c_1 \beta_V}{\mu_V \gamma_A} \right) (1-p) + \left(\frac{\beta_I}{\gamma_I + \mu} + \frac{c_2 \beta_V}{\mu_V (\mu + \gamma_I)} \right) p \right] S_0. \tag{3.91}$$

which can be divide in two main contribution channels from the symptomatic and the asymtomatic infected. The basic reproduction number (3.91) is the weighted sum of the terms T_A and T_I, that is,

$$\mathcal{R}_0 = (1-p) T_A + p T_I \tag{3.92}$$

where

$$T_A = \left(\beta_A + c_1 \frac{\beta_V}{\mu_V} \right) \frac{S_0}{\gamma_A} \tag{3.93}$$

measure the contribution of asymptomatic infectious individuals to the production of new infections, and

$$T_I = \left(\beta_I + c_2 \frac{\beta_V}{\mu_V} \right) \frac{S_0}{\gamma_I + \mu} \tag{3.94}$$

is the contribution of symptomatic infectious individuals to the production of new infections. Note that both terms take account the environment-to-human transmission route for virus.

3.7.2 Parameter Estimates and Bayesian Inference

The compartmental epidemic model (3.90) for the transmission dynamics of SARS-CoV-2 has 11 parameters. First, we gather some parameter values from the literature. Next, we estimate those parameters that are not found in the literature or that depend on the population under study. We assume the time unit is days and estimate the parameters as follows.

(i) *Recovery rates.* The estimated mean value for the recovery rates γ_A, γ_I,

for asymptomatic and symptomatic infectious individuals, respectively, have been estimated to be $\gamma_A = 0.13978$ and $\gamma_I = 0.33029$ [150].

(ii) *Mean incubation period.* The mean incubation period $(1/\sigma)$ for coronavirus infection has been estimated to be 6.4 days, ranging from 2.1 to 11.1 days [151]. Therefore, we assume $\sigma = 1/6.4$.

(iii) *Fraction of individuals which develop symptoms.* The probability of having symptoms after the infection has been estimated to be $p = 0.868343$ [150].

(iv) *Mortality rate of coronavirus in the environment.* Some studies have estimated that coronaviruses can remain infectious on inanimate surfaces at room temperature from a few hours up to 9 days [149]. Here, we assume an average survival rate of 1 day which implies $\mu_V = 1$.

(v) *Disease induced death rate.* The estimated mean value for the disease induced death rate is $\mu = 1.7826 \times 10^{-5}$ [150].

The rest of the parameters, that is, the transmission rates β_A, β_I, and β_V, in addition to the shedding rates c_1 and c_2, were estimated using Bayesian inference in [143]. From a Sobol sensitivity analysis, performed in Salib [152], we can see in Figure (3.34) that indices corresponding to c_i are null. Here, we assume $c_1 = \dfrac{c_2}{2}$ as in [153] and consider a fix value for c_1. Finally, since the $\beta' s$ rates depend highly on population-level characteristics, we make inference in β_I and β_V, assuming that $\beta_A = 2\beta_I$ based on results in [143]. We consider data corresponding to the daily cumulative cases of infected individuals in Mexico. The data were obtained from the daily report of the Mexican Secretaria of Health from March 11, 2020, to March 25, 2020 [154]. It is important to remark that this data corresponds to the confirmed cases; therefore, it is highly possible that the real epidemic curve is higher than the total infected cases presented in the data. In other words, since in México there is not massive testing, the initial data on the confirmed cases from the pandemic corresponds to symptomatic infections. Therefore, as an attempt to avoid estimates biased down, we fit the data using only the individuals in the symptomatic infectious class, I, without considering the asymptomatic infectious class A. We assume

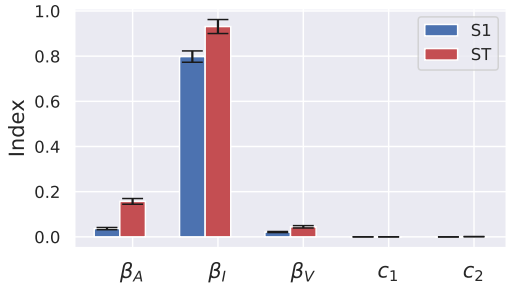

Figure 3.34: First ($S1$) and total order (ST) Sobol indices of the cumulative cases $C(t_i; \mathbf{x})$ built from the solution I of model (3.90) with respect to the parameters $\mathbf{x} = (\beta_A, \beta_I, \beta_V, c_1, c_2)$. We perform this analysis for several time values t_i and found that the results do not depend on t_i. The indices for the variables c_i $(i = 1, 2)$ are null.

the following model for the data y_i

$$y_i \sim \text{Poisson}\left(\mathcal{I}_j(\mathbf{x})\right), \qquad i = 0, \ldots, 14 \tag{3.95}$$

where $\mathcal{I}_j(\mathbf{x})$ denote the predicted number of new cases between times $j-1$ and j, see [155]. For the case of our model,

$$\mathcal{I}_j(\mathbf{x}) = \int_{t_{j-1}}^{t_j} p\sigma E(\mathbf{x}) dt \tag{3.96}$$

with E the exposed individuals given by the ODE's system at time t_i and $\mathbf{x} = (\beta_I, \beta_V)$ the vector of parameters to estimate. By assuming independence on the observations, the likelihood function $\mathcal{L}(\mathbf{x})$ satisfies:

$$\mathcal{L}(\mathbf{x}) \propto \prod_{j=1}^{j=14} \frac{e^{-\mathcal{I}_j(\mathbf{x})}(\mathcal{I}_j(\mathbf{x}))^{y_j}}{y_j!}. \tag{3.97}$$

The following values were taken as initial conditions: the initial total population was taken as the approximate Mexican population at the year 2020, i.e., $N(0) = 128,000,000$; the initially symptomatic infectious individuals as $I(0) = 4$, which is equal to the initial number of confirmed cases in the data. No recovered individuals are considered at the initial time, thus $R(0) = 0$. Finally, we

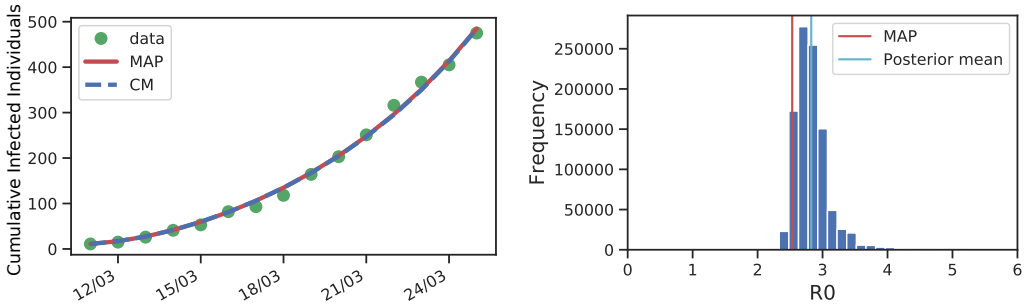

(a) (b)

Figure 3.35: **(a)** Data per date and fitted curves for the cumulative infected individuals for the MAP estimate and posterior mean. **(b)** Estimation of $\mathcal{R}_0$ for the samples of the MCMC. The value of $\mathcal{R}_0$ for the MAP estimate is 2.5 and for the posterior mean estimate is 2.7.

assumed $E(0) = 4$, $A(0) = 1$, $V(0) = 10$, and $S(0) = N(0) - E(0) - A(0) - I(0)$.

Moreover, we define by $\pi_0(\mathbf{x})$ the prior distribution for $\mathbf{x}$. We assume independence of the parameters, hence

$$\pi_0(\mathbf{x}) = \pi_1(\beta_I)\pi_2(\beta_V). \tag{3.98}$$

Since we are using mass action incidence, we can expect to have values of β_j ($j = I, V$) around the negative order of the initial susceptible population. Hence, we propose a Gamma distribution for β_A with mean 10^{-8}. Recall that the gamma distribution is denoted by $\Gamma(\alpha, \beta)$ with α the shape parameter and β the inverse scale parameter. If $Z \sim \Gamma(\alpha, \beta)$ then $\mathbb{E}[Z] = \alpha/\beta$ and $\mathbb{V}ar[Z] = \alpha/\beta^2$. We propose

$$\begin{aligned} \beta_I &\sim \Gamma(10^{-8}, 1) \\ \beta_V &\sim \Gamma(10^{-8}, 1). \end{aligned} \tag{3.99}$$

To sampling from the posterior, we run a Markov Chain Monte Carlo (MCMC) using twalk, introduced in [65]. We consider the time in days and $t_0 = 0$ for the first data on March 11. We run a MCMC for 100000 samples with 10000 of burnin. The posterior distribution for each parameter are shown in Fig. (3.36).

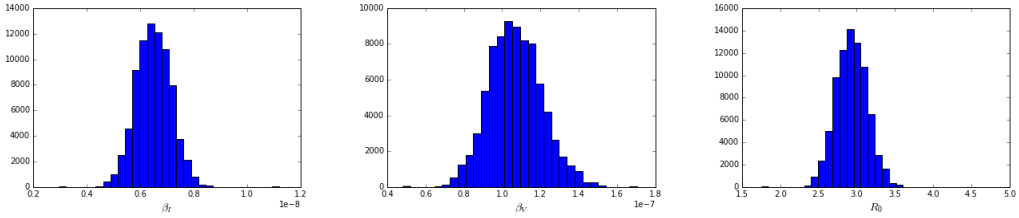

Figure 3.36: Marginal posteriors for the parameters (a) β_I and (b) β_V. (c) Frequency distribution for $\mathcal{R}_0$ from the Monte Carlo samples.

Parameter	MAP estimate	Posterior mean
β_I	6.69×10^{-9}	4.52×10^{-9}
β_V	4.73×10^{-8}	4.88×10^{-8}

Table 3.4: Bayesian estimators

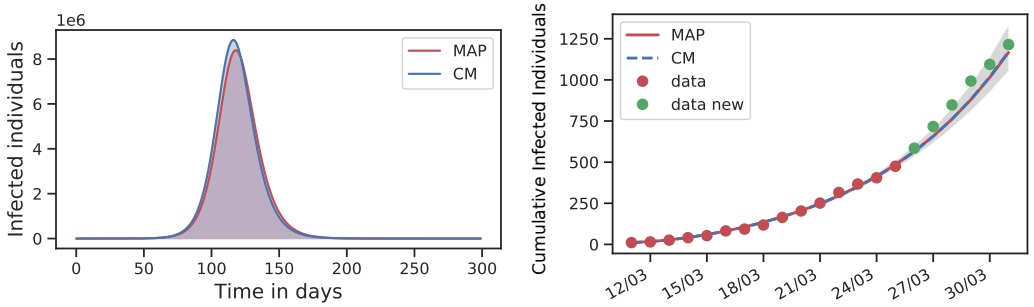

(a) (b)

Figure 3.37: **(a)** Infectious symptomatic individuals $I(t)$ corresponding to the MAP (red) and the posterior mean estimates (blue). **(b)** Red dots show the data of cumulative confirmed cases of COVID-19 in Mexico from March 11, 2020, to March 25, 2020. The gray area shows the uncertainty with the last 25000 samples of the chain. The green dots represent data from march 26 to march 31 that were not used in the inference.

The posterior distribution obtained allow us to compute posterior predictive marginals for future data (after March 25). The probability of a future observation $\mathbf{z}$ given the data y is $p(\mathbf{z}|y)$ and can be computed as follows

$$p(\mathbf{z}|y) = \int_{\mathbb{X}} p(\mathbf{z}|\mathbf{x})p(\mathbf{x}|y)d\mathbf{x} \tag{3.100}$$

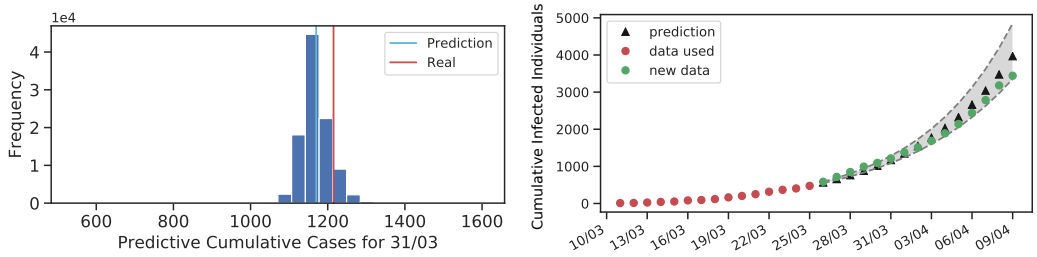

(a) (b)

Figure 3.38: **(a)** Posterior predictive marginal for the total cumulative infections on March 31. **(b)** Red dots show the data of cumulative confirmed cases of COVID-19 in Mexico from March 11, 2020, to March 25, 2020, used for the inference. In black we present our predicted values, in green the data from March 26 to April 9 not used in the inference, and the dashed lines show the interval with 98 percent of the mass for the predictive marginal.

where $\mathbf{x}$ denotes our vector of parameters. Figure 3.38 (a) shows the predictive posterior marginal for the total cumulative infections on March 31. Figure 3.38 (b) shows a comparison between the predicted values for the cumulative number of infections and the officially published data from March 26 to April 9. The dashed lines represent the interval with 98 percent of the mass for the predictive marginal.

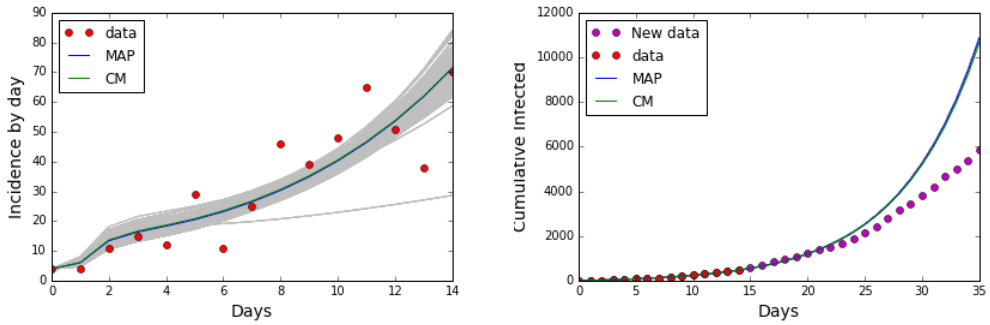

Figure 3.39: (a) Incidence data fit from Monte Carlo samples (b) Cumulative data fit from Monte Carlo samples.

3.8 Achieving convergence rates with accelerated methods

Consider the problem of

$$\min f(x) \tag{3.101}$$

where f is a convex function with $x \in \mathbb{R}^n$. First-order methods had become very popular in the machine learning community. The phenomenon named acceleration has been a topic of theoretical and computational research. As we mentioned before, authors in [106] derived a second-order ODE which is the exact limit of Nesterov's scheme. From a variational perspective, we can start with a continuous-time equation and propose a discretization. We can obtain several discretizations from the same second-order ODE. Of course, the aim is to find a discretization that preserves theoretical properties as the convergence rates. The aim of this section is to show numerical results about discretizations that preserve continuous convergence rates.

3.8.1 Discretization from the continuous time equation

In this subsection, we show a discretization from a continuous time equation. Consider the Hamiltonian

$$\mathcal{H}(P, X, S, t) = \frac{e^{2\alpha}}{2} \|P\|^2 + e^{\beta} f(X) + (e^{\alpha} + \dot{\alpha})\, S \tag{3.102}$$

where α, β and γ satisfies

$$\alpha = \log p - \log t \tag{3.103}$$

$$\beta = p \log t + \log C \tag{3.104}$$

$$\gamma = p \log t \tag{3.105}$$

are functions proposed in [113] to achieve convergence rate of $\mathcal{O}(t^{-p})$. Note that the optimal scaling conditions in equations (2.111) are satisfied. From lemma

2.7.1, we deduce the following contact system

$$\dot{X} = e^{2\alpha} P \tag{3.106}$$

$$\dot{P} = -e^{\beta} \nabla_X f(X) - P\left(e^{\alpha} + \dot{\alpha}\right) \tag{3.107}$$

$$\dot{S} = \frac{e^{2\alpha}}{2} \|P\|^2 - e^{\beta} f(X) - \left(e^{\alpha} + \dot{\alpha}\right) S\,. \tag{3.108}$$

In [112], authors propose a splitting method applied to this Hamiltonian. This ODE system is directly related with the solution of the optimization problem in equation (3.101). This splitting is proposed based on the ideas showed in subsection 2.7.1 and is given by

***Proposition* 3.8.1 (Second–order contact optimization algorithm)** *Splitting a contact Hamiltonian into the terms*

$$\mathcal{H}_{\phi_1} = \tfrac{e^{2\alpha}}{2} \|P\|^2 \tag{3.109}$$

$$\mathcal{H}_{\phi_2} = e^{\beta} f(X) \tag{3.110}$$

$$\mathcal{H}_{\phi_3} = \left(e^{\alpha} + \dot{\alpha}\right) S\,, \tag{3.111}$$

gives the following second–order contact integrator, which in turn derives an explicit optimization algorithm,

$$S_2(\tau) = e^{\frac{\tau}{2}\partial_t} e^{\frac{\tau}{2} X_{\phi_1}} e^{\frac{\tau}{2} X_{\phi_2}} e^{\tau X_{\phi_3}} e^{\frac{\tau}{2} X_{\phi_2}} e^{\frac{\tau}{2} X_{\phi_1}} e^{\frac{\tau}{2}\partial_t}\,, \tag{3.112}$$

where each map is given by

$$e^{\frac{\tau}{2}\partial_t}\begin{bmatrix} X \\ P \\ S \\ t \end{bmatrix} = \begin{bmatrix} X \\ P \\ S \\ t+\frac{\tau}{2} \end{bmatrix} \tag{3.113}$$

$$e^{\frac{\tau}{2}X_{\phi_1}}\begin{bmatrix} X \\ P \\ S \\ t \end{bmatrix} = \begin{bmatrix} X+\frac{\tau}{2}e^{2\alpha}P \\ P \\ S+\frac{\tau}{4}e^{2\alpha}\left\|P\right\|^2 \\ t \end{bmatrix} \tag{3.114}$$

$$e^{\frac{\tau}{2}X_{\phi_2}}\begin{bmatrix} X \\ P \\ S \\ t \end{bmatrix} = \begin{bmatrix} X \\ P-\frac{\tau}{2}e^{\beta}\nabla f(X) \\ S-\frac{\tau}{2}e^{\beta}f(X) \\ t \end{bmatrix} \tag{3.115}$$

$$e^{\tau X_{\phi_3}}\begin{bmatrix} X \\ P \\ S \\ t \end{bmatrix} = \begin{bmatrix} X \\ P\,e^{-\tau(e^{\alpha}+\dot{\alpha})} \\ S\,e^{-\tau(e^{\alpha}+\dot{\alpha})} \\ t \end{bmatrix}. \tag{3.116}$$

3.8.2 Numerical Results

To exemplify the results let us consider the correlated quadratic function

$$f(X)=\frac{1}{2}X^TAX,\quad A_{ij}=\frac{\sqrt{ij}}{2^{|i-j|}}\quad\text{for}\quad i,j=1,\dots,50\,. \tag{3.117}$$

with initial condition random in the range $-1\leq X_{0,i}\leq 1$ to test the robustness of each method to the initialization. Our results exemplify the convergence rate in equation (2.114) for orders $p=2,4,5,6,8,12$. We choose a final time to show the results. To stabilize the algorithm, for higher-order a lower step size is needed. That means that to reach the final time for small step sizes, more iterations are needed. That produces big computational costs to obtain good results in the high order regime.

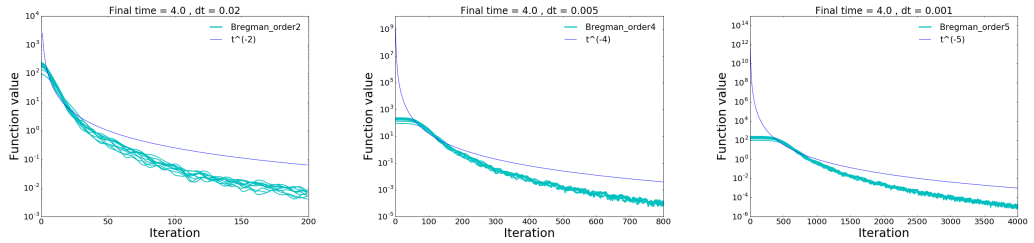

(a) (b) (c)

Figure 3.40: We exemplify how the discretization preserves the theoretical order for $p = 2, 4, 5$. Note that we decrease the step size dt as we increase the order p.

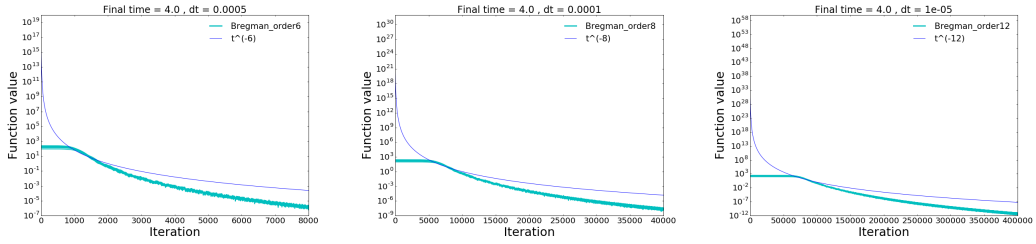

(a) (b) (c)

Figure 3.41: We exemplify how the discretization preserves the theoretical order for $p = 6, 8, 12$. For high order, the discretization may be unstable for high dt values.

Chapter 4

Discussion

Typical uncertainty quantification (UQ) problems include prediction, verification, validation (models and software), parameter estimation, and data assimilation. All possible sources of errors are considered in the UQ analysis as the forward modeling, observation, and discretization processes. Our specific interest relies on the challenges for the statistical approach for inverse problems produced by the presence of a dynamical system in the forward modeling. In this work, we analyze several uncertainty quantification strategies in different problems. The main contribution is for Bayesian model selection. First, we compute the normalization constants in a 1D example where the aim is to determine the number of coefficients in a Fourier series to represent the initial condition on the wave equation. Second, we compute the normalization constants using the low-rank approximation of the posterior covariance for linear Gaussian inverse problems. The same idea was applied in a linearized problem governed by an elliptic PDE. Both examples in 2D focus a in mesh refinement strategy and the model selection allows us to stop the refinement and compare between different criteria. Other results included (i) the comparison of two members of different families of transition kernels to perform the MCMC in an inference problem in 1D, (ii) the incorporation of optimal experimental design elements in the Multifrequency Algebraic Inversion with application to Magnetic Resonance Elastography, (iii) the inference for Oral Glucose Tolerance Test data by proposing modeling by an Erlang ODE system and a renewal equation perspective to model de delays in the body and (iv) the inference for an ODE

model that describes the early dynamics of the covid-19 in México. Finally, we also present a discretization that preserves theoretical convergence rates for an accelerated scheme with applications in optimization and machine learning. Now, we discuss our results.

We found that computing the normalization constants to compare several models allow determining optimal resolution or dimension for the inference. For the 1D example, this computation allows to considerably reduce the computational cost against a demanding MCMC as the reversible jump. For both 2D examples related to mesh refinement, for linear and linearized models, the normalization constant allows us to stop the refinement and to compare several refinement criteria with different information. Its application for nonlinear problems depends on each problem. Let us recall that having a locally refined mesh to perform the inference allows us to improve the results. Also, the refined mesh represents a tool when combining elements of different approaches. Traditional mesh refinement approaches include an error indicator to determine the region to refine. The criteria proposed in this work does not include this information. Consequently, the refinement does not allow us to reduce the L^2 error in the parameter. To combine uncertainty information and error indicators to perform the refinement is part of our future work.

We have found that t-walk slightly outperforms HAMCMC in the example at hand, e.g., HAMCMC fails to recover the variance of the points where the piecewise constant diffusion coefficient changes value. Our numerical experiments support the claim that for HAMCMC, the CM estimator does not fit the data well. Even though HAMCMC is asymptotically unbiased, an MH acceptance function contradicts this claim. In this case, the inverse Hessian approximation is not always definite positive. Of note, a constant regularization parameter λ can handicap the sampling. An eigendecomposition of H_t allows us to determine the value for λ at each t. This strategy is achievable in our case study but is prohibitive as the dimension increase. Even when t-walk needs a bigger chain, the sampling is faster due to the absence of derivative information. Densities with strong correlations and varying scales present several challenges at the sampling step. Despite its extensive computational effort and cost, local geometric information is introduced to obtain better samplings results.

The affine invariant property is a tool that allows us to face these challenges. As for optimization, a proposal guided only by the derivative information of the target density might not be enough when computational efficiency and high performance needs to be achieved. It is the case for a Quasi-Newton proposal (L-BFGS), specifically for HAMCMC. The Metropolized version of the complete Newton scheme satisfies the affine invariance property provided that the Hessian is positive definite. Bayesian inference (MCMC) demands approximations cheaper and faster but sufficiently informed.

We have found that introducing elements of optimal experimental design to the multifrequency algebraic inversion allow us to obtain an estimate with lower uncertainty and focalize in the region of interest. The way that we choose to decrease the uncertainty of the estimate was by computing the trace of the covariance matrix. For our simulations with synthetic data, we can compute the L^2 error between the estimate and the true parameter. The optimal design reduces this error. Other criteria to define the optimality may be implemented to compare these results.

We have found that modeling the glucose-insulin-glucagon dynamics by an Erlang ODE system allows obtaining good results in the inference of parameters on the Bayesian approach for the OGTT data. The modeling includes two insulin indicators, one related to blood level glucose, the other with the glucose level in the gastrointestinal tract. These indicators describe insulin dynamics due to oral stimulus. A possible classification for patients is described in Figure 3.31 (a). Patients diagnosed with IFG have an impaired value at fasting state and unimpaired values at two hours. Their insulin indicators classify these patients as healthy because their situation is not a consequence of the oral stimulus. A patient with IGT may have normal values for its insulin indicators as shown in Figure 3.32. From its glucose values, we can deduce that its situation is a consequence of impaired glucagon secretion. This anomaly will not be detected by the insulin indicators. To recognize this situation, the parameter θ_2 may provide information. As we discussed before, this parameter is not identifiable for all patients with their glucose values greater than the basal glucose level. Have measurements for more than two hours could solve the identifiability situation as we exemplify in Figure 3.33. Finally, the classification

places some healthy patients close to the transition zone. This situation may be a consequence of a high glucose level at 30 minutes, for θ_1, or at 1 hour and 30 minutes for θ_3, see Figure 3.32 (a). This may be the beginning of an anomaly which may be confirmed if patients stay under control and follow up for several months or years. From our results, it seems to us that the classification in healthy, IFG, IGT, IFG-IGT, and T2D could be modified to recognize more specific details about the cause of an impaired condition.

We have found in other works a discretization matching the theoretical rate of convergence in the context of acceleration methods for optimization and the inference on modeling the transmission human-environment for covid-19 for mexican data.

Chapter 5

Conclusions

Inverse problems arise in an enormous variety of science and engineering applications where model parameters must be estimated from noisy and indirect observational data. These problems are characterized by observational errors, model errors, and issues of ill-posedness which yield uncertainties in model parameters. Bayesian statistical approaches to inverse problems allow to make simulations and predictions with quantified uncertainties. These tasks become essential in model-based decision making. Verification and validation processes must be built focus in specific quantities of interest which allow to give answers to questions coming from the specific knowledge area. Diverse mathematical and computational branches as statistics, optimization, numerical analysis of ODEs/PDEs, and machine learning may meet to carry out this work. In this work, we have seen how theoretical conditions allow us to ensure a correct approach to numerics. These conditions give consistency on the discretization and produce stability in the numerical surrogate posterior. Possible applications like the ones we show in medical imaging, epidemiology, and biology illustrate how a probabilistic approach to encode errors in the modeling process may lead to predictive simulations with reliable uncertainty measures in real-world problems. However, more demanding applications bring with them more challenges related to power computing, high-dimensionality in data and parameters, prediction, multifidelity, and others that we do not address in this work.

Appendices

Appendix A

A note on optimization

A.1 Inexact Newton methods

The cost of factoring the Hessian is prohibitive, and it is preferable to compute approximations to the Newton step using iterative linear algebra techniques. The inexact Newton method use these technique. Recall that the Newton step is given by

$$H_k p_k = -g_k \tag{A.1}$$

The aim of these methods is to obtain inexpensive approximations of p_k for large dimensions. The idea is to solve A.1 by the conjugate gradient method. Lanczos method can be used too instead. Some modifications are needed to handle with negative curvature in the Hessian H_k. Note that we look for implement methods *Hessian free*, that is, where H_k not need to be calculated or stored explicitly.

To terminate an iterative solver for A.1, we consider the residual

$$r_k = H_k p_k + g_k \tag{A.2}$$

Usually, we terminate the CG iterations when

$$||r_k|| \leq \eta_k ||\nabla f_k|| \tag{A.3}$$

The sequence $\{\eta_k\}$ is called the forcing sequence. If the starting point is sufficiently near of the optimum, the convergence is obtained by ensuring that

$\eta_k \leq \eta < 1$, see [156]. Since the Hessian H_k may have negative eigenvalues when x_k is not close to a solution, the CG is adapted to terminate as soon a direction of negative curvature is generated. hIPPYlib uses Eisenstat-Walker [157] to choose the forcing sequence and Steihaug [158] to avoid negative curvature.

A.2 The Gauss Newton approximation of the Hessian

Consider the problem of minimizing the function S given by

$$S(\mathbf{x}) = \sum_{i=0}^{k} s_i^2(\mathbf{x}) \tag{A.4}$$

where $s_i : \mathbb{R}^n \to \mathbb{R}$. The Gauss Newton approximation of the Hessian is a modification of the Newton method that drop off the second derivatives, which may be hard and expensive to compute. If we denote by $\mathbf{g}$ the gradient of the function in equation (A.4), then

$$\mathbf{g}_j = 2\sum_{i=0}^{k} s_i \frac{\partial s_i(\mathbf{x})}{\partial x_j}, \qquad j = 1, \ldots, n \tag{A.5}$$

where $x_j = \mathbf{x}_j$. The Hessian matrix is computed by differentiating $\mathbf{g}$ and is given by

$$\mathbf{H}_{jp} = 2\left(\sum_{i=0}^{k} \frac{\partial s_i(\mathbf{x})}{\partial x_j}\frac{\partial s_i(\mathbf{x})}{\partial x_p} + s_i \frac{\partial^2 s_i(\mathbf{x})}{\partial x_j \partial x_p}\right), \qquad j, p = 1, \ldots, n \tag{A.6}$$

The Gauss-Newton approximation $\mathbf{H}^{GN}$ of $\mathbf{H}$ is

$$\mathbf{H}^{GN}_{jp} = 2\left(\sum_{i=0}^{k} \frac{\partial s_i(\mathbf{x})}{\partial x_j}\frac{\partial s_i(\mathbf{x})}{\partial x_p}\right), \qquad j, p = 1, \ldots, n \tag{A.7}$$

Motivated by this approximation, second derivatives in equations 2.50 and 2.51 of the forward problem are drop to compute the Gauss Newton approximation

of the Hessian for the pde constrained optimization.

A.3 GMRES

One of the most effective iterative methods for solving large sparse symmetric positive definite linear systems of equations is a combination of the conjugate gradient method with some preconditioning technique. Authors in [159] introduce a generalized minimal residual algorithm for solving nonsymmetric linear systems, the GMRES. The method is based on the Arnoldi process, which is the analogue of the Lanczos algorithm for nonsymmetric matrices. Arnoldi's method uses the Gram-Schmidt method for computing an l_2-orthonormal basis $\{v_1, v_2, \ldots, v_k\}$ of the Krylov subspace $K_k \equiv \text{span}\{v_1, Av_1, \cdots, A^{k-1}v_1\}$. In order to solve the linear system

$$Ax = f \tag{A.8}$$

we seek an approximate solution x_k of the form $x_k = x_0 + z_k$, where x_0 is some initial guess to the solution x and z_k is a member of the Krylov subspace $K_k \equiv \text{span}\{r_0, Ar_0, \cdots, A^{k-1}r_0\}$ with $r_0 = f - Ax_0$. Several methods to obtain this z_k are known which can break down of have stability problems for indefinite matrix cases. The GMRES method introduced in [159] uses the basis generated by Arnoldi's method to circumvent this limitation. The idea is to solve the least squares problem:

$$\min_{z \in K_k} ||f - A(x_0 + z)|| = \min_{z \in K_k} ||r_0 - Az|| \tag{A.9}$$

Since Arnoldi's method give us a basis for K_k, we can set $z = V_k y$ where V_k is the matrix formed by the elements basis $\{v_1, v_2, \cdots, v_k\}$. The solution is given by $x_k = x_0 + V_k y_k$ where y_k minimizes a constraint function with $y \in R^k$. In practice, when k increases, the number of vectors in storage increases like k. Same authors proposed a restarted version of GMRES denoted by GMRES(m). Over the years implementation modifications have been proposed to improve efficiency [160, 161, 162].

Appendix B

Mesh refinement for a coefficient in an elliptic equation

Let us recall the refinement criteria mentioned in subsection 3.3.4:

1. Comparing the changes on the posterior mean with respect to the prior mean.
2. Comparing the changes on the posterior mean and variance with respect to the prior mean and variance (ADS introduced previous subsection).
3. Refining the region of the boundary of the inclusion.
4. Refining the element with higher gradient.

We show the successive meshes generated by criterium 2 in Figure B.1, criterium 3 in figure B.2 and criterium 4 in figure B.3. Also, we implemented these four criteria for an example with two hard inclusions, see Figures B.4 - B.7.

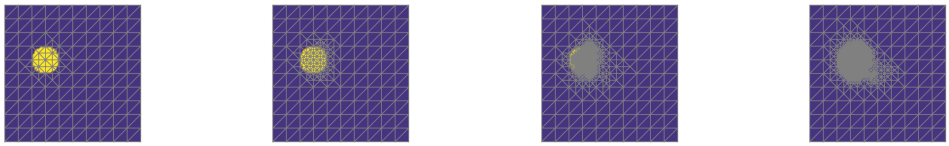

(a) (b) (c) (d)

Figure B.1: Local refinement based on the change of the posterior mean and variance with respect to the prior mean and variance (a) mesh 2, (b) mesh3, (c) mesh4, (d) mesh5.

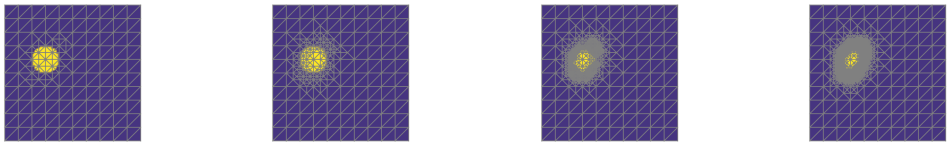

(a) (b) (c) (d)

Figure B.2: Local refinement based on the change of the posterior mean with respect to the prior mean to refine the boundary area (a) mesh 2, (b) mesh3, (c) mesh4, (d) mesh5.

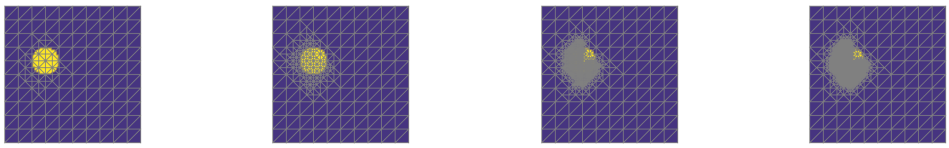

(a) (b) (c) (d)

Figure B.3: Local refinement based on the change of the gradient (a) mesh 2, (b) mesh3, (c) mesh4, (d) mesh5.

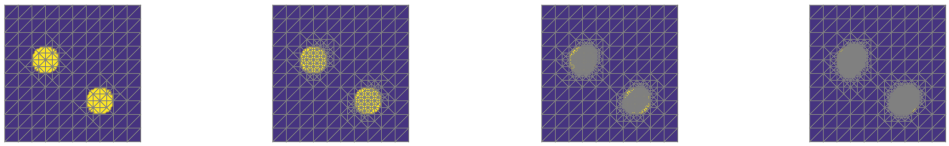

(a) (b) (c) (d)

Figure B.4: Local refinement based on the change of the posterior mean with respect to the prior mean for two inclusions (a) mesh 2, (b) mesh3, (c) mesh4, (d) mesh5.

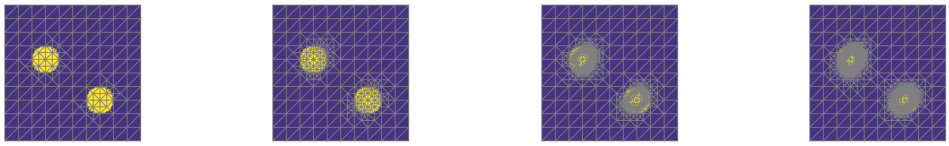

(a) (b) (c) (d)

Figure B.5: Local refinement based on the change of the posterior mean with respect to the prior mean to refine the boundary area for two inclusions (a) mesh 2, (b) mesh3, (c) mesh4, (d) mesh5.

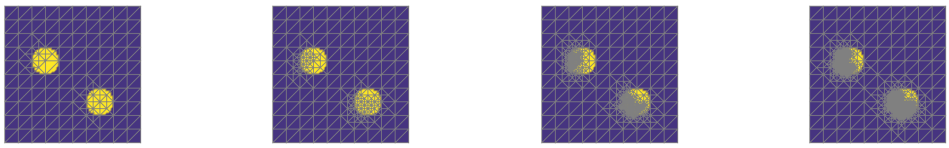

(a) (b) (c) (d)

Figure B.6: Local refinement based on the change of the gradient of the posterior mean for two inclusions (a) mesh 2, (b) mesh3, (c) mesh4, (d) mesh5.

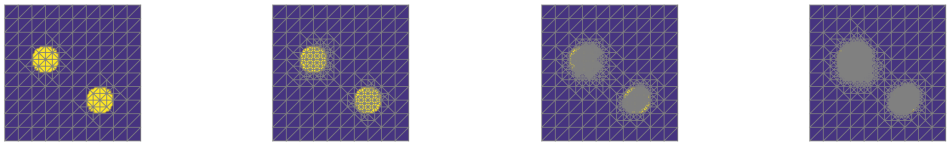

(a) (b) (c) (d)

Figure B.7: Local refinement based on the change of the posterior mean and variance with respect to the prior mean and variance for two inclusions(a) mesh 2, (b) mesh3, (c) mesh4, (d) mesh5.

Appendix C

Some models for glucose-insulin dynamics

In the last decades, diabetes has become the main health problem in Mexico. It is the principal cause of death in women since the year 2000. It is the primary cause of premature retirement, blindness, and kidney failure. By the year 2025, close to 11.7 million Mexicans are expected to be diagnosed with diabetes. Many mathematical models have been developed to better understand the dynamics of the glucose-insulin system. A review of some mathematical models can be found in [124]. In this section, we describe two models for better understand the ideas in the modeling proposed in section 3.6. The next model was presented in [36]

$$\begin{aligned} \dot{G} &= (L - I)\, G + \frac{D}{\theta_2} \\ \dot{I} &= \theta_0 \left(\frac{G}{G_0} - 1 \right)^{+} - \frac{I}{a} \\ \dot{L} &= \theta_1 \left(1 - \frac{G}{G_0} \right)^{+} - \frac{L}{b} \\ \dot{D} &= -\frac{D}{\theta_2} \end{aligned} \tag{C.1}$$

where $G(t)$ is the blood glucose level at time t, $I(t)$ is the blood insulin level at time t and $L(t)$ the glucagon levels. Also, $D(t)$ is the digestive system 'glucose level'. This model shows, again, that when $G(t)$ is over a threshold value, G_b, insulin is produced. For the contrary, when $G(t)$ is under that value, glucagon is produced.

A model with time delay: Authors in [128] proposed the following model

$$\dot{x} = -a_1 x(t) - a_2 x(t-\tau) y(t-\tau) + a_3, \tag{C.2}$$

$$\dot{y} = b_1 x(t) - b_2 y(t) \tag{C.3}$$

where $x(t)$ represents glucose concentration and $y(t)$ insulin concentration, a_1 and a_2 are desappearance rates, a_3 is the glucose infusion rate, b_1 is the insulin production rate and b_2 is the insulin degradation rate. The time delay τ represents the time taken by the pancreas to respond.

In section 3.6, we model this delay by an Erlang distribution by introducing substages for compartments in insulin, glucagon and digestive system. Also, as the model in the system (C.1), we model the insulin (glucagon) secretion by a positive part of the quantity $G - G_b$ $(G_b - G)$.

Appendix D

Sensitivity Analysis

The sensitivity analysis is the study of how the uncertainty in the output of a mathematical model can be apportioned to different sources of uncertainty in its inputs. This study can be made determining *sensitivity indices*, which according to [163], are used for estimating the influence of individual variables or groups of variables on the model output. Given a model of the form

$$Y = f(X_1, X_2, ..., X_k) \tag{D.1}$$

with Y a scalar, a variance based first order effect for a generic factor X_i can be written as

$$V_{X_i}\left(E_{X\sim i}(Y|X_i)\right)$$

where $E_{X\sim i}(\cdot)$ is the mean of argument $(\cdot)$ taken over all factors but X_i and $V_{X_i}(\cdot)$ is the variance of argument $(\cdot)$ taken over X_i. The meaning of the inner expectation operator is that the mean of Y is taken over all possible values of $X \sim i$ while keeping X_i fixed. The outer variance is taken over all possible values of X_i. The associated sensitivity measure (first order sensitivity coefficient) is written as:

$$S_i = \frac{V_{X_i}\left(E_{X\sim i}(Y|X_i)\right)}{V(Y)} \tag{D.2}$$

Bibliography

[1] Ville Kolehmainen, Matti Lassas, and Petri Ola. The inverse conductivity problem with an imperfectly known boundary. *SIAM Journal on Applied Mathematics*, 66(2):365–383, 2005.

[2] Likun Tan, Matthew DJ McGarry, Elijah EW Van Houten, Ming Ji, Ligin Solamen, John B Weaver, and Keith D Paulsen. Gradient-based optimization for poroelastic and viscoelastic mr elastography. *IEEE transactions on medical imaging*, 36(1):236–250, 2016.

[3] Lassi Roininen, Janne MJ Huttunen, and Sari Lasanen. Whittle-matérn priors for bayesian statistical inversion with applications in electrical impedance tomography. *Inverse Probl. Imaging*, 8(2):561, 2014.

[4] Ioannis Epanomeritakis, Volkan Akçelik, Omar Ghattas, and Jacobo Bielak. A newton-cg method for large-scale three-dimensional elastic full-waveform seismic inversion. *Inverse Problems*, 24(3):034015, 2008.

[5] Jeroen Tromp, Dimitri Komatitsch, and Qinya Liu. Spectral-element and adjoint methods in seismology. *Communications in Computational Physics*, 3(1):1–32, 2008.

[6] Jorge Xicoténcatl Velasco-Hernández, Mayra Núñez-López, Andreu Comas-García, Daniel Ernesto Noyola Cherpitel, and Marcos Capistrán Ocampo. Superinfection between influenza and rsv alternating patterns in san luis potosí state, méxico. *PloS one*, 10(3):e0115674, 2015.

[7] Noemi Petra, James Martin, Georg Stadler, and Omar Ghattas. A computational framework for infinite-dimensional bayesian inverse

problems, part ii: Stochastic newton mcmc with application to ice sheet flow inverse problems. *SIAM Journal on Scientific Computing*, 36(4):A1525–A1555, 2014.

[8] Daniela Calvetti, Ranjan K Dash, Erkki Somersalo, and Marco E Cabrera. Local regularization method applied to estimating oxygen consumption during muscle activities. *Inverse problems*, 22(1):229, 2006.

[9] Guy Baele, Philippe Lemey, Andrew Rambaut, and Marc A Suchard. Adaptive mcmc in bayesian phylogenetics: an application to analyzing partitioned data in beast. *Bioinformatics*, 33(12):1798–1805, 2017.

[10] Adrian E Raftery, Tilmann Gneiting, Fadoua Balabdaoui, and Michael Polakowski. Using bayesian model averaging to calibrate forecast ensembles. *Monthly weather review*, 133(5):1155–1174, 2005.

[11] Alessio Spantini, Antti Solonen, Tiangang Cui, James Martin, Luis Tenorio, and Youssef Marzouk. Optimal low-rank approximations of bayesian linear inverse problems. *SIAM Journal on Scientific Computing*, 37(6):A2451–A2487, 2015.

[12] Alessio Spantini, Tiangang Cui, Karen Willcox, Luis Tenorio, and Youssef Marzouk. Goal-oriented optimal approximations of bayesian linear inverse problems. *SIAM Journal on Scientific Computing*, 39(5):S167–S196, 2017.

[13] Chad Lieberman and Karen Willcox. Goal-oriented inference: Approach, linear theory, and application to advection diffusion. *siam REVIEW*, 55(3):493–519, 2013.

[14] J Andrés Christen, Marcos A Capistrán, M Luisa Daza-Torres, Hugo Flores-Argüedas, and J Cricelio Montesinos-López. Posterior distribution existence and error control in banach spaces in the bayesian approach to uq in inverse problems. *arXiv preprint arXiv:1712.03299*, 2017.

[15] Andrew M Stuart. Inverse problems: a bayesian perspective. *Acta numerica*, 19:451–559, 2010.

[16] Björn Sprungk. On the local lipschitz stability of bayesian inverse problems. *Inverse Problems*, 36(5):055015, 2020.

[17] Jonas Latz. On the well-posedness of bayesian inverse problems. *SIAM/ASA Journal on Uncertainty Quantification*, 8(1):451–482, 2020.

[18] Tan Bui-Thanh, Omar Ghattas, James Martin, and Georg Stadler. A computational framework for infinite-dimensional bayesian inverse problems part i: The linearized case, with application to global seismic inversion. *SIAM Journal on Scientific Computing*, 35(6):A2494–A2523, 2013.

[19] Tan Bui-Thanh and Quoc P Nguyen. Fem-based discretization-invariant mcmc methods for pde-constrained bayesian inverse problems. *Inverse Problems & Imaging*, 10(4):943, 2016.

[20] Lucas C Wilcox, Georg Stadler, Tan Bui-Thanh, and Omar Ghattas. Discretely exact derivatives for hyperbolic pde-constrained optimization problems discretized by the discontinuous galerkin method. *Journal of Scientific Computing*, 63(1):138–162, 2015.

[21] Shiwei Lan. Adaptive dimension reduction to accelerate infinite-dimensional geometric markov chain monte carlo. *Journal of Computational Physics*, 392:71–95, 2019.

[22] Alexandros Beskos, Ajay Jasra, Kody Law, Youssef Marzouk, and Yan Zhou. Multilevel sequential monte carlo with dimension-independent likelihood-informed proposals. *SIAM/ASA Journal on Uncertainty Quantification*, 6(2):762–786, 2018.

[23] Tan Bui-Thanh, Carsten Burstedde, Omar Ghattas, James Martin, Georg Stadler, and Lucas C Wilcox. Extreme-scale uq for bayesian inverse problems governed by pdes. In *Proceedings of the international conference on high performance computing, networking, storage and analysis*, page 3. IEEE Computer Society Press, 2012.

[24] Yulong Lu. On the bernstein-von mises theorem for high dimensional nonlinear bayesian inverse problems. *arXiv preprint arXiv:1706.00289*, 2017.

[25] Claudia Schillings, Björn Sprungk, and Philipp Wacker. On the convergence of the laplace approximation and noise-level-robustness of laplace-based monte carlo methods for bayesian inverse problems. *arXiv preprint arXiv:1901.03958*, 2019.

[26] Matteo Giordano and Hanne Kekkonen. Bernstein–von mises theorems and uncertainty quantification for linear inverse problems. *SIAM/ASA Journal on Uncertainty Quantification*, 8(1):342–373, 2020.

[27] Masoumeh Dashti, Stephen Harris, and Andrew Stuart. Besov priors for bayesian inverse problems. *arXiv preprint arXiv:1105.0889*, 2011.

[28] Zhewei Yao, Zixi Hu, and Jinglai Li. A tv-gaussian prior for infinite-dimensional bayesian inverse problems and its numerical implementations. *Inverse Problems*, 32(7):075006, 2016.

[29] Bamdad Hosseini and Nilima Nigam. Well-posed bayesian inverse problems: Priors with exponential tails. *SIAM/ASA Journal on Uncertainty Quantification*, 5(1):436–465, 2017.

[30] Tiangang Cui, Kody JH Law, and Youssef M Marzouk. Dimension-independent likelihood-informed mcmc. *Journal of Computational Physics*, 304:109–137, 2016.

[31] Tiangang Cui, Youssef M Marzouk, and Karen E Willcox. Data-driven model reduction for the bayesian solution of inverse problems. *International Journal for Numerical Methods in Engineering*, 102(5):966–990, 2015.

[32] Youssef Marzouk and Dongbin Xiu. A stochastic collocation approach to bayesian inference in inverse problems. 2009.

[33] Youssef M Marzouk and Habib N Najm. Dimensionality reduction and polynomial chaos acceleration of bayesian inference in inverse problems. *Journal of Computational Physics*, 228(6):1862–1902, 2009.

[34] Paul G Constantine, Eric Dow, and Qiqi Wang. Active subspace methods in theory and practice: applications to kriging surfaces. *SIAM Journal on Scientific Computing*, 36(4):A1500–A1524, 2014.

[35] Remi R Lam, Olivier Zahm, Youssef M Marzouk, and Karen E Willcox. Multifidelity dimension reduction via active subspaces. *SIAM Journal on Scientific Computing*, 42(2):A929–A956, 2020.

[36] Marcos A Capistrán, J Andrés Christen, and Sophie Donnet. Bayesian analysis of odes: Solver optimal accuracy and bayes factors. *SIAM/ASA Journal on Uncertainty Quantification*, 4(1):829–849, 2016.

[37] Tan Bui-Thanh and Omar Ghattas. An analysis of infinite dimensional bayesian inverse shape acoustic scattering and its numerical approximation. *SIAM/ASA Journal on Uncertainty Quantification*, 2(1):203–222, 2014.

[38] Abel Palafox, Marcos A Capistrán, and J Andrés Christen. Effective parameter dimension via bayesian model selection in the inverse acoustic scattering problem. *Mathematical Problems in Engineering*, 2014, 2014.

[39] Orcun Goksel, Hani Eskandari, and Septimiu E Salcudean. Mesh adaptation for improving elasticity reconstruction using the fem inverse problem. *IEEE transactions on medical imaging*, 32(2):408–418, 2012.

[40] Alexander Arnold, Stefan Reichling, Otto T Bruhns, and Jörn Mosler. Efficient computation of the elastography inverse problem by combining variational mesh adaption and a clustering technique. *Physics in Medicine & Biology*, 55(7):2035, 2010.

[41] Wenxia Wang, Wei Zou, Danfeng Hu, and Jiajun Wang. Adaptive mesh refinement for elastic modulus reconstruction in elastography. *Proceedings*

of the Institution of Mechanical Engineers, Part H: Journal of Engineering in Medicine, 232(3):215–229, 2018.

[42] Wolfgang Bangerth. A framework for the adaptive finite element solution of large-scale inverse problems. *SIAM Journal on Scientific Computing*, 30(6):2965–2989, 2008.

[43] Roland Becker and Rolf Rannacher. An optimal control approach to a posteriori error estimation in finite element methods. *Acta numerica*, 10:1–102, 2001.

[44] Roland Becker and Boris Vexler. A posteriori error estimation for finite element discretization of parameter identification problems. *Numerische Mathematik*, 96(3):435–459, 2004.

[45] Jari Kaipio and Erkki Somersalo. *Statistical and computational inverse problems*, volume 160. Springer Science & Business Media, 2006.

[46] Masoumeh Dashti and Andrew M Stuart. The bayesian approach to inverse problems. *Handbook of Uncertainty Quantification*, pages 1–118, 2016.

[47] Joseph T Chang and David Pollard. Conditioning as disintegration. *Statistica Neerlandica*, 51(3):287–317, 1997.

[48] Kenta Cho and Bart Jacobs. Disintegration and bayesian inversion, both abstractly and concretely. *See arxiv. org/abs/1709.00322*, 2017.

[49] Vladimir Igorevich Bogachev. *Gaussian measures*. Number 62. American Mathematical Soc., 1998.

[50] Finn Lindgren, Håvard Rue, and Johan Lindström. An explicit link between gaussian fields and gaussian markov random fields: the stochastic partial differential equation approach. *Journal of the Royal Statistical Society: Series B (Statistical Methodology)*, 73(4):423–498, 2011.

[51] Matthew M Dunlop and Andrew M Stuart. The bayesian formulation of eit: analysis and algorithms. *arXiv preprint arXiv:1508.04106*, 2015.

[52] Lassi Roininen, Mark Girolami, Sari Lasanen, and Markku Markkanen. Hyperpriors for mat\'ern fields with applications in bayesian inversion. *arXiv preprint arXiv:1612.02989*, 2016.

[53] Matthew M Dunlop, Marco A Iglesias, and Andrew M Stuart. Hierarchical bayesian level set inversion. *Statistics and Computing*, 27(6):1555–1584, 2017.

[54] Yair Daon and Georg Stadler. Mitigating the influence of the boundary on pde-based covariance operators. *arXiv preprint arXiv:1610.05280*, 2016.

[55] Umberto Villa, Noemi Petra, and Omar Ghattas. hippylib: An extensible software framework for large-scale inverse problems. *J. Open Source Software*, 3(30):940, 2018.

[56] Sudhakar Kundapur Venkatesh and Richard L Ehman. Magnetic resonance elastography of liver. *Magnetic Resonance Imaging Clinics*, 22(3):433–446, 2014.

[57] Hanne Kekkonen, Matti Lassas, and Samuli Siltanen. Posterior consistency and convergence rates for bayesian inversion with hypoelliptic operators. *Inverse Problems*, 32(8):085005, 2016.

[58] Sebastian J Vollmer. Posterior consistency for bayesian inverse problems through stability and regression results. *Inverse Problems*, 29(12):125011, 2013.

[59] TJ Sullivan. Well-posedness of bayesian inverse problems in quasi-banach spaces with stable priors. *PAMM*, 17(1):871–874, 2017.

[60] Sergios Agapiou, Stig Larsson, and Andrew M Stuart. Posterior consistency of the bayesian approach to linear ill-posed inverse problems. 2012.

[61] Han Cheng Lie, Timothy John Sullivan, and Aretha Teckentrup. Error bounds for some approximate posterior measures in bayesian inference. *arXiv preprint arXiv:1911.05669*, 2019.

[62] Andrew Stuart and Aretha Teckentrup. Posterior consistency for gaussian process approximations of bayesian posterior distributions. *Mathematics of Computation*, 87(310):721–753, 2018.

[63] Alison L Gibbs and Francis Edward Su. On choosing and bounding probability metrics. *International statistical review*, 70(3):419–435, 2002.

[64] Yi-An Ma, Tianqi Chen, and Emily Fox. A complete recipe for stochastic gradient mcmc. In *Advances in Neural Information Processing Systems*, pages 2917–2925, 2015.

[65] J Andrés Christen and Colin Fox. A general purpose sampling algorithm for continuous distributions (the t-walk). *Bayesian Analysis*, 5(2):263–281, 2010.

[66] Jonathan Goodman and Jonathan Weare. Ensemble samplers with affine invariance. *Communications in applied mathematics and computational science*, 5(1):65–80, 2010.

[67] Daniel Foreman-Mackey, David W Hogg, Dustin Lang, and Jonathan Goodman. emcee: the mcmc hammer. *Publications of the Astronomical Society of the Pacific*, 125(925):306, 2013.

[68] Abel Palafox, Marcos Capistrán, and J Andrés Christen. Point cloud-based scatterer approximation and affine invariant sampling in the inverse scattering problem. *Mathematical Methods in the Applied Sciences*, 40(9):3393–3403, 2017.

[69] Maria L Daza, Marcos A Capistrán, J Andrés Christen, and Lilí Guadarrama. Solution of the inverse scattering problem from inhomogeneous media using affine invariant sampling. *Mathematical Methods in the Applied Sciences*, 40(9):3311–3319, 2017.

[70] Mark Girolami and Ben Calderhead. Riemann manifold langevin and hamiltonian monte carlo methods. *Journal of the Royal Statistical Society: Series B (Statistical Methodology)*, 73(2):123–214, 2011.

[71] James Martin, Lucas C Wilcox, Carsten Burstedde, and Omar Ghattas. A stochastic newton mcmc method for large-scale statistical inverse problems with application to seismic inversion. *SIAM Journal on Scientific Computing*, 34(3):A1460–A1487, 2012.

[72] N Petra, J Martin, G Stadler, and O Ghattas. A stochastic newton mcmc method with applications to ice sheet inverse problems. *AGUFM*, 2012:GC32A–07, 2012.

[73] T Bui-Thanh and OMAR Ghattas. A scaled stochastic newton algorithm for markov chain monte carlo simulations. *SIAM Journal on Uncertainty Quantification*, pages 1–25, 2012.

[74] Umut Simsekli, Roland Badeau, Taylan Cemgil, and Gaël Richard. Stochastic quasi-newton langevin monte carlo. 2016.

[75] Dominique Bontemps et al. Bernstein–von mises theorems for gaussian regression with increasing number of regressors. *The Annals of Statistics*, 39(5):2557–2584, 2011.

[76] Lucien Le Cam and Grace Lo Yang. *Asymptotics in statistics: some basic concepts*. Springer Science & Business Media, 2012.

[77] George Biros and Omar Ghattas. Parallel lagrange–newton–krylov–schur methods for pde-constrained optimization. part i: The krylov–schur solver. *SIAM Journal on Scientific Computing*, 27(2):687–713, 2005.

[78] Pei Chen. Hessian matrix vs. gauss–newton hessian matrix. *SIAM Journal on Numerical Analysis*, 49(4):1417–1435, 2011.

[79] Nathan Halko, Per-Gunnar Martinsson, and Joel A Tropp. Finding structure with randomness: Probabilistic algorithms for constructing approximate matrix decompositions. *SIAM review*, 53(2):217–288, 2011.

[80] Arvind K Saibaba, Jonghyun Lee, and Peter K Kitanidis. Randomized algorithms for generalized hermitian eigenvalue problems with application to computing karhunen–loève expansion. *Numerical Linear Algebra with Applications*, 23(2):314–339, 2016.

[81] Robert E Kass and Adrian E Raftery. Bayes factors. *Journal of the american statistical association*, 90(430):773–795, 1995.

[82] Isabella Verdinelli and Larry Wasserman. Computing bayes factors using a generalization of the savage-dickey density ratio. *Journal of the American Statistical Association*, 90(430):614–618, 1995.

[83] Andrew Gelman and Xiao-Li Meng. Simulating normalizing constants: From importance sampling to bridge sampling to path sampling. *Statistical science*, pages 163–185, 1998.

[84] Luc Devroye, Abbas Mehrabian, and Tommy Reddad. The total variation distance between high-dimensional gaussians. *arXiv preprint arXiv:1810.08693*, 2018.

[85] Christopher KI Williams and Carl Edward Rasmussen. *Gaussian processes for machine learning*, volume 2. MIT press Cambridge, MA, 2006.

[86] Gavin Low, Scott A Kruse, and David J Lomas. General review of magnetic resonance elastography. *World journal of radiology*, 8(1):59, 2016.

[87] Eric Jones, Travis Oliphant, Pearu Peterson, et al. Scipy: Open source scientific tools for python. 2001.

[88] Armando Manduca, Travis E Oliphant, M Alex Dresner, JL Mahowald, Scott A Kruse, E Amromin, Joel P Felmlee, James F Greenleaf, and Richard L Ehman. Magnetic resonance elastography: non-invasive mapping of tissue elasticity. *Medical image analysis*, 5(4):237–254, 2001.

[89] Jiming Zhang and Raja Muthupillai. Magnetic resonance elastography. In *Handbook of Imaging in Biological Mechanics*, pages 54–75. CRC Press Boca Raton, 2014.

[90] Matthew McGarry, Elijah Van Houten, Ligin Solamen, Scott Gordon-Wylie, John Weaver, and Keith Paulsen. Uniqueness of poroelastic and viscoelastic nonlinear inversion mr elastography at low frequencies. *Physics in Medicine & Biology*, 64(7):075006, 2019.

[91] Sebastian Hirsch, Jurgen Braun, and Ingolf Sack. *Magnetic resonance elastography: physical background and medical applications*. John Wiley & Sons, 2017.

[92] Travis E Oliphant, Armando Manduca, Richard L Ehman, and James F Greenleaf. Complex-valued stiffness reconstruction for magnetic resonance elastography by algebraic inversion of the differential equation. *Magnetic Resonance in Medicine: An Official Journal of the International Society for Magnetic Resonance in Medicine*, 45(2):299–310, 2001.

[93] Ronald W Schafer et al. What is a savitzky-golay filter. *IEEE Signal processing magazine*, 28(4):111–117, 2011.

[94] Ivan W Selesnick, Richard G Baraniuk, and Nicholas G Kingsbury. The dual-tree complex wavelet transform. *IEEE signal processing magazine*, 22(6):123–151, 2005.

[95] Sunder Ram Krishnan and Chandra Sekhar Seelamantula. On the selection of optimum savitzky-golay filters. *IEEE transactions on signal processing*, 61(2):380–391, 2012.

[96] C Antonio Sánchez, Corina S Drapaca, Sivabal Sivaloganathan, and Edward R Vrscay. Elastography of biological tissue: direct inversion methods that allow for local shear modulus variations. In *International Conference Image Analysis and Recognition*, pages 195–206. Springer, 2010.

[97] S Papazoglou, U Hamhaber, J Braun, and I Sack. Algebraic helmholtz inversion in planar magnetic resonance elastography. *Physics in Medicine & Biology*, 53(12):3147, 2008.

[98] Marvin M Doyley. Model-based elastography: a survey of approaches to the inverse elasticity problem. *Physics in Medicine & Biology*, 57(3):R35, 2012.

[99] Martin S. Alnæs, Jan Blechta, Johan Hake, August Johansson, Benjamin Kehlet, Anders Logg, Chris Richardson, Johannes Ring, Marie E. Rognes,

and Garth N. Wells. The fenics project version 1.5. *Archive of Numerical Software*, 3(100), 2015.

[100] Michael Vogelius. An analysis of the p-version of the finite element method for nearly incompressible materials. *Numerische Mathematik*, 41(1):39–53, 1983.

[101] Mohammad Honarvar, Ramin S Sahebjavaher, Robert Rohling, and Septimiu E Salcudean. A comparison of finite element-based inversion algorithms, local frequency estimation, and direct inversion approach used in mre. *IEEE transactions on medical imaging*, 36(8):1686–1698, 2017.

[102] Mohammad Honarvar, Ramin Sahebjavaher, Ralph Sinkus, Robert Rohling, and Septimiu E Salcudean. Curl-based finite element reconstruction of the shear modulus without assuming local homogeneity: time harmonic case. *IEEE transactions on medical imaging*, 32(12):2189–2199, 2013.

[103] R Liu, Mary F Wheeler, and Clinton N Dawson. A three-dimensional nodal-based implementation of a family of discontinuous galerkin methods for elasticity problems. *Computers & Structures*, 87(3-4):141–150, 2009.

[104] Sebastian Papazoglou, Sebastian Hirsch, Jürgen Braun, and Ingolf Sack. Multifrequency inversion in magnetic resonance elastography. *Physics in Medicine & Biology*, 57(8):2329, 2012.

[105] Eric Barnhill, Penny J Davies, Cemre Ariyurek, Andreas Fehlner, Jürgen Braun, and Ingolf Sack. Heterogeneous multifrequency direct inversion (hmdi) for magnetic resonance elastography with application to a clinical brain exam. *Medical image analysis*, 46:180–188, 2018.

[106] Weijie Su, Stephen Boyd, and Emmanuel J. Candès. A differential equation for modeling Nesterov's accelerated gradient method: Theory and insights. *Journal of Machine Learning Research*, 17(153):1–43, 2016.

[107] Uwe Helmke and John B Moore. *Optimization and dynamical systems*. Springer Science & Business Media, 2012.

[108] Johannes Schropp and I Singer. A dynamical systems approach to constrained minimization. *Numerical functional analysis and optimization*, 21(3-4):537–551, 2000.

[109] AA Brown and Michael C Bartholomew-Biggs. Some effective methods for unconstrained optimization based on the solution of systems of ordinary differential equations. *Journal of Optimization Theory and Applications*, 62(2):211–224, 1989.

[110] Radu Ioan Boţ, Ernö Robert Csetnek, and Szilárd Csaba László. A second-order dynamical approach with variable damping to nonconvex smooth minimization. *Applicable Analysis*, 99(3):361–378, 2020.

[111] Hedy Attouch, Zaki Chbani, Juan Peypouquet, and Patrick Redont. Fast convergence of inertial dynamics and algorithms with asymptotic vanishing viscosity. *Mathematical Programming*, 168(1-2):123–175, 2018.

[112] Alessandro Bravetti, Maria L Daza-Torres, Hugo Flores-Arguedas, and Michael Betancourt. Optimization algorithms inspired by the geometry of dissipative systems. *arXiv preprint arXiv:1912.02928*, 2019.

[113] Andre Wibisono, Ashia C Wilson, and Michael I Jordan. A variational perspective on accelerated methods in optimization. *proceedings of the National Academy of Sciences*, 113(47):E7351–E7358, 2016.

[114] Michael Betancourt, Michael I Jordan, and Ashia C Wilson. On symplectic optimization. *arXiv preprint arXiv:1802.03653*, 2018.

[115] Mats Vermeeren, Alessandro Bravetti, and Marcello Seri. Contact variational integrators. *Journal of Physics A: Mathematical and Theoretical*, 52(44):445206, 2019.

[116] Robert I McLachlan and G Reinout W Quispel. Splitting methods. *Acta Numerica*, 11:341–434, 2002.

[117] Lawrence C Evans. Partial differential equations. graduate studies in mathematics. *American mathematical society*, 2:1998, 1998.

[118] James O Berger. *Statistical decision theory and Bayesian analysis*. Springer Science & Business Media, 2013.

[119] Ne-Zheng Sun and Alexander Sun. *Model calibration and parameter estimation: for environmental and water resource systems*. Springer, 2015.

[120] Viatcheslav B Melas. Fundamentals of the optimal experimental design. *Functional Approach to Optimal Experimental Design*, pages 5–21, 2006.

[121] Leszek Szablewski. Glucose homeostasis–mechanism and defects. *Diabetes-Damages and Treatments*, 2, 2011.

[122] Serenella Salinari, Alessandro Bertuzzi, and Geltrude Mingrone. Intestinal transit of a glucose bolus and incretin kinetics: a mathematical model with application to the oral glucose tolerance test. *American Journal of Physiology-Endocrinology and Metabolism*, 300(6):E955–E965, 2011.

[123] Pasquale Palumbo, Susanne Ditlevsen, Alessandro Bertuzzi, and Andrea De Gaetano. Mathematical modeling of the glucose–insulin system: A review. *Mathematical biosciences*, 244(2):69–81, 2013.

[124] Athena Makroglou, Jiaxu Li, and Yang Kuang. Mathematical models and software tools for the glucose-insulin regulatory system and diabetes: an overview. *Applied numerical mathematics*, 56(3-4):559–573, 2006.

[125] Jiraphat Yokrattanasak, Andrea De Gaetano, Simona Panunzi, Pairote Satiracoo, Wayne M Lawton, and Yongwimon Lenbury. A simple, realistic stochastic model of gastric emptying. *PloS one*, 11(4):e0153297, 2016.

[126] Mk Nauck, F Stöckmann, R Ebert, and W Creutzfeldt. Reduced incretin effect in type 2 (non-insulin-dependent) diabetes. *Diabetologia*, 29(1):46–52, 1986.

[127] Filip K Knop, Tina Vilsbøll, Patricia V Højberg, Steen Larsen, Sten Madsbad, Aage Vølund, Jens J Holst, and Thure Krarup. Reduced incretin effect in type 2 diabetes: cause or consequence of the diabetic state? *Diabetes*, 56(8):1951–1959, 2007.

[128] S Saber, E Bashier, S Alzahrani, and I Noaman. A mathematical model of glucose-insulin interaction with time delay. *J Appl Computat Math*, 7(416):2, 2018.

[129] Dang Vu Giang, Yongwimon Lenbury, Andrea De Gaetano, and Pasquale Palumbo. Delay model of glucose–insulin systems: global stability and oscillated solutions conditional on delays. *Journal of mathematical analysis and applications*, 343(2):996–1006, 2008.

[130] Andrea De Gaetano, Simona Panunzi, Alice Matone, Adeline Samson, Jana Vrbikova, Bela Bendlova, and Giovanni Pacini. Routine ogtt: a robust model including incretin effect for precise identification of insulin sensitivity and secretion in a single individual. *PLoS One*, 8(8):e70875, 2013.

[131] Nicolás Kuschinski, J Andrés Christen, Adriana Monroy, and Silvestre Alavez. Modeling oral glucose tolerance test (ogtt) data and its bayesian inverse problem. *arXiv preprint arXiv:1601.04753*, 2016.

[132] Alun L Lloyd. Realistic distributions of infectious periods in epidemic models: changing patterns of persistence and dynamics. *Theoretical population biology*, 60(1):59–71, 2001.

[133] David Champredon, Jonathan Dushoff, and David JD Earn. Equivalence of the erlang-distributed seir epidemic model and the renewal equation. *SIAM Journal on Applied Mathematics*, 78(6):3258–3278, 2018.

[134] Nicolás E Kuschinski, J Andrés Christen, Adriana Monroy, and Silvestre Alavez. Bayesian experimental design for oral glucose tolerance tests (ogtt). *arXiv preprint arXiv:1903.11697*, 2019.

[135] Paola Vargas, Miguel Angel Moreles, Joaquin Peña, Adriana Monroy, and Silvestre Alavez. Estimation and svm classification of glucose-insulin model parameters from ogtt data: a comparison with the ada criteria. *International Journal of Diabetes in Developing Countries*, pages 1–9, 2020.

[136] Marcos A Capistrán, Antonio Capella, and J Andrés Christen. Forecasting hospital demand during covid-19 pandemic outbreaks. *arXiv preprint arXiv:2006.01873*, 2020.

[137] Tyler Cassidy. Distributed delay differential equation representations of cyclic differential equations. *arXiv preprint arXiv:2007.03173*, 2020.

[138] Chiara Dalla Man, Michael Camilleri, and Claudio Cobelli. A system model of oral glucose absorption: validation on gold standard data. *IEEE Transactions on Biomedical Engineering*, 53(12):2472–2478, 2006.

[139] Hugo Alberto Flores Arguedas. Bayesian analysis of a model for glucose-insulin dynamics during the oral glucose tolerance test (ogtt). 2016.

[140] Christian W Eurich, Michael C Mackey, and Helmut Schwegler. Recurrent inhibitory dynamics: The role of state-dependent distributions of conduction delay times. *Journal of theoretical biology*, 216(1):31–50, 2002.

[141] Michael C Mackey and U An der Heiden. The dynamics of recurrent inhibition. *Journal of Mathematical Biology*, 19(2):211–225, 1984.

[142] Andrea De Gaetano, Thomas Hardy, Benoit Beck, Eyas Abu-Raddad, Pasquale Palumbo, Juliana Bue-Valleskey, and Niels Pørksen. Mathematical models of diabetes progression. *American Journal of Physiology-Endocrinology and Metabolism*, 295(6):E1462–E1479, 2008.

[143] Fernando Saldaña, Hugo Flores-Arguedas, José Ariel Camacho-Gutiérrez, and Ignacio Barradas. Modeling the transmission dynamics and the impact of the control interventions for the covid-19 epidemic outbreak. 2020.

[144] Sk Shahid Nadim, Indrajit Ghosh, and Joydev Chattopadhyay. Short-term predictions and prevention strategies for covid-2019: A model based study. *arXiv preprint arXiv:2003.08150*, 2020.

[145] Alexandra Teslya, Thi Mui Pham, Noortje E Godijk, Mirjam E Kretzschmar, Martin CJ Bootsma, and Ganna Rozhnova. Impact of self-imposed prevention measures and short-term government intervention on mitigating and delaying a covid-19 epidemic. *medRxiv*, 2020.

[146] Pauline Van den Driessche and James Watmough. Reproduction numbers and sub-threshold endemic equilibria for compartmental models of disease transmission. *Mathematical biosciences*, 180(1-2):29–48, 2002.

[147] Chayu Yang and Jin Wang. A mathematical model for the novel coronavirus epidemic in wuhan, china. *Mathematical Biosciences and Engineering*, 17(3):2708, 2020.

[148] World Health Organization et al. Assessment of risk factors for coronavirus disease 2019 (covid-19) in health workers: protocol for a case-control study, 26 may 2020. Technical report, World Health Organization, 2020.

[149] Günter Kampf, Daniel Todt, Stephanie Pfaender, and Eike Steinmann. Persistence of coronaviruses on inanimate surfaces and their inactivation with biocidal agents. *Journal of Hospital Infection*, 104(3):246–251, 2020.

[150] Biao Tang, Xia Wang, Qian Li, Nicola Luigi Bragazzi, Sanyi Tang, Yanni Xiao, and Jianhong Wu. Estimation of the transmission risk of the 2019-ncov and its implication for public health interventions. *Journal of Clinical Medicine*, 9(2):462, 2020.

[151] Jantien A Backer, Don Klinkenberg, and Jacco Wallinga. Incubation period of 2019 novel coronavirus (2019-ncov) infections among travellers from wuhan, china, 20–28 january 2020. *Eurosurveillance*, 25(5), 2020.

[152] Jon Herman and Will Usher. Salib: an open-source python library for sensitivity analysis. *Journal of Open Source Software*, 2(9):97, 2017.

[153] Tian-Mu Chen, Jia Rui, Qiu-Peng Wang, Ze-Yu Zhao, Jing-An Cui, and Ling Yin. A mathematical model for simulating the phase-based transmissibility of a novel coronavirus. *Infectious diseases of poverty*, 9(1):1–8, 2020.

[154] Secretaria of Health. Aviso epidemiologico: casos de infeccion respiratoria asociados a nuevo-coronavirus-2019-ncov. urlhttps://www.gob.mx/salud/es, 2020.

[155] José M Ponciano and Marcos A Capistrán. First principles modeling of nonlinear incidence rates in seasonal epidemics. *PLoS Comput Biol*, 7(2):e1001079, 2011.

[156] Jorge Nocedal and Stephen Wright. *Numerical optimization*. Springer Science & Business Media, 2006.

[157] Stanley C Eisenstat and Homer F Walker. Globally convergent inexact newton methods. *SIAM Journal on Optimization*, 4(2):393–422, 1994.

[158] Trond Steihaug. The conjugate gradient method and trust regions in large scale optimization. *SIAM Journal on Numerical Analysis*, 20(3):626–637, 1983.

[159] Youcef Saad and Martin H Schultz. Gmres: A generalized minimal residual algorithm for solving nonsymmetric linear systems. *SIAM Journal on scientific and statistical computing*, 7(3):856–869, 1986.

[160] Kathryn Turner and Homer F Walker. Efficient high accuracy solutions with gmres(m). *SIAM journal on scientific and statistical computing*, 13(3):815–825, 1992.

[161] EH Ayachour. A fast implementation for gmres method. *Journal of Computational and Applied Mathematics*, 159(2):269–283, 2003.

[162] H Saberi Najafi and H Zareamoghaddam. A new computational gmres method. *Applied mathematics and computation*, 199(2):527–534, 2008.

[163] Ilya M Sobol. Global sensitivity indices for nonlinear mathematical models and their monte carlo estimates. *Mathematics and computers in simulation*, 55(1-3):271–280, 2001.

[164] Christopher Nemeth, Chris Sherlock, and Paul Fearnhead. Particle metropolis-adjusted langevin algorithms. *Biometrika*, 103(3):701–717, 2016.

[165] Albert Parker and Colin Fox. Sampling gaussian distributions in krylov spaces with conjugate gradients. *SIAM Journal on Scientific Computing*, 34(3):B312–B334, 2012.

[166] Fred Brauer. Mathematical epidemiology: Past, present, and future. *Infectious Disease Modelling*, 2(2):113–127, 2017.

[167] Odo Diekmann, Johan Andre Peter Heesterbeek, and Johan AJ Metz. On the definition and the computation of the basic reproduction ratio r 0 in models for infectious diseases in heterogeneous populations. *Journal of mathematical biology*, 28(4):365–382, 1990.

[168] Herbert W Hethcote. The mathematics of infectious diseases. *SIAM review*, 42(4):599–653, 2000.

[169] Jiwei Jia, Jian Ding, Siyu Liu, Guidong Liao, Jingzhi Li, Ben Duan, Guoqing Wang, and Ran Zhang. Modeling the control of covid-19: Impact of policy interventions and meteorological factors. *arXiv preprint arXiv:2003.02985*, 2020.